Very High Energy Gamma-Rays emitting BL LAC's Population Study

Master Thesis
University of Turku
Department of Physics and Astronomy
Astronomy
2014
Vandad Fallah Ramazani
Supervised by:
Dr. Elina Lindfors

University of Turku
Department of Physics and Astronomy

Vandad Fallah Ramazani: Very High Energy Gamma-Rays emitting BL LAC's Population Study

Master's thesis, 91 pages, 2 Appendices
Astronomy
August 2014

Abstract

Context: BL Lacs are the most numerous extragalactic objects which are detected in Very High Energy (VHE) γ-Rays band. They are a subclass of blazars. Large flux variability amplitude, sometimes happens in very short time scale, is a common characteristic of them. Significant optical polarization is another main characteristics of BL Lacs. BL Lacs' spectra have a continuous and featureless Spectral Energy Distribution (SED) which have two peaks.

Among 1442 BL Lacs in the *Roma-BZB catalogue*, only 51 are detected in VHE γ-rays band. BL Lacs are most numerous (more than 50% of 514 objects) objects among the sources that are detected above 10 GeV by *FERMI-LAT*. Therefore, many BL Lacs are expected to be discovered in VHE γ-rays band. However, due to the limitation on current and near future technology of Imaging Air Cherenkov Telescope, astronomers are forced to predict whether an object emits VHE γ-rays or not.

Some VHE γ-ray prediction methods are already introduced but still are not confirmed. Cross band correlations are the building blocks of introducing VHE γ-rays prediction method.

Aims: We will attempt to investigate cross band correlations between flux energy density, luminosity and spectral index of the sample. Also, we will check whether recently discovered MAGIC J2001+435 is a typical BL Lac.

Methods: We select a sample of 42 TeV BL Lacs and collect 20 of their properties within five energy bands from literature and *Tuorla blazar monitoring program database*. All of the data are synchronized to be comparable to each other. Finally, we choose 55 pair of datasets for cross band correlations finding and investigating whether there is any correlation between each pair. For MAGIC J2001+435 we analyze the publicly available *SWIFT-XRT* data, and use the still unpublished VHE γ-rays data from *MAGIC collaboration*. The results are compared to the other sources of the sample.

Results: Low state luminosity of multiple detected VHE γ-rays is strongly correlated luminosities in all other bands. However, the high state does not show such strong correlations. VHE γ-rays single detected sources have similar behaviour to the low state of multiple detected ones. Finally, MAGIC J2001+435 is a typical TeV BL Lac. However, for some of the properties this source is located at the edge of the whole sample (e.g. in terms of X-rays flux).

keywords: BL Lac(s), Population study, Correlations finding, Multi wavelengths analysis, VHE γ-rays, γ-rays, X-rays, Optical, Radio

Contents

List of Figures

List of Tables

1 Introduction

Active Galactic Nuclei (AGNs) are compact regions in galaxies. They are exceptionally luminous at least in some parts of the electromagnetic spectrum. Accretion of matter by a super-massive black hole is believed to be the cause of AGN's radiation. They are the most luminous stable sources of radiation in the universe. Being distant objects, AGNs can be used as means for studying distant universe [1].

A subclass of AGNs, with the jet axes oriented close to the observer's line of sight, are called blazars. Typical observational features in blazars, such as strongly anisotropic radiation, super-luminal motion, high polarization and rapid variability are due to relativistic beaming. Blazars are divided into two subclasses, flat spectrum radio quasars (FSRQs) and BL Lacertae objects (BL Lacs). FSRQs are observationally characterized by broad spectral lines in the optical band, while such lines are weak or absent in BL Lacs [2].

BL Lacs are compact flat-spectrum radio sources with a violent flaring activity. They have featureless optical spectra and occasionally show a high linear polarization. The majority of the extragalactic objects yet detected at Very High Energy (VHE) photon energies mostly belong to the class of BL Lacs.

VHE γ-rays from celestial objects have been detected by pointing air Cherenkov telescopes. This forces astronomers to ensure about the existence of VHE γ-rays radiation before observation attempt. Existence of VHE γ-rays radiation could be proved by knowing spectral behaviour of object and extrapolating lower wavelengths detection to that part of spectrum. Therefore, a multi wavelength study plays a significant role in VHE γ-ray astronomy. On the other hand, objects within the same category show similar behaviour in different wavelengths. Finding out behaviour of specific type of objects is the main reason of their population study. Combination of multi wavelength and population study of an object type could result to introduction of a new object for VHE γ-ray detection.

BL Lac objects are the most numerous VHE γ-ray emitting extragalactic objects. A complete multi wavelength population study (including VHE γ-ray band) of BL Lac objects could be used to understand BL Lacs contribution to diffuse extragalactic γ-ray emission as well as in Extragalactic Background Light (EBL) studies.

VHE γ-Ray emitting BL Lac population study will lead to investigate cross band correlation for these objects. The latest work in this regard had been done by Wagner [3] on 17 VHE γ-ray emitting BL Lacs in 2008. Number of such sources was 44 in June 2012. Investigating the amount of available data play an important role in cross band correlation findings.

This thesis is assigned to cover this investigation and carrying out correlation finding as much as possible with the current available data. We will also check whether recently discovered MAGIC J2001+435 is a typical VHE γ-ray emitting BL Lac, as it's multi wavelengths properties had been little studied prior to its VHE γ-ray detection.

Different wavelengths properties of 41 BL Lac are collected from literature, to achieve the main aim of the thesis. For MAGIC J2001+435, X-rays data are reduced and analysed to calculate the properties of this band. The properties for this object in other wavelengths are collected from the literature.

In this chapter, VHE γ-ray sky and BL Lac objects will be introduced briefly. Chapter 2 covers Background of MAGIC J2001+435 (in this thesis "the source") and BL Lacs population study alongside with sample selection and implementation method. In chapter 3 objects and the source properties in different wavelengths are categorized, introduced and presented in details. Chapter 4 contains results and discussions on MAGIC J2001+435 and VHE γ-rays emitting BL Lacs population study. Finally, in chapter 5 we present future prospective of the work.

Hereafter, in this thesis the following terms are used as specified here. The term

"BL Lacs" related to all selected BL Lacs including the source. "BL Lacerate" is defined for the individual object in the sky that is known under the same name. The term "TeV source(s)/ object(s)/ BL Lac(s)" is used to indicate that source(s), object(s) or BL Lac(s) is already detected in VHE γ-rays band (i.e >150 GeV).

1.1 Very High Energy Gamma-ray sky

Radiations with energy above 100 GeV are called VHE γ-ray radiation. Earth's atmosphere is not transparent to radiation with energy above $\simeq 4$ [eV] (Ultraviolet wavelengths). Therefore, VHE γ-ray radiation is not directly observable on the Earth. With current technology, due to detection area limitation of space telescopes the upper limit of cosmic γ-ray energy is 100 GeV.

Due to low flux of the VHE γ-ray photons; to detect VHE γ-ray directly an ideal telescope with enormous (about football field size) collection area should be located in space. The indirect method is used to detect VHE γ-ray radiations from cosmic object. This method is based on the Imaging Air Cherenkov (IAC) technique. When high-energy γ-rays reach the earth's atmosphere, they start interacting with nucleons in the air. Secondary particles are the product of this interactions. Secondary particle also start to interact with atmosphere. Shower particle number reaches a maximum at about 10 [km] height and start to dim afterwards. The shower particles move faster than the local speed of light. Therefore, they emit a faint blue flash of light, Cherenkov light.

The Cherenkov light is emitted in a conical shape with the axes nearly parallel to the direction of the incident primary particle. The cone illuminates a circle, with the diameter about 250 [m], on the ground. This circle is often called the Cherenkov light pool. A very high energy (10^{12} [eV]) primary photon causes only about 100 [Ph/m^2] to be observable on the ground. These photons are observable in a short time period, maximum 20 [ns].

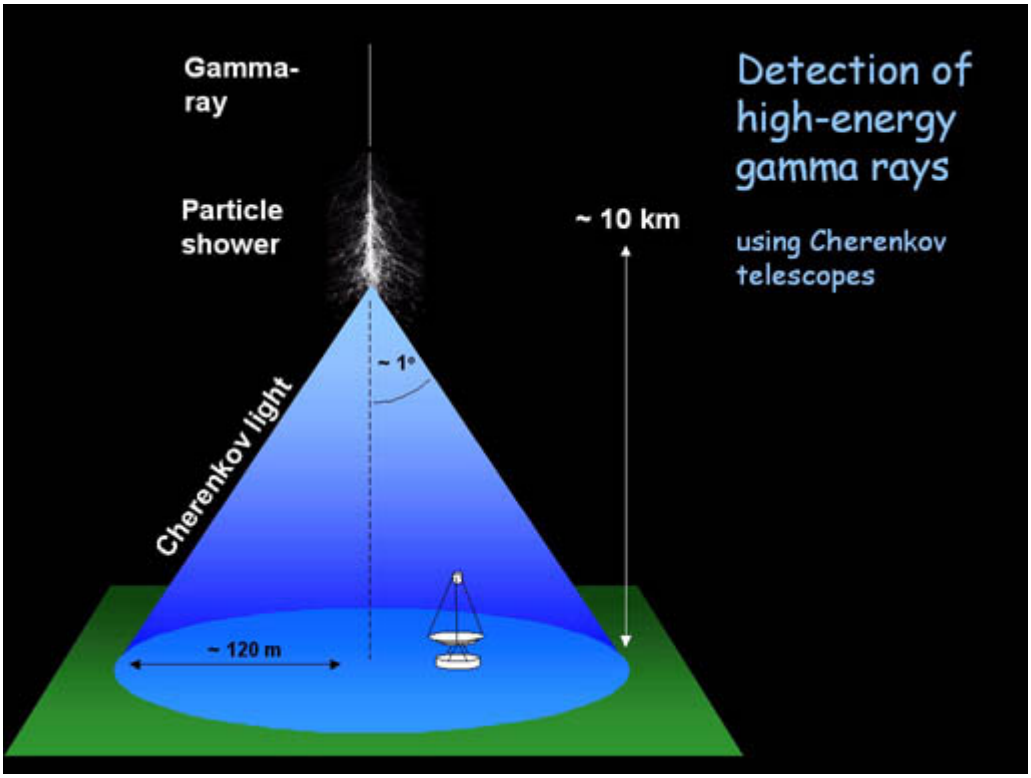

Figure 1. Cherenkov light pool [Wagner, 2006]

A telescope, located in the light pool (Figure 1), will "see" the air shower. To detect the light telescope's mirror area should be large enough to collect enough photons. The area of the Cherenkov light pool, ~ 50000 [m^2], roughly gives the "effective detection area" of a Cherenkov telescope.

The footprint of the air shower is illustrated in the image acquired by the telescope. The image intensity is related to the γ-ray energy. The image shape is used to reject unwanted "background".

It is difficult to reconstruct the geometry of the air shower with a single telescope. For more accurate geometry reconstruction, multiple telescopes are used which view the shower from different points. This allow a stereoscopic reconstruction of the shower geometry.[1]

MAGIC, HESS and VERITAS are the current generation of pointing telescopes

[1] `http://www.mpi-hd.mpg.de/hfm/HESS/pages/about/telescopes/#cherenkov`

which use IAC technique to observe VHE γ-ray of the different sources.

Cherenkov Telescope Array (CTA) which is planned to start operation in 2020 is the next generation of this kind of telescopes.

The first cosmic object detected in VHE γ-ray was the Crab nebula. This detection took place in 1989 by Whipple observatory. Before the current generation of IAC telescopes begin their operation only 14 celestial objects were observed in this waveband. According to TeV Catalogue[2], 145 celestial objects have been detected in VHE γ-ray band by June 2013.

Within the Galaxy following source types are detected in VHE γ-ray:

- **Pulsar Wind Nebula:** is an interstellar cloud powered by the wind of a highly magnetized, rotating Neutron star, Pulsar. Relativistic particle outflow from the central source is the main driver of these objects' emission. The VHE γ-rays is generated by scattering of the high energy electrons on photon target fields and producing Inverse Compton (IC)[4].

- **Supernova Remnant (SNR):** is the structure resulting from the explosion of a star in a supernova. [3] It is believed that they are the dominant sites of hadronic Galactic cosmic-ray (CR) acceleration to energies approaching $\sim 10^{15}$ [eV] [5]. CRs (hadrons and electrons) are injected into the SNR shock front, and are then accelerated via the diffusive shock acceleration (DSA) process. Subsequent γ-ray production from the interaction of these CRs with ambient matter and/or electromagnetic fields is a tracer of such non-thermal particle acceleration, and establishing the hadronic or leptonic nature of the parent CRs in any γ-ray source remains a key issue[6].

- **Unidentified sources:** For 28 TeV sources, it is not clear which of the other wavelengths sources within the positional errors are related to them. This

[2] `http://tevcat.uchicago.edu`

[3] `http://en.wikipedia.org/wiki/Supernova_remnant#Types_of_supernova_remnant`

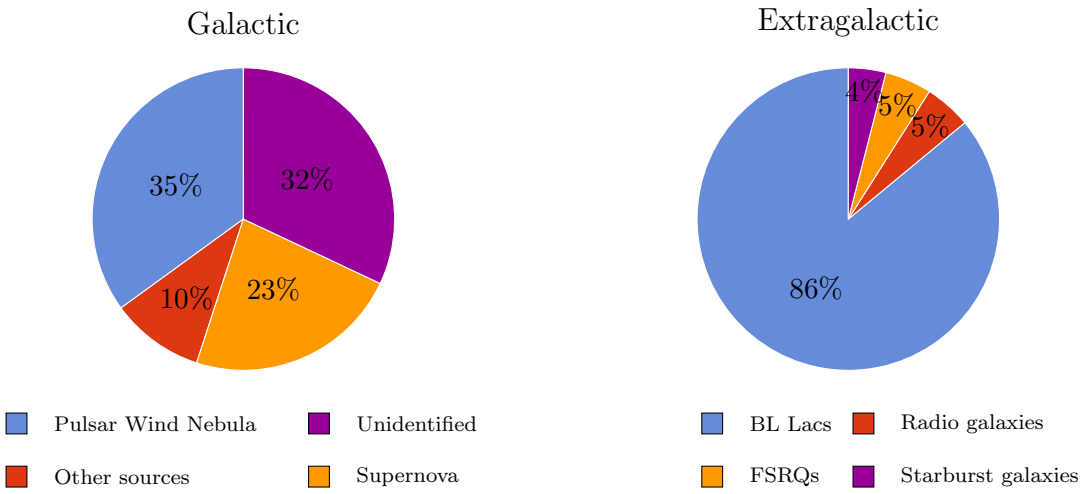

Figure 2. Galactic (left) and Extragalactic (right) TeV source types distribution

issue causes to categorize such sources as unidentified sources in VHE γ-ray sky. The latest work on Unidentified γ-ray sources is done by Massaro [7]. In their research, none of the unidentified TeV sources are specified. Almost all of this kind of sources are located near galactic plane. It is assumed that these sources are galactic sources.

Totally 88 TeV sources are within the Galaxy. Figure 2 shows different types of galactic TeV sources.

There were 57 Extragalactic TeV sources in VHE γ-ray sky (by June 2013). Almost all of these sources are from three different types of AGNs. Two starburst galaxies have also been detected VHE γ-rays band.

- **BL Lacs:** They are the most numerous extragalactic TeV sources type. 49 TeV objects in extragalactic sky are confirmed as BL Lacs up to July 2013. This object type will be defined extensively as the object type of interest in the next section.

- **FSRQs:** are subclass of blazars and observationally characterized by broad spectral lines in the optical band. There are three TeV FSRQs that have large

redshifts in the VHE γ-ray sky.

- **Radio galaxies Fanaroff-Riley Class I** (FR-I) In comparison to blazars jet axes direction of this type of AGN is not aligned to the observer's line of sight. These sources become fainter as one approaches the outer parts of the lobes. Jets are detected in most of FR-I galaxies (80%). Close to the core, the jet is one-sided. It becomes two-sided and continuous beyond a few kiloparsec. The component of the magnetic field in the plane of the sky, is at first parallel to the jet axis. It soon becomes aligned predominantly perpendicular to the axis. Centaurus A, M87 and NGC 1275 are TeV FR-I sources.[4]

- **Starburst galaxies** show the signatures of recent large-scale star formation activity. These are generally characterized by relatively strong radio emission. There is some speculation that there is evolution between the Starburst galaxies and AGNs. M82 and NGC 253 are two non-variable TeV startburst galaxies yet detected.[5]

Figure 2 right shows different types of extragalactic TeV sources. BL Lacs are the most numerous objects in extragalactic VHE γ-ray sky.

1.2 BL Lac objects

BL Lacs typically show lower radio power than FSRQs. They are characterized by rapid and large-amplitude flux variability and significant optical polarization. BL Lacs have spectra dominated by featureless non-thermal continuum. Their observed nuclear phenomenology is interpreted as being due to the effects of the relativistic jet. All known BL Lacs are associated with core dominated radio sources, many of them exhibiting super-luminal motion.

[4] `http://ned.ipac.caltech.edu/level5/Glossary/Essay_fanaroff.html`

[5] `http://ned.ipac.caltech.edu/level5/Glossary/Essay_starburst.html`

Jets from BL Lacs travel with the speed very near to the speed of light. BL Lacs' jet axis is nearly aligned to the observer's line of sight. Each point of jet emit light (radiation) through its path to the observer. This light does not reach to the observer much sooner than the original particles in the jet. In other words, the jet is chasing the light that it emits. This phenomena is called super-luminal motion or with exaggeration, travelling faster than the speed of light. The effect was discovered with Very Long Baseline Interferometry (VLBI) as it is the only way to resolve the AGNs jet.

Electromagnetic emissions from BL Lacs are observable from radio to VHE γ-ray frequency so their spectra have a continuous Spectral Energy Distribution (SED) which have two peaks. Synchrotron emission by highly relativistic electrons spiralling in the magnetic field of the jet is used to explain the lower frequency peak. Depending on assumed particles that cause γ-rays emission, leptonic and hadronic models are two approaches to model the second peak of SED. In leptonic model the higher frequency peak part of BL Lacs spectra is the result of Inverse Compton (IC) mechanism. Depending on the origin of seed photons for IC scattering there are two different scenarios. First scenario is External Compton (EC) by the same highly relativistic electron population and seed photons emitted by source external to the jet. In the second scenario seed photons for IC is provided by the synchrotron emission itself (Synchrotron Self Compton, SSC). In hadronic model proton synchrotron emission or photopion production are two main scenarios to model second hump of SED.

As BL Lacs have no or very weak Broad Line emission Region (BLR) there are more evidences that SSC scenario is the one that describe the higher frequency peak in BL Lacs SED. However, there is also more complicated scenarios, single-zone SSC does not reproduce all observed properties for BL Lacs. For FSRQs EC scenarios are favoured.

BL Lac objects also show rapid variability on time scales of days or shorter, during which they undergo strong flux variations often named "flares", with intrinsic time scales longer than the apparent ones.

The frequency at which lower frequency peak of BL Lacs' SED occurs is called synchrotron peak frequency (ν_{syn}). BL Lacs generally classified under three main categories according to their synchrotron peak frequency as below [8]:

- **Low energy peaked BL Lacs** (LBL), $\nu_{syn} < 10^{14}$ [Hz]
- **Intermediate energy peaked BL Lacs** (IBL), $10^{14} < \nu_{syn} < 10^{15}$ [Hz]
- **High energy peaked BL Lacs** (HBL), $\nu_{syn} > 10^{15}$ [Hz]

TeV BL Lacs are mostly HBLs. BL Lacs type will be discussed in details in section 3.1.2.

2 Backgrounds and Methodology

2.1 MAGIC J2001+435

MAGIC J2001+435 was first detected by the MAGIC stereoscopic telescope in VHE γ-ray band. It is positionally consistent with the Fermi-LAT γ-ray source 1FGL J2001.1+4351 (RA $20^h\ 01^m\ 13.5^s$, DEC $+43^\circ\ 53'\ 02.8''$, $J2000$), and the radio source MG4 J200112+4352 (RA $20^h\ 01^m\ 12.9^s$, DEC $+43^\circ\ 52'\ 52.8''$, $J2000$). The redshift of this source is still uncertain[9]. It was classified as a BL Lac object in 2009 [10] after its detection in γ-rays band. More specifically, this source is an IBL[8].

XMMSL1 J200112.7+435255 likely matches to be the same source. The positional uncertainty of XMM Slew source is only $4.51''$. The source ($0.2 - 12$ [keV]) flux is $\sim 5.5 \times 10^{-12}$ [erg/cm^2/s] with $\sim 60\%$ of the counts coming from the softest X-ray band ($0.2 - 2$ [keV]). In X-ray band the source is variable (by a factor of ~ 2) and has steep power law spectrum ($\Gamma = 2.7$)[10].

Due to its proximity to the galactic plane, the source has not been part of traditional BL Lacs samples. Therefore, its multi wavelengths properties are not well studied.

2.2 TeV BL Lacs population study

Costamante and Ghisellini 2002 [11] proposed in 2002 a general and simple criterion to select TeV BL Lacs candidates. 246 BL Lacs from Slew Survey Sample, EMSS[6], RASS[7], RGB[8], EXOSAT archive BL Lac catalogue and 1 Jy BL Lac sample had been selected and their radio (5 [GHz]), optical (5500 [Å]) and X-rays (1 [keV]) properties were compared to five then known TeV BL Lacs. They found that all TeV BL Lacs lie in two rectangles in Radio and X-rays flux energy density plane

[6]Einstein Medium Sensitivity Survey

[7]ROSAT All Sky Survey BL Lac sample

[8]ROSAT All Sky Survey - Green Bank sample

as well as Optical and X-rays flux energy density plane (please see Figures 4 and 5 in their paper). They predicted that 33 BL Lacs which are in the same region in these two plane as TeV BL Lac candidates. It is notable that two third of these candidates are now detected in VHE γ-rays band.

Wagner [3] studied 17 TeV BL Lacs to find any correlations between X-ray, optical, radio and VHE γ-ray luminosities. His research resulted in a visible trend between X-ray and VHE γ-ray luminosities which lead to the (correlation coefficient of 0.76)[9] and a linear fit to data with slope of 1.11. Data in optical and VHE γ-ray plane are more scattered than X-ray and VHE γ-ray plane. Radio luminosity, unlike optical and X-rays, does not show any clear trend to VHE γ-rays.

Abdo et. al. [12] conducted a detail investigation on spectral properties of LBAS[10]. In their sample 116 AGNs, including 42 BL Lacs[11], had been studied. There were seven TeV BL Lacs in the LBAS sample at the time of publication. They found a strong correlation between power law spectral index slope of AGNs between X-rays and γ-rays bands. They did not attempt to find this correlation within their sample's subclasses. Considering newly discovered TeV BL Lacs, the number of TeV BL Lacs in their sample is 16 now ($< 14\%$ of their sample).

Fan et. al. [13] collected quasi-simultaneous data for 39 BL Lacs from 2LAC[12] and MOJAVE[13] to investigate the radio-γ-rays connection. They reported positive correlation between radio flux (15 [GHz]) and γ-rays photon flux (1-100 [GeV]). Correlation coefficient using Spearman test is equal to 0.04.

Correlations between different wavelengths properties of TeV BL Lacs are expected to be present. Most of the published works are incomplete. As the aim of this thesis we will broaden the knowledge in this regard by focusing on two cross

[9]There is no information about type of correlation test.

[10]Fermi LAT Bright AGN Sample

[11]Their BL Lacs sample is not completely same as my sample.

[12]The Second LAT AGN Catalog

[13]Monitor of Jets in AGN with VLBA Equipment

bands properties of TeV BL Lacs. They are BL Lacs' flux energy density, luminosity and spectral index in different wavelengths.

2.3 Sample selection

In the *Roma-BZB catalogue* [14] 950 objects are categorized as confirmed BL Lacs. Whereas 492 objects are BL Lacs candidates. Out of the total number of 1442 BL Lacs only small fraction is detected to emit VHE γ-rays. TeVCat of University of Chicago keeps track of sources detected in VHE γ-rays. According to this catalogue confirmed number TeV BL Lacs in June 2012 (Start time of the thesis) was 44. Two objects were excluded from the sample because uncertainty about their type in that time. These objects are HESS $J1943+213$ (RA 19^h 43^m 55^s, DEC +21° 18′ 08″, $J2000$) and IC 310 (RA 03^h 16^m 43^s, DEC +41° 19′ 29″, $J2000$). Finally, 42 BL Lacs are selected as the sample. Figure 3 shows the sky position of those 42 TeV BL Lacs in galactic coordinates. The sample (Table 1) is sorted according to RA. BL Lacs positions are retrieved from *NASA/IPAC Extragalactic Database (NED)*[14].

Table 1: Sample and their position in the sky (J2000)

Source Name	**RA** $[hh:mm:ss]$	**DEC** $[dd°:mm':ss'']$
BZB J0013-1854	00:13:56	-18:54:07
1ES 0033+595	00:35:53	+59:50:05
RGB J0152+017	01:52:40	+01:47:17
3C 66A	02:22:40	+43:02:08
1ES 0229+200	02:32:49	+20:17:18
RBS 0413	03:19:52	+18:45:34
1ES 0347-121	03:49:23	-11:59:27
1ES 0414+009	04:16:52	+01:05:24
PKS 0447-439	04:49:25	-43:50:10
1ES 0502+675	05:07:56	+67:37:24
VER J0521+211	05:21:55	+21:11:24
Continued on next page		

[14] `http://ned.ipac.caltech.edu`

Table 1: continued from previous page

Source Name	**RA** $[hh:mm:ss]$	**DEC** $[dd^{\circ}:mm':ss'']$
PKS 0548-322	05:50:41	-32:16:16
RGB 0648+152	06:48:48	+15:16:25
1ES 0647+250	06:50:46	+25:03:00
RGB J0710+591	07:10:30	+59:08:20
S5 0716+714	07:21:53	+71:20:36
1ES 0806+524	08:09:49	+52:18:58
BZB J1010-3119	10:10:16	-31:19:09
1ES 1011+496	10:15:04	+49:26:01
1ES 1101-232	11:03:38	-23:29:31
Markarian 421	11:04:27	+38:12:32
Markarian 180	11:36:26	+70:09:27
1ES 1215+303	12:17:52	+30:07:01
1ES 1218+304	12:21:22	+30:10:37
W Comae	12:21:32	+28:13:59
PKS 1424+240	14:27:00	+23:48:00
H 1426+428	14:28:33	+42:40:21
1ES 1440+122	14:42:48	+12:00:40
PKS 1440-389	14:43:57	-39:08:39
AP Lib	15:17:42	-24:22:19
PG 1553+113	15:55:43	+11:11:24
Markarian 501	16:53:52	+39:45:37
1ES 1727+502	17:28:19	+50:13:10
1ES 1741+196	17:43:58	+19:35:09
1ES 1959+650	20:00:00	+65:08:55
MAGIC J2001+435	20:01:14	+43:53:03
PKS 2005-489	20:09:25	-48:49:54
PKS 2155-304	21:58:52	-30:13:32
BL Lacertae	22:02:43	+42:16:40
B3 2247+381	22:50:06	+38:24:37
1ES 2344+514	23:47:05	+51:42:18
H 2356-309	23:59:08	-30:37:41

2.4 Implementation

The work consist of three steps: I) Collecting sample data for different properties of BL Lacs from literature. II) Analysing X-ray data to complete the collection. III) Performing cross band correlation study.

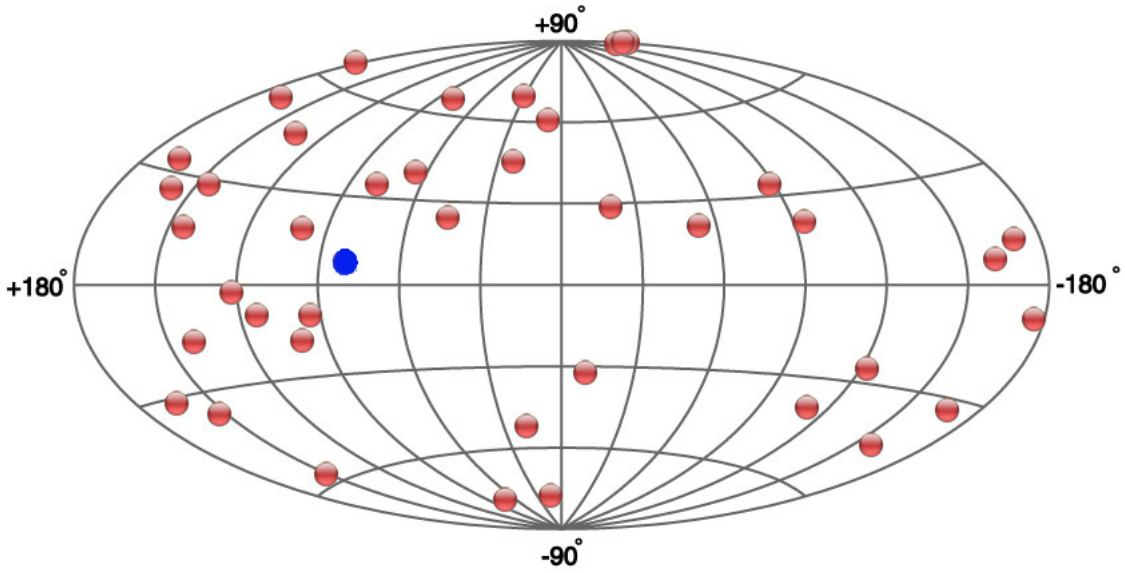

Figure 3. Sky position of the sample T. Blue circle indicates MAGIC J2001+435 [`http://tevcat.uchicago.edu`]

I) BL Lacs properties are categorize into five different categories.

- **General Properties** this category includes Redshift (z), Synchrotron Peak Frequency (ν_{syn}), Luminosity Distance (D_L) and Radio flux at 4.85 [GHz] (f_R). Redshift is used to calculate luminosity distance. Luminosity distance (D_L) is used to calculate the luminosity of BL Lacs in different selected wavelengths. Synchrotron Peak Frequency is used to categorize BL Lacs and the basis for further studies.

- **Optical Properties** Polarization properties and flux properties are two subclasses of this category. The former contains mean Degree of Polarization (DOP), Degree of Polarization variability (DOP_{var}), Polarization Angle (PA), Polarization Angle variability (PA_{var}) and finally the related optical band (POL_{band}) which polarization is observed in it. The later is combined of each object flux in optical R-band (f_O), flux variability ($f_{O,var}$) and host galaxy flux in R-band ($f_{O,Host}$).

- **X-ray Properties** X-ray integral energy flux (density) (S_X) between (2 – 10 [keV]), flux variability amplitude ($f_{X,var}$) and spectral index properties of BL Lacs will be studied. The latter contains spectral features that show the behaviour of spectra within the X-ray band. Spectra of BL Lacs follow two mathematical model (Spectral shape ($\Gamma_{X,t}$)). First model is Power Law (PL) and the second is Log Parabola (LP). The slope of spectra (Γ_X) is the main parameter to describe power law model. To define log parabola model a curvature parameter ($\Gamma_{X,c}$) is needed in addition to Γ_X.

- **Gamma-ray Properties** γ-ray integral flux between (1 – 100 [GeV]) range (f_γ) and flux variability index are ($f_{\gamma,var}$) are two important properties which included in this category. Spectral properties such as spectral shape ($\Gamma_{\gamma,t}$) and slope of spectra (Γ_γ) are two main parameters of spectral properties of this band.

- **VHE Gamma-ray Properties** divided into multiple and single detected categories. The former includes flaring and non-flaring states as subclasses. Integral flux (f_V) and spectral index (Γ_V) are the main parameters. We collect these parameters for both categories and their subclasses. For multiple detected category, integral flux variability amplitude ($f_{V,var}$) is an additional parameter that connects these two states together.

These 20 properties are collected from published papers and other sources of information. BL Lacs' flux energy density ($S = \nu f_\nu$ [erg/cm^2/s]) in each of the five selected band are calculated using the flux and frequency as the band indicator. Having flux energy density in hand, by using luminosity distance we calculate BL Lacs luminosity ($L \propto S * D_L^2$ [erg/s]) in different bands.

II) X-ray properties of Markarian 180 and BL Lacertae are reduced from their raw images obtained by *SWIFT* telescope. Comparing properties from this data

reduction and already published data from the literature ensures the validity of data reduction procedure. The source X-ray properties are obtained from *SWIFT* telescope observations. Details will be discussed in section 4.2. The source VHE γ-ray properties will be discussed qualitatively using a paper from MAGIC collaboration (Under the process of preparation). The source properties will be compared to sample properties as the last step of this section.

III) Flux energy density, luminosity and spectral index in different wavelengths are parameters for cross bands correlations finding. 55 pairs of datasets introduced according to these parameters. Correlations between each pair of datasets quantified by calculating Pearson product-moment correlation coefficient (PCC) [15] for them. PCC values show existence of linear correlation. To check power law correlations between pairs of datasets, datasets are linearised using $Y' = Ln(Y)$ and $X' = Ln(X)$ as the transforming parameters.

Finally, according to the best PCC value a linear or power law model fitted to each pair of datasets using a Fortran 90 code. The code calculates the best-fitted model parameters using linear regression method.

3 Step I: TeV BL Lacs Properties

3.1 General Properties

3.1.1 Redshift

Most of BL Lacs' host galaxies are large elliptical galaxies. Radiation absorption in the stellar atmospheres and cold interstellar clouds as well as strong non-thermal radiation from BL Lacs themselves made their spectral emission and absorption lines weak or absent. Therefore, redshift measurement is the most challenging property measurement for this type of object. BL Lacs' host galaxy imaging is an alternative if point source spectroscopy failed. Another alternate method to determine the redshift is observation of $Ly\alpha$, $Ly\beta$ and $Ly\gamma$ forests toward the object. By using the later method upper and the lower redshift limits are determined.

An accurate literature review take place in thesis to find the most reliable value for BL Lacs' redshift. Final result of literature review shows the following conclusions:

- For 35 BL Lacs redshift is measured from observed spectral lines.
- Redshift value for 1ES 0033+595 is available, but more recent observations disfavour this value. Therefore the value of 0.3 is assumed for its redshift.
- For MAGIC J2001+435, host galaxy redshift is $z = 0.19 \pm 0.04$. This value measured by Kari Nilsson in June 13, 2013 using Nordic Optical Telescope telescope (results of this work is not published yet).
- Two tentative redshift for PKS 0447-439 and 1ES 0502+675. Different values are published as their redshift. The values with more reputations are assumed for their redshift.
- Redshift lower limit for PKS 1424+240 is based on $Ly\beta$ and $Ly\gamma$ absorption features in the spectra as the most distance BL Lacs up to now.

- Redshift lower limit for 3C 66A is based on $Ly\alpha$ absorption features in the spectra

- Redshift lower limit for PG 1553+113 is based on confirmed $Ly\alpha + O_{vi}$ absorption features.

Each source redshift could be found in table 2 column 5 and its corresponding reference is presented in column 6 of the same table.

Table 2: Type, ν_{syn} and Redshift of BL Lacs

Source Name (1)	**Type (2)**	**log ν_{syn} (3)**	**Ref. (4)**	**z (5)**	**Ref. (6)**
BZB J0013-1854	HBL[a]			0.095	[16]
1ES 0033+595	HBL	18.93	[17]	0.300[g]	[18]
RGB J0152+017	HBL	15.29[c]	[19]	0.080	[20]
3C 66A	HBL	15.10	[8]	0.3347[h]	[21]
1ES 0229+200	HBL	19.45	[17]	0.139	[22]
RBS 0413	HBL	16.99	[17]	0.190	[23]
1ES 0347-121	HBL	16.73[c]	[19]	0.188	[24]
1ES 0414+009	HBL	20.71	[17]	0.287	[23]
PKS 0447-439	HBL	15.60	[8]	0.205[d]	[23]
1ES 0502+675	HBL	16.60	[8]	0.416[d]	[23]
VER J0521+211	IBL[b]			0.108	[25]
PKS 0548-322	HBL	15.76[c]	[19]	0.071	[16]
RGB 0648+152	HBL[b]			0.179	[26]
1ES 0647+250	HBL	18.28	[17]	0.410	[27]
RGB J0710+591	HBL	21.05	[17]	0.125	[20]
S5 0716+714	IBL	14.60	[8]	0.310	[23]
1ES 0806+524	HBL	16.57	[17]	0.137	[23]
BZB J1010-3119	HBL[b]			0.143	[23]
1ES 1011+496	HBL	16.30	[8]	0.212	[23]
1ES 1101-232	HBL	16.29[c]	[19]	0.186	[23]
Markarian 421	HBL	16.60	[8]	0.031	[23]
Markarian 180	HBL	18.61	[17]	0.046	[23]
1ES 1215+303	HBL	15.50[c]	[8]	0.130	[23]
1ES 1218+304	HBL	19.14	[17]	0.184	[23]
W Comae	IBL	14.50	[8]	0.103	[23]
PKS 1424+240	IBL	14.90[c]	[8]	0.604[e]	[28]

Continued on next page

Table 2: continued from previous page

Source Name (1)	**Type** (2)	**log ν_{syn}** (3)	**Ref.** (4)	**z** (5)	**Ref.** (6)
H 1426+428	HBL	18.55	[17]	0.129	[20]
1ES 1440+122	HBL	16.45	[17]	0.163	[20]
PKS 1440-389	HBL	15.40[c]	[19]	0.065	[16]
AP Lib	LBL	13.80[c]	[8]	0.048	[23]
PG 1553+113	HBL	15.40[c]	[8]	0.395[f]	[29]
Markarian 501	HBL	17.10	[8]	0.034	[23]
1ES 1727+502	HBL	17.40	[17]	0.055	[30]
1ES 1741+196	HBL	17.91	[17]	0.083	[18]
1ES 1959+650	HBL	16.60	[8]	0.047	[23]
MAGIC J2001+435	IBL[b]			0.190[i]	
PKS 2005-489	HBL	15.30[c]	[8]	0.071	[23]
PKS 2155-304	HBL	16.00	[8]	0.116	[23]
BL Lacertae	LBL	13.60	[8]	0.069	[23]
B3 2247+381	HBL	15.61	[17]	0.119	[20]
1ES 2344+514	HBL	16.40	[17]	0.044	[23]
H 2356-309	HBL	16.57[c]	[19]	0.165	[23]

a- This source is in sedentary survey of extreme high energy peaked BL Lacs[31]

b- The type relied on Fermi LAT Second AGN Catalogue[23]

c- Value has been estimated from $\alpha_{ox} - \alpha_{ro}$[23]

d- Tentative value, disfavoured by later observations

e- Lower limit estimation based on Lyβ and Lyγ

f- Lower limit based on confirmed Ly$\alpha + O_{vi}$ absorber

g- Assumed redshift

h- Lower limit estimation based on Lyα

i- Host galaxy redshift from unpublished data by Kari Nilsson

The presented redshift values are used as comparison parameter and in luminosity distance calculation. There is uncertainty on 15% of sample redshift.

BL Lacs redshift are constrained in a range of 0.031 (Markarian 421) and 0.604 (PKS 1424+240). Distribution of BL Lacs' redshifts is shown in figure 4 (Left Panel). This distribution was predictable. It confirms that there is more opportunity of VHE γ-rays detection from nearer BL Lacs. Possibility of VHE γ-rays interaction with extragalactic background light (EBL) photons reduces for BL Lacs near to us. Therefore, the observer has more opportunity to detect VHE γ-rays.

3.1.2 BL Lacs Type and Synchrotron Peak Frequency

ν_{syn} for BL Lacs are collected from three different papers (see table 2 column 3 and 4). Nieppola et al. [17] used parabolic function "$y = Ax^2 + Bx + C$" to fit the synchrotron component of SED in $\log\nu - \log\nu F$ plane.

Simple third degree polynominal "$\nu F_\nu = a\nu^3 + b\nu^2 + c\nu + d$" is the function which is used by Abdo et al. [8] to fit synchrotron component of SED in most of BL Lacs.

Another method which is used by Abdo et al. [8] to estimate ν_{syn} is based on using two spectral slopes (α_{ro}, α_{ox}). First is the power law slope connects radio flux to optical flux and the second one is related to power law slope connects optical flux to X-ray flux in SED. Same procedure is used by L.S. Mao in [19] based on data collected from *"THE RGB SAMPLE OF INTERMEDIATE BL LACERTAE OBJECTS"* [32], *"THE EINSTEIN SLEW SURVEY SAMPLE OF BL LACERTAE OBJECTS"* [33] and his private communication with Dr. Dario Gasparrini. Superscript "c" marks in front of ν_{syn} value in table 2, column 3 indicate usage of this procedure.

The value of ν_{syn} for each object is compared to the boundaries already introduced in section 1.2. Result of this comparison is the object's type. BL Lacs' type are presented in column 2 of table 2.

For objects which their ν_{syn} were not available in the literature (i.e. BZB J0013-1854, VER J0521+211, RGB 0648+152, BZB J1010-3119 and MAGIC J2001+435) I used their type based on other catalogues (see notes "a" and "b" at the end of table 2).

There are 2 LBLs, 5 IBLs and 35 HBLs in my sample using the boundary conditions in [8]. By changing boundary conditions to the ones mention in [17] the number of TeV BL Lacs changes to 4 LBLs, 22 IBLs and 16 HBLs accordingly.

It is clear now most of TeV BL Lacs are HBLs. This can be understood e.g. with SSC model for IC part of BL Lacs SED. Photons emitted from synchrotron

emission have more energy and they need less energy from electrons to reach the very high energies.

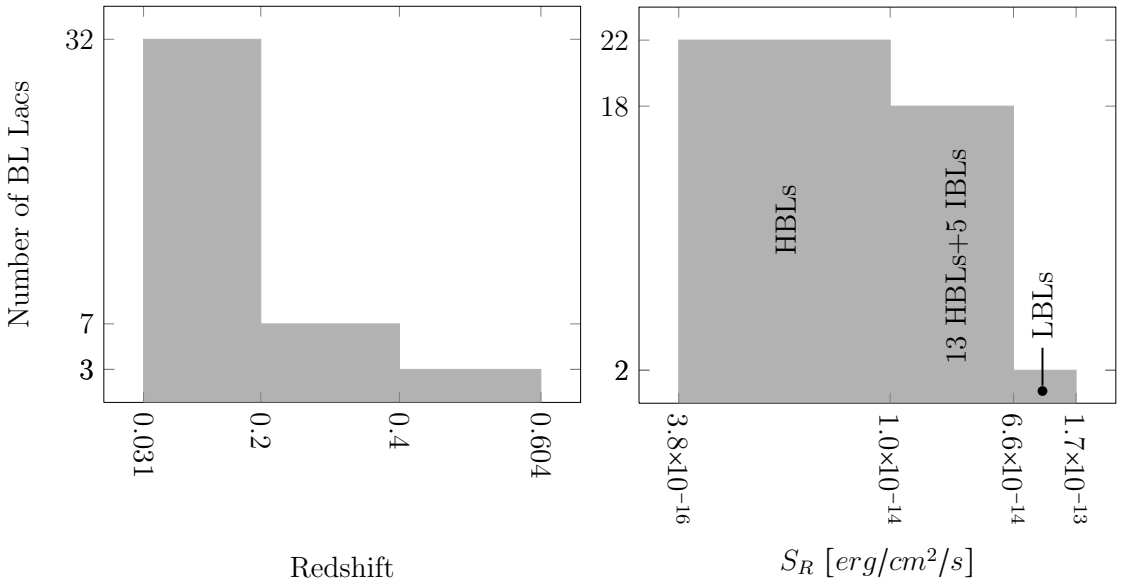

Figure 4. Distribution of BL Lacs's redshifts (Right panel) and radio flux energy density (Left Panel)

Different SED modelling procedures can affect this classification. As a sign of this effect, all log ν_{syn} values larger than 18 in table 2 are from Nieppola et al.[17].

In addition, BL Lacs are variable objects in most of the wavelengths. This will cause uncertainty of their classification during the flares.

3.1.3 Luminosity Distance

Objects flux depend on each object's distance. Object's luminosity is a distance independent parameter.

Luminosity distance (D_L) is the parameter which correlates object's flux (F) and luminosity (L) together.

$$L = 4\pi D_L^2 F \tag{1}$$

Luminosity distance of BL Lacs are calculated using NED Cosmology Calculator-

I (online tool [15]) [34] and following assumptions [35]:

- ΛCDM Model
- Flat universe
- Hubble constant $H_0 = 67.3$ [km/s/Mpc]
- Matter density $\Omega_M = 0.315$

Table 3 column 2 and 3 illustrate luminosity distance of BL Lacs in [Mpc] and [cm] units accordingly. Minimum and maximum values of sample are 141.3 [Mpc] and 3679.0 [Mpc].

3.1.4 Radio flux

Radio flux at 5 GHz is a good and accurate proxy of BL Lacs' relativistic jet power. Radiation in this low frequency is not affected by interstellar medium or dust through its way to the observer.

BL Lacs are well studied in radio band. Being a subclass of blazars correlation between radio and γ-ray emission is one of their typical properties. For further information and study on this matter please see Kovalev et al. [36]; Ghirlanda et al. [37], [38]; Mahony et al. [39] and Ackermann et al. [40].

In column 4 of table 3 BL Lacs' radio flux at 4.85 [GHz] (f_R) are presented. Column 5 of this table shows the reference which the data of the previous column comes from, while column 6 shows S_R in [erg/cm^2/s] unit.

In the sample S_R varies between 3.88×10^{-16} and 1.74×10^{-13} [erg/cm^2/s]. Sample distribution of S_R illustrated in figure 4 (Right Panel). HBLs generally emit less radiation in low frequency. Generally their jet power is less than other types of BL Lacs. It also could be described by considering the general SED shape of BL Lacs.

[15] `http://www.astro.ucla.edu/~wright/CosmoCalc.html`

The synchrotron peak of SED in LBLs are closer to radio frequency. Therefore, their radio fluxes are typically higher.

Table 3: Luminosity distance and radio flux of BL Lacss

Source Name (1)	D_L [**Mpc**] (2)	D_L [10^{27} cm] (3)	f_R [**mJy**] (4)	**Ref.** (5)	$S_R/10^{-15}$ [$erg/cm^2/s$] (6)
BZB J0013-1854	452.8	1.40	44	[41]	2.134
1ES 0033+595	1609.7	4.97	119	[42]	5.772
RGB J0152+017	377.5	1.16	53	[42]	2.571
3C 66A	1609.7	4.97	806	[42]	39.091
1ES 0229+200	681.6	2.10	46	[42]	2.231
RBS 0413	960.7	2.96	22	[23]	1.067
1ES 0347-121	949.5	2.93	8	[30]	0.388
1ES 0414+009	1529.9	4.72	70	[42]	3.395
PKS 0447-439	1045.5	3.23	231	[43]	11.204
1ES 0502+675	2356.1	7.27	25	[42]	1.213
VER J0521+211	519.2	1.60	530	[23]	25.705
PKS 0548-322	333.0	1.03	161	[30]	7.809
RGB 0648+152	899.3	2.77	67	[42]	3.250
1ES 0647+250	2316.0	7.15	79	[42]	3.832
RGB J0710+591	607.5	1.87	81	[42]	3.929
S5 0716+714	1671.7	5.16	788	[42]	38.218
1ES 0806+524	670.9	2.07	177	[42]	8.585
BZB J1010-3119	702.9	2.17	74	[23]	3.589
1ES 1011+496	1085.5	3.35	286	[42]	13.871
1ES 1101-232	938.3	2.90	66	[41]	3.201
Markarian 421	141.3	0.44	722	[42]	35.017
Markarian 180	212.0	0.65	274	[42]	13.289
1ES 1215+303	633.9	1.96	445	[42]	21.583
1ES 1218+304	927.1	2.86	56	[42]	2.716
W Comae	493.5	1.52	981	[42]	47.579
PKS 1424+240	3679.0	11.35	316	[42]	15.326
H 1426+428	628.6	1.94	38	[42]	1.843
1ES 1440+122	811.1	2.50	50	[42]	2.425
PKS 1440-389	303.6	0.94	92	[43]	4.462
AP Lib	221.5	0.68	2013	[41]	97.631
PG 1553+113	2216.6	6.84	638	[42]	30.943
Markarian 501	155.3	0.48	1371	[42]	66.494

Continued on next page

Table 3: continued from previous page

Source Name (1)	D_L [**Mpc**] (2)	D_L [10^{27} cm] (3)	f_R [**mJy**] (4)	**Ref.** (5)	$S_R/10^{-15}$ [$erg/cm^2/s$] (6)
1ES 1727+502	255.1	0.79	159	[42]	7.712
1ES 1741+196	392.4	1.21	339	[42]	16.442
1ES 1959+650	216.7	0.67	253	[42]	12.271
MAGIC J2001+435	1609.7	4.97	208	[42]	10.088
PKS 2005-489	333.0	1.03	1149	[43]	55.727
PKS 2155-304	560.6	1.73	407	[41]	19.740
BL Lacertae	323.2	1.00	3593	[42]	174.26
B3 2247+381	576.2	1.78	119	[42]	5.772
1ES 2344+514	202.5	0.62	231	[42]	11.204
H 2356-309	822.1	2.54	64	[23]	3.104

3.2 Optical Properties

Traditionally optical properties of astronomical objects are important in study of the objects' properties. Synchrotron emission from jet and thermal radiation from the host galaxy of BL Lacs are thought to be the domain of radiations which are observable in optical band. However, the emission site is rather uncertain. For some of the BL Lacs the host galaxy radiation is significant. While for some of them the host galaxies are not observable in optical band. To have more accurate comparison of the optical luminosity of the BL Lacs' jet, an estimation of the host galaxy flux is needed.

At least discovery of 5 new blazar in VHE γ-rays band by MAGIC were the result of optically triggered ToO observations [44]. VHE γ-rays discoveries which are resulted from optically triggered ToO observations need less time of observation VHE γ-rays (about half) in comparison to non triggered ones [45]. A connection between optical and VHE γ-rays states is expected, if the emission region of synchrotron and IC radiation is the same [44].

Optical polarization can be used as a tool for locating the emission region within the jet. Magnetic field of the jet can be traced by polarization properties. Domi-

nance of the synchrotron emission over the thermal components can be estimated by monitoring degree of the polarization. Effects of shocks on the magnetic field of the jet can be traced from optical polarization analysis.

3.2.1 Polarization Properties

Search for polarization data of TeV BL Lacs is done to find an appropriate collection of data for whole sample. Mean Degree of Polarization (DOP), its variability (DOP_{var}), Polarization Angle (PA) and its variability (PA_{var}) are the polarization parameters which I was looking for. At the end of my search the following resources give the best information collection for totally 26 objects of the sample.

- All five parameters available for 12 Objects in *"Polarimetric monitoring of Blazars at San Pedro Martir"* which takes place in time span between August and November 2009. The data are presented in Dominika Wylezalek's Bachelor Thesis [46].

- *"The optical polarization properties of X-ray-selected BL Lacertae objects"* contains result of 3 years monitoring started at 1987 for 37 BL Lacs. Maximum Degree of Polarization (DOP) for 4 objects (RBS 0413, 1ES 1101-232, 1ES 1218+304 and H 1426+428) of the sample were available in the published paper of this program [47]. The only available Polarization Angle (PA) and its variability (PA_{var}) in this paper were for RBS 0413.

- For three objects of the sample unpublished data from Liverpool Telescope [48] are used. These three objects are Markarian 421, Markarian 501 and PG 1553+113. Observations were takes place between September 2011 and July 2012. Minimum number of observations was 37 which gives good statistics to our calculation. I use calculation method like the one described in [46, section 5-4-2] to calculate polarization data.

- DOP and PA for PKS 1424+240 and AP Lib are retrieved from *"Optical and infrared polarimetry and photometry of blazars"* using the observations in the period of August 1986 to February 1988 [49].

- DOP and PA for 1ES 0502+675 and 1ES 1440+122 are retrieved from *"The Einstein Slew Survey Sample of BL Lacertae Objects"*. Former has a single observation and latter has three observations data available [33, Table 6].

- In *"Optical and infrared polarization of active extragalactic objects"* maximum and minimum values of DOP and PA collected from different papers[50]. I calculate mean value for DOP and PA using these data for PKS 0548-322, Markarian 180 and 1ES 1215+303. The variability of DOP and PA would be half the difference between maximum and minimum values.

Please see table 4 for complete detail of retrieved data which are available for the sample. The difference between the observed bands within different papers makes the sample inhomogeneous. The collected dataset is incomplete and is not uniform because of lack published data. We applied and have been granted a monitoring observation time from Nordic Optical Telescope (NOT)-cycle 49 for improving this part of study in future.

Study of the available data leads to the following summary:

- Mean degree of polarization (DOP) of the sample varies from 1.33% to 13.95%.

- Degree of polarization variability (DOP_{var}) varies from 1.72% to 12.34%.

- All objects that have multiple observations of PA, show some variability in PA.

Table 4: Optical polarization properties of BL Lacs

Source Name (1)	POL_{band} (2)	DOP [%] (3)	DOP_{var} [%] (4)	PA [°] (5)	PA_{var} [°] (6)	**Ref.** (7)
BZB J0013-1854						
1ES 0033+595	R	4.79	4.02	94.66	74.17	[46]
RGB J0152+017						
3C 66A	R	11.58	10.68	25.59	39.73	[46]
1ES 0229+200						
RBS 0413	All	5.21[a]		169	20	[47]
1ES 0347-121						
1ES 0414+009	R	3.97		150.93	17.18	[46]
PKS 0447-439						
1ES 0502+675	All	3.89		124.3		[33]
VER J0521+211						
PKS 0548-322[b]	All	1.75	0.25	80	55	[50]
RGB 0648+152						
1ES 0647+250	R	5.13	5.32	178.74	12.46	[46]
RGB J0710+591						
S5 0716+714	R	4.74	7.52	127.46	74.45	[46]
1ES 0806+524	R	2.01	1.97	121.83		[46]
BZB J1010-3119						
1ES 1011+496						
1ES 1101-232	All	1.33[a]				[47]
Markarian 421	All	3.1	6.89	89.95	173.16	[48]
Markarian 180[b]	All	2.5	1.5	132.5	12.5	[50]
1ES 1215+303[b]	v	10.2	4.8	150	30	[51],[50]
1ES 1218+304	R	6.83[a]				[47]
W Comae	All	13.95	1.72	55.61	7.51	[46]
PKS 1424+240	v	4.27		115.57		[49]
H 1426+428	All	2.48[a]				[47]
1ES 1440+122	All	2.2		86.3		[33]
PKS 1440-389						
AP Lib	v	4.83		18.72		[49]
PG 1553+113	All	4.03	6.64	102.39	91.75	[48]
Markarian 501	All	3.07	4.72	128.62	39.46	[48]
1ES 1727+502	R	3.04	6.96	104.68	28.9	[46]
1ES 1741+196						
1ES 1959+650	R	7.18	4.62	150.02	25.9	[46]

Continued on next page

Table 4: continued from previous page

Source Name (1)	POL_{band} (2)	DOP [%] (3)	DOP_{var} [%] (4)	PA [°] (5)	PA_{var} [°] (6)	**Ref.** (7)
MAGIC J2001+435						
PKS 2005-489						
PKS 2155-304	R	3.61	11.11	72.74	105	[46]
BL Lacertae	R	9.25	12.34	14.74	57.23	[46]
B3 2247+381						
1ES 2344+514	R	1.46	2.19	135.78	81.9	[46]
H 2356-309						

a- Maximum Degree of Polarization

b- Values are calculated from maximum and minimum values

3.2.2 R-Band Flux Properties

Within the optical waveband; R-band is selected to study the optical flux properties of TeV BL Lacs. These selection is due to available, well synchronized, long time monitoring of Tuorla blazar monitoring program. This program have been monitored 70% of the sample. BL lacs, which are not monitored by this program, are mainly located in the southern part of the sky. Monitoring duration is more than 3 years. In some cases the monitoring period exceeds to 10 years[16]. Data for the rest of the sample are collected from different published papers.

Flux variability of those 29 BL Lacs which are monitored Tuorla blazar monitoring program are presented in table 5. The rest of the sample are ignored to have uniform and comparable variability of R-Band optical flux. The following simple formula used for calculating flux variability.

$$f_{O,var} = \frac{|f_{average} - f_{max}|}{f_{average}} \tag{2}$$

Table 5 shows optical flux properties of the sample. Column 2 contains data of average radiation observed in optical for each source in [mJy] unit. Data in this column are corrected by considering host galaxy flux of sources. Column 3 shows

[16]Please visit `http://users.utu.fi/kani/1m/index.html` for further information

the related reference which data in column 2 are coming from. In column 4 the host galaxy flux of each BL Lac are illustrated. In column 5 you can find the variability of the flux of sample. Be noted that for some the BL Lacs flux variability was not available in the reference papers. Finally column 6 shows the sample optical flux energy density in [erg/cm^2/s] unit.

Distributions of BL Lacs' optical flux and optical flux variability are shown in figure 5.

Fainter BL Lacs in the sample has larger ν_{syn}. The first division of optical flux distribution just includes HBLs. ALL IBLs lie in the the second and third division of optical flux distribution. Finally LBLs are in the brightest division of distribution. This is consistence with the definition of synchrotron peak frequency divisions that are used.

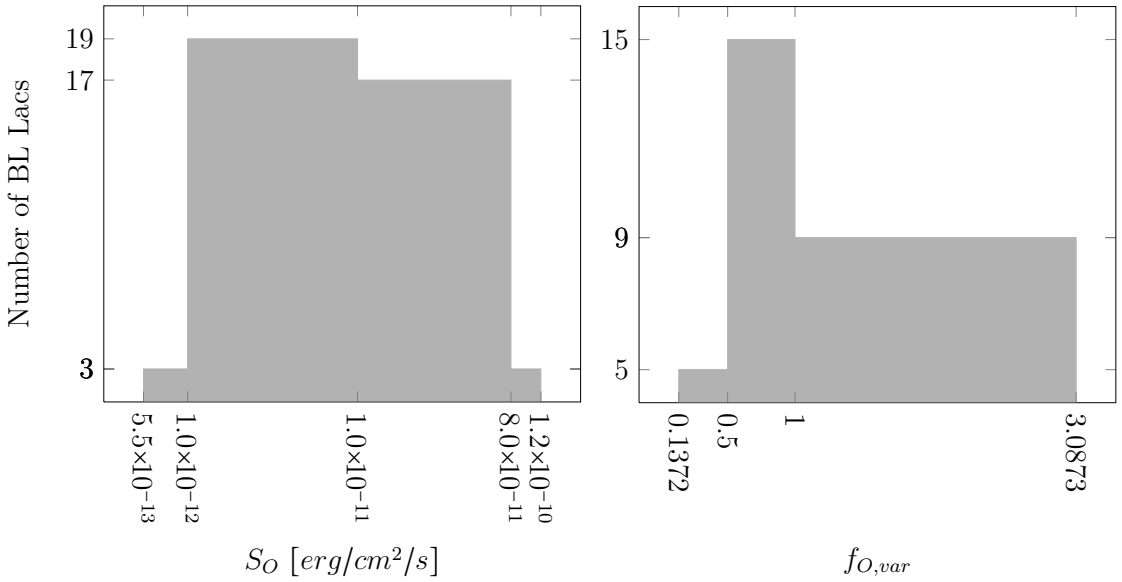

Figure 5. Distribution of BL Lacs' optical flux energy density and their optical flux variability

There is no correlation between different level of optical flux variability and types of BL Lacs. Optical flux variability is one the general characteristics of BL Lac objects. The result from our study is consistent with this definition. Optical flux variability of MAGIC J2001+435 lie in the most populated division of flux

variability distribution. Host galaxy flux for 26 BL Lacs are retrieved and presented in table 5. To complete the study, host galaxies flux values are needed for the rest of the sample.

Table 5: Optical flux properties of BL Lacs

Source Name (1)	f_O [**mJy**] (2)	**Ref.** (3)	$f_{O,Host}$ [**mJy**] (4)[a]	$f_{O,var}$ (5)	$S_O/10^{-11}$ $[erg/cm^2/s]$ (6)
BZB J0013-1854	10.199	[52]			4.95664
1ES 0033+595	0.2335	[53]	0.22[d]	0.7788	0.11346
RGB J0152+017	11.183	[52]			5.43484
3C 66A	7.3837	[53]	0.08	1.0303	3.58849
1ES 0229+200	0.1148	[53]	1	1.0979	0.05581
RBS 0413	0.1811	[53]	0.17	0.7796	0.08799
1ES 0347-121	0.7613	[24]		0.0305[b]	3.70000
1ES 0414+009	0.8841	[53]	0.19	0.7880	0.42966
PKS 0447-439	3.0800	[52]			1.49688
1ES 0502+675	0.7697	[53]	0.078	0.7259	0.37411
VER J0521+211	1.4126	[53]		0.2093	0.68653
PKS 0548-322	1.7724	[54]			0.86136
RGB 0648+152	0.6625	[53]		0.2060	0.32198
1ES 0647+250	1.3309	[53]	0.033	0.5616	0.64683
RGB J0710+591	2.4465	[55]			1.18901
S5 0716+714	19.772	[53]	0.1	1.6478	9.60902
1ES 0806+524	2.3442	[53]	0.69	1.0249	1.13929
BZB J1010-3119	2.1308	[52]			1.03559
1ES 1011+496	2.7898	[53]	0.49	0.5015	1.35584
1ES 1101-232	0.1226	[52]			0.05959
Markarian 421	18.148	[53]	8.1	1.241	8.82003
Markarian 180	1.4815	[53]	3.2	1.0227	0.71999
1ES 1215+303	3.1431	[53]	1[c]	0.6317	1.52753
1ES 1218+304	1.0974	[53]	0.4	0.8223	0.5333
W Comae	4.0020	[53]	0.58	0.7865	1.94495
PKS 1424+240	7.8142	[53]	0[e]	0.3666	3.79769
H 1426+428	0.4556	[53]	0.89	0.5007	0.2214
1ES 1440+122	0.6353	[56]			0.3087
PKS 1440-389	1.7724	[52]			0.8614
AP Lib	4.0700	[49]			1.97802

Continued on next page

Table 5: continued from previous page

Source Name (1)	f_O **[mJy]** (2)	**Ref.** (3)	$f_{O,Host}$ **[mJy]** (4)[a]	$f_{O,var}$ (5)	$S_O/10^{-11}$ $[erg/cm^2/s]$ (6)
PG 1553+113	12.137	[53]	0[e]	0.4698	5.89845
Markarian 501	4.3535	[53]	12	0.5898	2.11578
1ES 1727+502	0.9285	[53]	1.25	0.7269	0.45123
1ES 1741+196	0.9115	[53]	2.21	0.9165	0.44299
1ES 1959+650	3.6000	[53]	1.7[c]	1.6428	1.74962
MAGIC J2001+435	1.2900	[53]		0.951	0.62597
PKS 2005-489	0.3772	[52]			0.18331
PKS 2155-304	24.643	[53]	1.17	0.7261	11.9764
BL Lacertae	6.0116	[53]	1.38	3.0873	2.92163
B3 2247+381	0.5980	[53]	0.7	1.0082	0.29063
1ES 2344+514	4.3441	[53]	3.71[c]	0.1372	2.11125
H 2356-309	0.8483	[57]			0.41228

a- Presented data in this column are collected from Tuorla Blazar monitoring Program [53]

b- This source data are collected from [24]

c- The values are host galaxy together with nearby star flux

d- The value is nearby star flux

e- Host galaxy is not detected

3.3 X-Ray Properties

In BL Lacs' SED generally X-ray (0.15 – 150 [keV]) is located between the end of first hump and the beginning of the second one. This make X-ray properties one of the important wavelengths when attempting to study BL Lacs. The middle part of X-ray band (2 – 10 [keV]) is the best estimation of the whole band. Flux properties indicate amount of energy which is emitted from objects while spectral properties give us the shape of spectra in this band to predict behaviour outside of the selected range (2 – 10 [keV]). To have a good comparison within different object the average integral flux in the range of (2 – 10 [keV]) is the first important parameter. X-ray flux variability is the other important factor which gives the variance of X-ray flux from the average integral flux. Also searching for the variability of the objects could

lead to find a correlation between X-ray and the other wavelengths.

Flux, Flux variability and spectral properties of sample are presented in following sections.

3.3.1 Flux Properties

Count rate of point sources in soft X-ray ($0.3 - 2$ [keV]) are high. This cause saturation on detector pixels. Therefore flux uncertainty increase in this range. To avoid detection uncertainty ($2 - 10$ [keV]) range is selected for X-ray flux energy density (S_X) study. Having more observation in large epoch give more accuracy in calculating average integral flux and variability of objects. Data reduced from same instrument decreases statistical error of calculated average integral flux.

An alternative could be searching for X-ray flux properties of objects near the epoch which their VHE γ-rays properties come from.

BL Lacs X-ray integral flux are presented in column 2 of table 6. The related references for this column data are presented in column 3.

BL Lacs' X-ray flux variability amplitude ($f_{X,var}$) are illustrated in column 4 of table 6. The values indicate the count rate ratio of maximum and minimum integral flux between $0.3 - 10$ [keV] in [counts/s] unit. Data are retrieved from available online light curves [17] of "Swift X-ray Telescope Monitoring of Fermi-LAT Gamma Ray Sources of Interest" [58]. The images are downloaded from website and by measuring pixels in an image processor software the count rate are estimated for the highest and lowest points in image. Then count rate ratios between highest and lowest points are calculated for 32 out of 42 BL Lacs. As shown in figure 6 (left panel), most of the objects have $f_{X,var} < 10$, while Markarian 421 shows the most extreme variability amplitude.

To validate the above mentioned procedure observational bias should be checked.

[17] `http://www.swift.psu.edu/monitoring/`

Observing each object might end up only in low (or high) state by using small number of observations ($N_{X,O}$). In principal this issue will cause the variability amplitude to be smaller. I checked correlation between number of observations and variability amplitude on sample. In figure 6 (Right panel), circles show the result of my check in logarithmic scale. As illustrated in this figure with same number of observation different objects have different variability amplitude. It is apparent that variability amplitude is trending with number of observations.

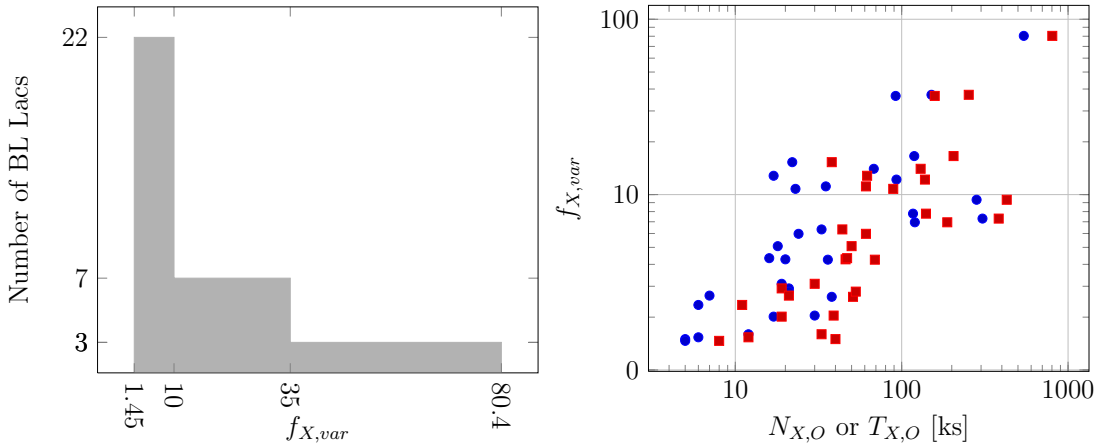

Figure 6. Left: X-ray flux variability amplitude distribution. Right: X-ray flux variability amplitude vs. number of observation (circles) and total exposure time [ks] (squares) [logarithmic scale]

The same procedure is used for finding correlation between variability amplitude and total exposure time of all observations ($T_{X,O}$). As illustrated in figure 6 (Right panel) by squares, similar conclusion comes out for correlation between $f_{X,var}$ and $T_{X,O}$. In table 6 column 5 and 6 values for $N_{X,O}$ and $T_{X,O}$ are presented.

Minimum and maximum number of observations for individual objects are 5 and 542 accordingly. On the other hand, minimum and maximum total exposure time of all observation for individual objects are 8 and 804 [ks] accordingly. Flux variability amplitude distribution illustrated in figure 6 (left panel).

Table 6: X-ray flux properties of BL Lacs

Source Name	$S_X/10^{-12}$ $[erg/cm^2/s]$	**Ref.**	$f_{X,var}$	$N_{X,O}$	$T_{X,O}$ $[ks]$
(1)	**(2)**	**(3)**	**(4)**	**(5)**	**(6)**
BZB J0013-1854					
1ES 0033+595	58.9	[59]	3.10	19	30
RGB J0152+017	2.70	[55]			
3C 66A	4.16	[8]	10.78	23	89
1ES 0229+200	14.9	[59]	2.61	38	51
RBS 0413	7	[31]			
1ES 0347-121	6	[31]			
1ES 0414+009	8.4	[31]	2.92	21	19
PKS 0447-439	7.6	[8]	5.08	18	50
1ES 0502+675	19.2	[59]	1.50	5	40
VER J0521+211	31.4	[60]	15.31	22	38
PKS 0548-322	41.1	[61]			
RGB 0648+152			2.35	6	11
1ES 0647+250			4.25	36	69
RGB J0710+591			2.04	30	39
S5 0716+714	9.7	[8]	16.58	119	205
1ES 0806+524	8.7	[62]	2.80	21	53
BZB J1010-3119					
1ES 1011+496	3.6	[61]	5.98	24	61
1ES 1101-232	36.8	[59]			
Markarian 421	531	[61]	80.40	542	804
Markarian 180[a]	50.7	[61]			
1ES 1215+303	1.6	[61]	4.27	20	46
1ES 1218+304	14.8	[31]	6.33	33	44
W Comae	0.5	[61]	36.55	92	158
PKS 1424+240	2	[61]	11.14	35	61
H 1426+428	10.3	[31]	6.95	120	188
1ES 1440+122			1.46	5	8
PKS 1440-389			2.65	7	21
AP Lib	5.6	[61]	1.60	12	33
PG 1553+113	4.7	[61]	14.03	68	130
Markarian 501	65.4	[61]	7.30	306	383
1ES 1727+502	8.9	[63]	1.53	6	12
1ES 1741+196	6.9	[59]	2.01	17	19
1ES 1959+650	71.7	[61]	7.79	117	140

Continued on next page

Table 6: continued from previous page

Source Name (1)	$S_X/10^{-12}$ $[erg/cm^2/s]$ **(2)**	**Ref.** **(3)**	$f_{X,var}$ **(4)**	$N_{X,O}$ **(5)**	$T_{X,O}$ $[ks]$ **(6)**
MAGIC J2001+435[a]			12.81	17	62
PKS 2005-489	48.5	[61]			
PKS 2155-304	76	[64]	37.09	151	253
BL Lacertae[a]	11.2	[61]	9.34	282	428
B3 2247+381	6.83	[65]	4.34	16	47
1ES 2344+514	2.1	[61]	12.18	93	138
H 2356-309	53	[64]			

a- These objects properties are also calculated as part of the thesis [section 4.2]

3.3.2 Spectral Index Properties

Spectral index properties in X-ray could predict the behaviour or the physics of BL Lacs emission in shorter wavelengths (i.e. γ-rays and VHE γ-rays). By assuming stochastic acceleration scenario there is a link between spectral curvature parameter to the volume of the emitting region. This comes out from inverse proportionality of the curvature to the number of acceleration steps. It indicates the emitting electron density to be larger if the curvature parameter is lower. Therefore, inverse Compton component of SED become brighter which leads to more detection opportunity of γ-rays and VHE γ-rays radiation from the source [66].

Generally X-rays part of BL Lacs spectrum could be described with Power Law (PL) and Log Parabola (LP) models. I synchronised data from different publications by the following forms.

The PL model is the form of:

$$F(E) = KE^{-\Gamma_X} \tag{3}$$

The LP model is the form of:

$$F(E) = KE^{-(\Gamma_X + \Gamma_{X,c}\log(E/E_p))} \tag{4}$$

Where K is normalization factor, E_p is the pivot energy, Γ_X is slope of spectra and $\Gamma_{X,c}$ is curvature of spectra in the pivot energy.

In column 2 of table 7 the best fitted model ($\Gamma_{X,t}$) for each BL Lac are presented from different publications. Column 3 shows slope of spectra and column 4 shows curvature of spectra when it is applicable (i.e. best fitted model is LP). The last column show the reference number in bibliography which data for column 2 through 4 are collected from.

Table 7: X-ray spectral properties of BL Lacs

Source Name (1)	$\Gamma_{X,t}$ (2)	Γ_X (3)	$\Gamma_{X,c}$ (4)	**Ref.** (5)
BZB J0013-1854	LP	1.86±0.04	0.59±0.09	[67]
1ES 0033+595	PL	2.06±0.03	NA	[59]
RGB J0152+017	PL	2.72±0.08	NA	[55]
3C 66A	PL	2.67±0.39	NA	[8]
1ES 0229+200	PL	1.99±0.05	NA	[59]
RBS 0413	LP	1.6±0.3	0.4±0.2	[31]
1ES 0347-121	LP	1.7±0.2	0.4±0.2	[31]
1ES 0414+009	LP	2.3±0.4	0.3±0.3	[31]
PKS 0447-439	LP	2.53±0.02	0.36±0.06	[8]
1ES 0502+675	PL	2.3±0.23	NA	[59]
VER J0521+211	PL	2.47±0.1	NA	[60]
PKS 0548-322	LP	1.55±0.16	0.27±0.1	[61]
RGB 0648+152	PL	2.51±0.06	NA	[68]
1ES 0647+250				
RGB J0710+591	PL	1.86±0.01	NA	[69]
S5 0716+714	PL	2.7±0.06	NA	[8]
1ES 0806+524	PL	2.4±0.1	NA	[62]
BZB J1010-3119	LP	1.88±0.06	0.76±0.14	[67]
1ES 1011+496	PL	2.52±0.08	NA	[61]
1ES 1101-232	LP	2.01±0.06	NA	[59]
Markarian 421	LP	1.97±0.01	0.4±0.02	[61]
Markarian 180[a]	LP	1.86±0.05	0.66±0.13	[61]
1ES 1215+303	PL	2.56±0.1	NA	[61]
1ES 1218+304	LP	2.1±0.03	0.37±0.03	[31]
W Comae	PL	2.35±0.24	NA	[61]

Continued on next page

Table 7: continued from previous page

Source Name (1)	$\Gamma_{X,t}$ (2)	Γ_X (3)	$\Gamma_{X,c}$ (4)	**Ref.** (5)
PKS 1424+240	PL	2.35±0.18	NA	[61]
H 1426+428	LP	1.81±0.03	0.11±0.03	[31]
1ES 1440+122	LP	1.85±0.05	0.48±0.11	[67]
PKS 1440-389	LP	2.50±0.04	0.40±0.10	[70]
AP Lib	PL	1.48±0.1	NA	[61]
PG 1553+113	LP	2.5±0.06	0.35±0.19	[61]
Markarian 501	LP	1.93±0.03	0.22±0.07	[61]
1ES 1727+502	LP	2.12±0.05	0.46±0.15	[67]
1ES 1741+196	PL	2.02±0.08	NA	[59]
1ES 1959+650	LP	2.05±0.04	0.59±0.07	[61]
MAGIC J2001+435[a]				
PKS 2005-489	LP	2.02±0.07	0.28±0.16	[61]
PKS 2155-304	LP	2.38±0.01	0.48±0.01	[71]
BL Lacertae[a]	PL	1.88±0.25	NA	[61]
B3 2247+381	PL	2.60±0.3	NA	[65]
1ES 2344+514	PL	2.56±0.32	NA	[61]
H 2356-309	LP	1.78±0.03	0.25±0.03	[31]

a- These objects properties are also calculated as part of the thesis [section 4.2]

Figure 7 shows the distribution of Γ_X for the sample. IBLs have softer spectra than other types. IBLs are within last three group in the distribution. Two LBLs lie in the lowest and the third group accordingly. LBLs have hard spectra. HBLs distributed over whole domain.

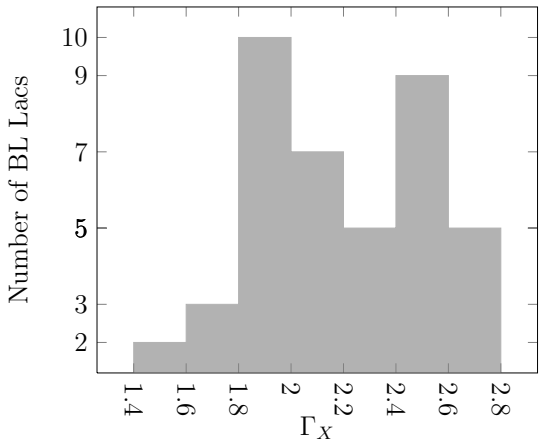

Figure 7. Distribution of BL Lacs' X-ray spectral index

Softening and hardening of X-rays spectra depends on the position synchrotron peak frequency in SED. For LBLs, X-ray band lays between two humps of SED. In that portion the shape of SED is somehow flat. Therefore, spectral index will be hard. In IBLs, X-ray band located at the end of first hump. Thus, the spectral index is generally soft in that area. Finally, position range of synchrotron peak frequency is wide for HBLs. Hence, spectral index can vary from soft to hard for this type of BL Lacs. Described connections between synchrotron peak frequency and X-rays spectral index are not general for all BL Lacs, but for our sample (which only include two LBLs and five IBLs) it could describe the shape of Γ_X distribution.

3.4 Gamma-Ray Properties

Gamma-Ray band, also known as high energy band, in astronomy generally predicated to electromagnetic radiation with frequency higher than 2.42×10^{20} [Hz] ($wavelength \leq 1.24 \times 10^{-12}$[m] or $energy \geq 1$[MeV]).

In 2008, *FERMI* (satellite) opened the window for observing whole sky in range of 10 [KeV] to 300 [GeV]. Low energy (10 [KeV] to 25 [MeV]) radiations are observing by Gamma-ray Burst Monitor (GBM) instrument while the high energy part (from 30 [MeV] to 300 [GeV]) is done by Large Area Telescope (LAT) instrument on board of *FERMI*.

Field of view is ~ 2.4 sr for *FERMI* LAT instrument. This instrument is most sensitive (in E^2dN/dE) for photon energy about 3 GeV. From this energy range up to ~ 300 [GeV] the on-axis effective area for instrument response functions (P7CLEAN V6) is at least 0.7 [m^2]. The 68% containment radius of the point-spread function (PSF) is narrowing to $\sim 0.2^\circ$ above 100 [GeV] [72].

All of the data presented in this section are from "Fermi Large Area Telescope Second Source Catalog". Totally 1873 sources detected and characterized in this catalogue. From total number of sources, 127 sources are firmly identified. On the

other hand, 1171 sources have reliable association with counterparts which are in the class of γ-rays emitting sources or are likely to emit γ-rays[73].

There are 1017 γ-ray sources associated statistically with AGNs in "The Second LAT AGN Catalog (2LAC)". Consequently the clean sample of sources that includes 886 AGNs. Among the total number of AGNs there are 395 BL Lacs [23].

According to *"The First Fermi-LAT Catalog of Sources Above 10 GeV"*, BL Lac objects are the most numerous. AGNs, including BL Lacs, have the total number of 388 out of 514 sources, which detected above 10 [GeV]. More than 50 % of the whole sample and 66 % of AGNs are BL Lacs [72].

Energy range between 1 and 100 [GeV] is selected from the available ranges, in the 2FGL catalogue, to study BL Lacs γ-rays flux properties. The best sensitivity of *FERMI* LAT lies in this range. On the other hand the properties above 150 [GeV] will be studied in VHE γ-rays part which IACT telescopes give the best results.

3.4.1 Spectral Properties

Power Law (PL) and Log Parabola (LP) are the models which describe BL Lacs spectra in γ-rays. By knowing the spectral properties one can extrapolate the VHE γ-rays flux. This extrapolated flux could be assumed as an upper limit of the flux in VHE γ-rays band. If this upper limit is high enough, it can be concluded that the VHE γ-rays radiation is in a range more than IACT sensitivity range. Therefore, shape of spectra in γ-rays is one of the best predictor for VHE γ-rays emission detection of BL Lacs.

In 2FGL catalogue [73] they first fit AGNs spectra with a LP model.

$$\frac{dN}{dE} = K\ (\frac{E}{E_0})^{-(\Gamma_\gamma + \beta \log(\frac{E}{E_0}))} \tag{5}$$

where Γ_γ, β and E_0 are accordingly spectral slope at E_0, curvature and arbitrary reference energy that evolves for each source along the iterations. Significance of

the curvature is checked by:

$$TS_{curve} = 2[\log L(LogParabola) - \log L(Power\ law)] \quad (6)$$

where L represents the likelihood function. Power-law is a special case of log parabola model which its β is equal to zero. Therefore, TS_{curve} distributed as χ^2 by one degree of freedom. The value of $TS_{curve} > 16$ corresponds to 4σ significance of curvature. All the sources in the catalogue were checked and if the TS_{curve} value goes down the limit value the result of power-law model fitting is presented. The pivot energy was computed as the energy at which the relative uncertainty on the differential flux K was minimal.

Column 5 in table 8 shows models which the BL Lacs spectra are best fitted with. Meanwhile, column 6 in table 8 shows best fit photon index which describe the spectra in power-law. Sources which have log parabola spectral shape indicates the value of spectra slope at pivot energy.

In our sample four BL Lacs have spectra which shows enough curvature significance to be modelled by log parabola. They are 3C 66A, S5 0716+714, 1ES 1011+496 and BL Lacertae. Their spectral curvature (β) are 0.0408, 0.0375, 0.0749 and 0.0950 accordingly. Their spectral index (Γ_γ) are above 1.71. There are two HBLs, one IBL and one LBL with curved spectral shape. Therefore, there is no connection between curvature of spectral shape and type of BL Lacs in this band.

Distribution of spectral index for the sample in γ-rays band is shown in figure 8 (Right panel). By choosing proper boundaries for spectral index, LBLs and IBLs will be grouped in one of our sample division. HBLs have harder spectra in comparison to LBLs and IBLs.

HBLs spectra first hump is lie nearer to the γ-rays band and their synchrotron emission has more energy to be transferred to the IC part of their SED. Therefore, it was expected that HBLs spectra is harder than the one of IBLs and LBLs. Which means total integral flux detected in γ-rays band is higher for HBLs.

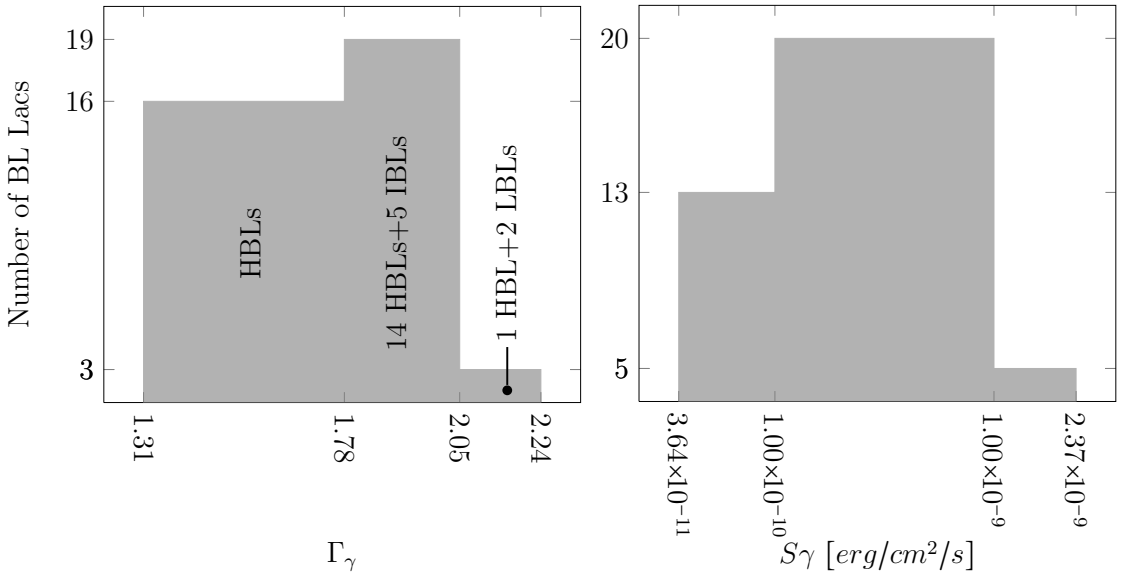

Figure 8. Distribution of BL Lacs's spectral index (Left Panel) and flux energy density (Right panel) in γ-rays band.

3.4.2 Flux Properties

In 1FGL [74] and 2FGL [73] catalogues, the photon fluxes originally reported in five energy bands (100 to 300 [MeV]; 300 [MeV] to 1 [GeV]; 1 to 3 [GeV]; 3 to 10 [GeV]; 10 to 100 [GeV]) by freezing the spectral index to that obtained in the fit over the full range and adjusting the normalization in each spectral band.

Two methods could be used to calculate integral flux in the range of 1 to 100 [GeV]. The first method is summing integral flux over three individual ranges (i.e. 1 to 3 [GeV], 3 to 10 [GeV] and 10 to 100 [GeV]). This method is used in 1FGL catalogue [74] and it is a good estimation because in that catalogue all sources' spectra were fitted using power-law model.

The second method is using full spectral fit to calculate the integral flux. In 2FGL catalogue [73] the problem of spectral fitting only with power-law model is solved. The usage of this method will overcome the limitation problem occurred due to summation procedure and the uncertainty of flux calculation reduced by a factor of 20%.

BL Lacs' integral flux in γ-ray band (f_γ between 1 and 100 [GeV]) are retrieved from 2FGL catalogue [73] and presented in table 8 column 2. Column 3 of table 8 shows the S_γ of each BL Lac in unit of [erg/cm^2/s] which is calculated by assuming the 50 [GeV] as energy indicator of this band.

Totally 38 BL Lacs γ-ray flux was available in 2FGL. Remained four BL Lacs are BZB J0013-1854, 1ES 0229+200, 1ES 0347-121 and PKS 0548-322. These sources are included in *FERMI* third catalogue (private communication with Gino Tosti). Also, BZB J0013-1854 data were present in 1FGL but it is not included in 2FGL catalogue. Being faint in γ-rays band and statistical issues during the data reduction process can be possible reasons for the absence of these BL Lacs in 2FGL catalogue. Distribution of BL Lacs' γ-ray flux illustrated in figure 8 (Left Panel).

Variability is common in γ-ray emitting sources. In 2FGL catalogue γ-ray flux variability of sources are calculated using an interesting procedure. As a building block of this procedure, they use their own residual test statistic method which is used for spectral analysis and flux calculation.

In their procedure each object light-curve is time-binned into 24. Each bin has approximately 1 month length. Normalizations of the object of interest, the diffuse backgrounds, and bright and nearby catalogue sources are allowed to vary. The other parameters which describing spectral shape of the source in region of interest are fixed. Photon flux over full energy range, its error and detection significant are calculated for each time bin. Finally flux variability index ($f_{\gamma,var}$) calculated from the value of the likelihood in the null hypothesis, that the object flux is constant across the full 2-year period, and the value under the alternate hypothesis where the flux in each bin is optimized:

$$f_{\gamma,var} = 2[\log L(\{F_i\}) - \log L(\{F_{const}\})] = 2\sum_i [\log L_i(\{F_i\}) - \log L_i(\{F_{const}\})] \quad (7)$$

where $\log L(\{F_i\})$ is the log likelihood for the full time period and is expressed as a sum of terms for the individual time bands, $\log L_i$. $f_{\gamma,var}$ is distributed as χ^2

with 23 degrees of freedom if the null hypothesis is correct. The value of $f_{\gamma,var} > 41.6$ is used to identify variable sources at a 99% confidence level.

Column 4 in table 8 shows $f_{\gamma,var}$ for the sample. γ-ray flux of 17 BL Lacs are variable in monthly time scale.

Table 8: Gamma-ray properties of BL Lacs[a]

Source Name	$f_\gamma/10^{-9}$ $[Ph/cm^2/s]$	$S_\gamma/10^{-10}$ $[erg/cm^2/s]$	$f_{\gamma,var}$	$\Gamma_{\gamma,t}$	Γ_γ
(1)	**(2)**	**(3)**	**(4)**	**(5)**	**(6)**
BZB J0013-1854					
1ES 0033+595	2.43±0.25	1.95	36.52	PL	1.87±0.07
RGB J0152+017	0.77±0.14	0.62	27.73	PL	1.79±0.14
3C 66A	25.61±0.61	20.51	358.64	LP	1.85±0.02
1ES 0229+200					
RBS 0413	1.06±0.17	0.85	44.09	PL	1.55±0.11
1ES 0347-121					
1ES 0414+009	0.69±0.14	0.56	15.56	PL	1.98±0.16
PKS 0447-439	11.41±0.40	9.14	91.92	PL	1.86±0.02
1ES 0502+675	2.42±0.21	1.94	41.46	PL	1.49±0.07
VER J0521+211	9.04±0.40	7.24	118.72	PL	1.93±0.03
PKS 0548-322					
RGB 0648+152	1.56±0.20	1.25	13.04	PL	1.74±0.11
1ES 0647+250	1.78±0.20	1.43	27.25	PL	1.59±0.08
RGB J0710+591	0.81±0.13	0.65	29.86	PL	1.53±0.12
S5 0716+714	18.33±0.43	14.68	859.73	LP	2.01±0.02
1ES 0806+524	2.45±0.19	1.96	37.80	PL	1.94±0.06
BZB J1010-3119	0.84±0.16	0.67	13.91	PL	2.24±0.14
1ES 1011+496	7.80±0.33	6.25	48.05	LP	1.72±0.04
1ES 1101-232	0.49±0.13	0.40	25.74	PL	1.80±0.21
Markarian 421	29.67±0.61	23.76	112.77	PL	1.77±0.01
Markarian 180	1.15±0.13	0.92	19.67	PL	1.74±0.08
1ES 1215+303	5.49±0.30	4.40	96.20	PL	2.02±0.04
1ES 1218+304	2.81±0.25	2.25	40.00	PL	1.71±0.07
W Comae	5.54±0.28	4.44	111.50	PL	2.02±0.03
PKS 1424+240	11.48±0.40	9.20	77.72	PL	1.78±0.02
H 1426+428	0.75±0.13	0.60	22.16	PL	1.32±0.12
1ES 1440+122	0.45±0.11	0.36	25.10	PL	1.41±0.18
PKS 1440-389	3.25±0.26	2.60	18.48	PL	1.77±0.06

Continued on next page

Table 8: continued from previous page

Source Name	$f_\gamma/10^{-9}$ $[Ph/cm^2/s]$	$S_\gamma/10^{-10}$ $[erg/cm^2/s]$	$f_{\gamma,var}$	$\Gamma_{\gamma,t}$	Γ_γ
(1)	**(2)**	**(3)**	**(4)**	**(5)**	**(6)**
AP Lib	5.16±0.31	4.13	19.11	PL	2.05±0.04
PG 1553+113	14.04±0.46	11.25	93.46	PL	1.67±0.02
Markarian 501	8.77±0.35	7.02	72.33	PL	1.74±0.03
1ES 1727+502	0.81±0.13	0.64	17.60	PL	1.83±0.13
1ES 1741+196	0.63±0.14	0.51	26.49	PL	1.62±0.15
1ES 1959+650	5.88±0.27	4.71	52.30	PL	1.94±0.03
MAGIC J2001+435	11.77±0.44	9.42	117.98	PL	1.90±0.03
PKS 2005-489	3.83±0.26	3.06	68.86	PL	1.78±0.05
PKS 2155-304	23.53±0.57	18.85	262.87	PL	1.84±0.02
BL Lacertae	10.46±0.39	8.38	266.98	LP	2.11±0.04
B3 2247+381	1.09±0.17	0.88	26.96	PL	1.84±0.11
1ES 2344+514	1.55±0.18	1.24	28.13	PL	1.72±0.08
H 2356-309	0.61±0.12	0.49	20.19	PL	1.89±0.17

a- All data are collected from Fermi LAT Second Source Catalog [73] except third column

3.4.3 Gamma-Ray Properties Summary

Sources with higher average flux energy density has more chance to be observed in different levels above the detector sensitivity. This causes the sample γ-ray flux energy density (S_γ) to have a positive trend to variability index of the BL Lacs. The trend is more obvious among the objects which are classified as variable γ-rays sources. Figure 9 left shows the distribution of BL Lacs in S_γ and $f_{\gamma,var}$ plane. The extra major grid line at value of $f_{\gamma,var} = 10^{1.62} = 41.6$ shows the boundary which of flux variability. These two datasets (S_γ and $f_{\gamma,var}$) are not independent therefore the regular statistical test are not applicable to fitted model. To overcome this problem the error part of both sets of data are needed. According to 2FGL catalogue only the error bars of S_γ is available. To calculate the error bars of $f_{\gamma,var}$ observed data for all the sources of the sample should be reduced manually. This work is postponed to the future studies.

Similar work is done for finding correlation between spectral index (Γ_γ) and γ-rays flux variability index ($f_{\gamma,var}$). BL Lacs distribution in Γ_γ and $f_{\gamma,var}$ plane is illustrated in figure 9 right. The extra major grid line at value of $f_{\gamma,var}$ = 41.6 is the boundary indicator of flux variability.

In addition to this a search for finding correlation between γ-rays spectral index (Γ_γ) and γ-ray flux energy density (S_γ) is done. The result of this study is illustrated in figure 9. A peak in f_γ is distinguishable near the spectral index value of 1.8. However, this correlation is not significant and it is mostly dominated by one object (i.e. Markarian 421). The results agree with the analysis done by Senturk et. al. [75]

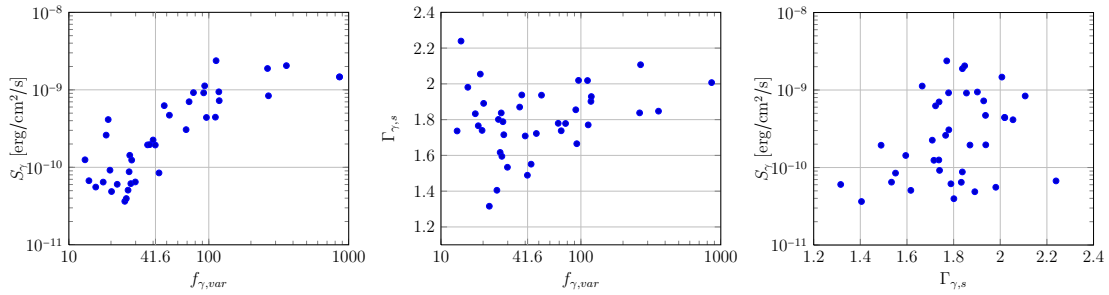

Figure 9. Left: γ-rays flux energy density vs. γ-rays flux variability index [Logarithmic scale]. Middle: γ-rays Spectral Index vs. γ-rays flux variability index [Semi-logarithmic scale]. Right: γ-rays flux energy density vs. γ-rays spectral index [Semi-logarithmic scale].

3.5 Very High Energy Gamma-Ray Properties

There is no good synchronized data for BL Lacs' VHE γ-rays properties. This causes difficulty in presenting collected data from different papers.

Spectral shape of BL Lacs in VHE γ-rays band are described by simple power law model.

$$\frac{dN}{dE} = N_0 \left(\frac{E}{E_t}\right)^{(-\Gamma_V)} \tag{8}$$

Where N_0 is normalization constant in unit of [TeV^{-1}cm^{-2}s^{-1}]. E_t and Γ_V are the pivot energy and slope of fitted spectra accordingly.

Search for VHE γ-rays properties started by collecting integral flux above E_t and spectral index for each source of the sample from published papers and available telegrams[18]. Pivot Energy E_t, which integral flux is calculated above it, is different among the objects, telescopes, observation periods and papers.

To avoid presenting very preliminary data here, VHE γ-rays properties of BL Lacs, available in published papers, are presented in appendix I. These properties are pivot energy (E_t), integral flux over the pivot energy ($f_{V(>E_t)}$) and best fit spectral index (Γ_V). The references are also available in that part. EBL absorption corrected data for TeV BL Lacs are not available in all cases. Also, different EBL models for different objects would result scatter in VHE γ-rays properties. Non-corrected data will lead errors on spectral studies because the corrected spectra is harder than the measured ones and correction increases with redshift. Considering these points, all presented data here are measured properties and they are not corrected by EBL absorption.

E_t = 200 [GeV] is the most frequent pivot energy (17 out of 40) which the VHE γ-rays integral flux of our sample presented above it. Synchronization pivot energy, E_s, is defined to be equal to 200 [GeV] to make data, from different papers, comparable. Integral flux of 23 BL Lacs, which are indicated above pivot energy other than E_s, in their related papers, are extrapolated by using their spectral indices to E_s.

Some of the BL Lacs (17 out of 40) have at least two different value for VHE γ-rays integral flux over synchronization pivot energy($f_{V(>E_s)}$). To simplify our presentation, these BL Lacs are grouped in one category (Group A).

Another group (Group B) is defined to cover VHE γ-rays properties of the BL Lacs, which there is no clear claim about their integral flux variability. 23 objects of in our sample are in this group.

MAGIC J2001+435 and 1ES 0647+250 are two remained objects which are not

[18] `http://www.astronomerstelegram.org/`

categorized in these groups because there is no data available for them. VHE γ-rays properties of MAGIC J2001+435 will be presented in section 4.3.

The detection of 1ES 0647+250 was announced in *"12^{th} International Conference on Topics in Astroparticle and Underground Physics (TAUP 2011)"* [76]. Data reduction for calculating VHE γ-rays properties of this object is not published yet. The only available data is its integral flux over 100 [GeV] $f_{V(>E_{100GeV})}$ = 0.03 [Crab unit] [19] which corresponds to $1.62 * 10^{-11}$ [Ph/cm^2/s]. This object is not categorized to the defined groups because the available data are preliminary and could not be synchronized to the others.

3.5.1 Multiple detected BL Lacs (group A)

BL Lacs in this group could be considered as variable BL Lacs in VHE γ-rays band. Their flux shows at least two different values when they are synchronized to the selected pivot energy. There are lots of observation for some of these sources (e.g. Markarian 421). I consider the highest and lowest observed flux of such sources to have a homogeneous data for comparison.

Table 9 shows data retrieved from different papers for these objects. Column 2 to 4 shows the VHE γ-rays properties of these BL Lacs in the high state. The sub-columns in table 9 under high state include integral flux ($f_{V,H(>E_s)}$) in units of [Ph/cm^2/s] (column 2), flux energy density ($S_{V,H(>E_s)}$) in units of [erg/cm^2/s] (column 3) and spectral index $\Gamma_{V,H}$ (column 4).

Column 5 to 7 in table 9 shows the data for the same sources in their lowest detected state. The distribution of sub-columns are as the same as high state. These sub-columns are $f_{V,L(>E_s)}$ in units of [Ph/cm^2/s], $S_{V,L(>E_s)}$ in units of [erg/cm^2/s] and spectral index $\Gamma_{V,L}$ accordingly.

[19] `http://tevcat.uchicago.edu/?mode=1&showsrc=238`

Table 9: VHE γ-rays properties of BL Lacs (group A)

Source Name	**High State**			**Low state**			$f_{V,var}$
	$f_{V,H(>E_s)}/10^{-11}$ $[Ph/cm^2/s]$	$S_{V,H(>E_s)}/10^{-11}$ $[erg/cm^2/s]$	$\Gamma_{V,H}$	$f_{V,L(>E_s)}/10^{-11}$ $[Ph/cm^2/s]$	$S_{V,L(>E_s)}/10^{-11}$ $[erg/cm^2/s]$	$\Gamma_{V,L}$	
(1)	**(2)**	**(3)**	**(4)**	**(5)**	**(6)**	**(7)**	**(8)**
3C 66A	2.50	0.80	4.10±0.6	0.39	0.12	4.10±0.4	6.41
VER J0521+211	7.08	2.27	3.25±0.72	1.93	0.62	2.92±0.34	3.67
S5 0716+714	4.10	1.31	3.45±0.54	0.44	0.14	3.45±0.54	9.38
1ES 0806+524	2.45	0.79	3.20±0.3	0.45	0.15	2.70±0.4	5.41
1ES 1011+496	7.70	2.47	3.01	1.58	0.51	4.00±0.5	4.87
Markarian 421	232.65	74.55	2.20	10.00	3.20	2.20±0.8	23.27
1ES 1215+303	0.77	0.25	2.96±0.14	0.34	0.11		2.26
1ES 1218+304	2.18	0.70	3.00±0.4	1.22	0.39	3.07±0.09	1.78
W Comae	6.22	1.99	3.68±0.22	1.99	0.64	3.81±0.35	3.13
PKS 1424+240	0.53	0.17	5.00±1.7	0.26	0.08	3.50±1.2	2.03
H 1426+428	66.21	21.22	3.50±0.35	0.41	0.13	3.50±0.35	163.43
PG 1553+113	2.43	0.78	4.50±0.21	0.57	0.18	4.10±0.3	4.23
Markarian 501	98.06	31.42	2.06±0.13	5.62	1.80	2.72±0.15	17.44
1ES 1959+650	48.89	15.67	2.83±0.14	2.41	0.77	2.58±0.18	20.29
PKS 2155-304	172.00	55.12	3.19±0.02	5.56	1.78	3.34±0.05	30.94
BL Lacertae	34.00	10.89	3.60±0.4	0.60	0.19	3.60±0.5	56.67
1ES 2344+514	13.91	4.46	2.78±0.09	0.55	0.18	2.40±0.4	25.29

Finally column 8 shows the flux variability amplitude of these objects. $f_{V,H(>E_s)}$ is divided by $f_{V,L(>E_s)}$ in [Ph/cm^2/s] unit for each BL Lac to calculate its variability amplitude.

Raw data from published papers, which the above data are retrieved from them, are presented in appendix I. Related references for these data are also available in appendix I.

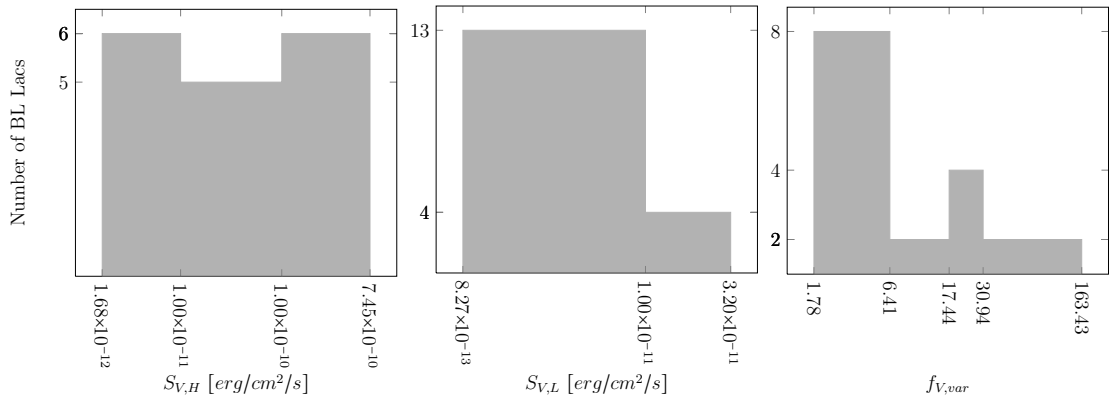

Figure 10. Left: VHE γ-rays high state flux energy density. Middle: VHE γ-rays low state flux energy density. Right: VHE γ-rays integral flux variability amplitude

Distribution of flux energy density over the synchronization pivot energy in high state, low state and integral flux variability amplitude are shown in figure 10. The low state histogram shows a significant drop in number of BL Lacs when flux energy density magnitude increases. For high state the distribution is smoother than the low state. Distribution of variability amplitude shows mostly moderate values similar to those seen in X-rays.

3.5.2 Single detected BL Lacs (group B)

There is no clear claim on integral flux variability of 23 objects from our sample. For some sources, there is only one observation available. For other sources, VHE γ-rays emission is steady during the available observations.

Column (1) in table 10 indicates sources name which are categorized in this group. Spectral index, Γ_V, are presented in column (2). Columns (3) and (4) shows

these sources integral flux ($f_{V(>E_s)}$) in [Ph/cm^2/s] and flux energy density ($S_{V(>E_s)}$) in [erg/cm^2/s] units accordingly.

Table 10: VHE γ-rays properties of BL Lacs (group B)

Source Name	$\Gamma_{V,s}$	$f_{V(>E_s)}/10^{-12}$ $[Ph/cm^2/s]$	$S_{V(>E_s)}/10^{-12}$ $[erg/cm^2/s]$
(1)	**(2)**	**(3)**	**(4)**
BZB J0013-1854	3.40±0.50	2.38	0.76
1ES 0033+595	3.80±0.70	3.17	1.02
RGB J0152+017	2.95±0.36	5.95	1.91
1ES 0229+200	2.50±0.19	4.64	1.49
RBS 0413	3.18±0.68	2.44	0.78
1ES 0347-121	3.10±0.23	5.30	1.70
1ES 0414+009	3.45±0.25	1.88	0.60
PKS 0447-439	4.36±0.49	16.7	5.36
1ES 0502+675	3.92±0.35	25.4	8.17
PKS 0548-322	2.86±0.34	4.09	1.31
RGB 0648+152	4.40±0.80	7.54	2.42
RGB J0710+591	2.69±0.26	7.74	2.48
BZB J1010-3119	3.08±0.42	2.35	0.75
1ES 1101-232	2.94±0.20	4.50	1.44
Markarian 180	2.80±0.70	22.5	7.21
1ES 1440+122	3.40±0.70	2.28	0.73
PKS 1440-389		6.85	2.20
AP Lib	2.50±0.20	4.77	1.53
1ES 1727+502	2.70±0.50	2.60	0.83
1ES 1741+196	2.70±0.47	1.94	0.62
PKS 2005-489	3.20±0.16	11.8	3.78
B3 2247+381	3.20±0.50	5.00	1.60
H 2356-309	3.06±0.15	4.45	1.43

Distributions of BL Lacs' spectral index and integral flux energy density are illustrated in figure 11.

It is notable that there is no published data for spectral index of PKS 1440-389 within the papers and web resources. In addition, this object is deleted from TeV catalogue. According to private communication with Henri, G. (member of HESS collaboration) this source is detected in VHE γ-rays band but the data reduction

and analysis process is not completed yet.

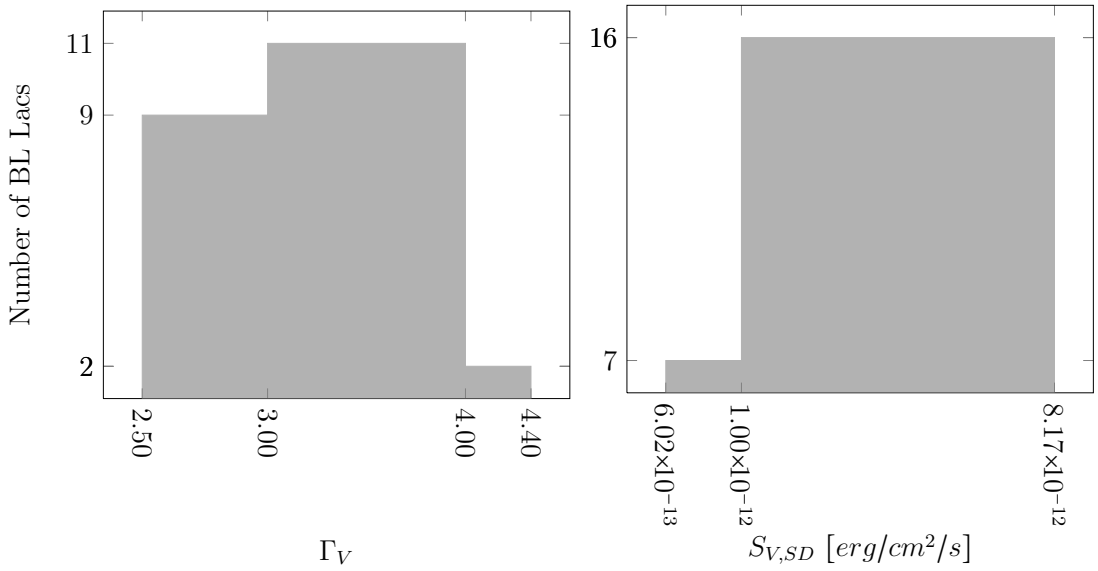

Figure 11. Distribution of VHE γ-rays properties of BL Lacs' (Group B). Left: VHE γ-rays spectral index Right: VHE γ-rays flux energy density.

By comparing integral flux of both groups it is clear that group A are generally brighter sources in VHE γ-rays band. However, the faintest detected BL Lac is PKS 1424+240 which is in group A. Also this object is the farthest BL Lac. In group B, 1ES 0414+009 is the faintest BL Lacs. Markarian 421 is the brightest ever detected object in this band. However, PKS 2155-304 is the second bright source in this band.

3.6 Objects' luminosity

Objects' luminosity in the selected wavelengths are presented in table 11. The values in this table calculated from previously presented objects' fluxes and luminosity distances in section 3.1.3 by using equation (1). In this table, VHE γ-rays data are presented in last three column according to previously defined subclasses (i.e. multiple detected high state, multiple detected low state and single detected)

Table 11: BL Lacs luminosity in different wavelengths[a]

Source Name	L_R 10^{42}	L_O 10^{45}	L_X 10^{45}	L_γ 10^{46}	$L_{V,H}$ 10^{45}	$L_{V,L}$ 10^{44}	$L_{V,SD}$ 10^{44}
BZB J0013-1854	0.052	1.216					0.187
1ES 0033+595	1.789	0.352	18.26	6.043			3.152
RGB J0152+017	0.044	0.927	0.046	0.105			0.325
3C 66A	15.61	14.33	1.661	81.90	3.198	4.989	
1ES 0229+200	0.124	0.031	0.828				0.827
RBS 0413	0.118	0.097	0.773	0.936			0.863
1ES 0347-121	0.042	0.399	0.647				1.833
1ES 0414+009	0.951	1.203	2.352	1.558			1.687
PKS 0447-439	1.465	1.958	0.994	11.96			7.007
1ES 0502+675	0.805	2.485	12.75	12.88			54.25
VER J0521+211	0.829	0.221	1.013	2.336	0.731	1.995	
PKS 0548-322	0.104	0.114	0.545				0.174
RGB 0648+152	0.314	0.312		1.211			2.338
1ES 0647+250	2.459	4.151		9.177			
RGB J0710+591	0.173	0.525		0.286			1.095
S5 0716+714	12.78	32.13	3.243	49.088	4.391	4.684	
1ES 0806+524	0.462	0.614	0.469	1.056	0.423	0.782	
BZB J1010-3119	0.212	0.612		0.397			0.445
1ES 1011+496	1.956	1.911	0.508	8.809	3.478	7.138	
1ES 1101-232	0.337	0.063	3.876	0.417			1.519
Markarian 421	0.084	0.211	1.268	0.568	1.781	0.765	
Markarian 180	0.071	0.039	0.273	0.049			0.388
1ES 1215+303	1.038	0.734	0.077	2.115	0.119	0.524	
1ES 1218+304	0.279	0.548	1.522	2.317	0.717	4.020	
W Comae	1.386	0.567	0.015	1.293	0.581	1.858	
PKS 1424+240	24.82	61.50	3.239	148.9	2.726	13.40	
H 1426+428	0.087	0.105	0.487	0.286	10.03	0.614	
1ES 1440+122	0.191	0.243		0.287			0.576
PKS 1440-389	0.049	0.095		0.287			0.242
AP Lib	0.573	0.116	0.033	0.243			0.090
PG 1553+113	18.19	34.68	2.763	66.14	4.577	10.81	
Markarian 501	0.192	0.061	0.189	0.203	0.907	0.520	
1ES 1727+502	0.060	0.035	0.069	0.050			0.065
1ES 1741+196	0.303	0.082	0.127	0.093			0.114
1ES 1959+650	0.069	0.098	0.403	0.264	0.880	0.434	
MAGIC J2001+435	1.114	0.691	0.144	10.41			6.369

Continued on next page

Table 11: continued from previous page

Source Name	L_R 10^{42}	L_O 10^{45}	L_X 10^{45}	L_γ 10^{46}	$L_{V,H}$ 10^{45}	$L_{V,L}$ 10^{44}	$L_{V,SD}$ 10^{44}
PKS 2005-489	0.739	0.024	0.643	0.407			0.502
PKS 2155-304	0.742	4.503	2.858	7.087	20.72	6.699	
BL Lacertae	2.178	0.365	0.140	1.047	1.362	0.240	
B3 2247+381	0.229	0.115	0.271	0.348			0.636
1ES 2344+514	0.055	0.104	0.010	0.061	0.219	0.086	
H 2356-309	0.251	0.333	4.286	0.394			1.154

a- All values are in [erg/s] unit.

PKS 1424+240 is the most luminous object in radio, optical, γ-rays and VHE γ-rays low state. 1ES 0033+595, PKS 2155-304 and 1ES 0502+675 are the most luminous object in X-rays, VHE γ-rays high state and VHE γ-rays single detected accordingly.

The lowest luminosity objects are: 1ES 0347+121 in radio; PKS 2005-489 in optical; Markarian 180 in γ-rays; 1ES 1727+502 in VHE γ-rays single detected. 1ES 2344+514 has the lowest luminosity in X-rays and VHE γ-rays high and low state.

4 Step II: Is MAGIC J2001+435 a typical TeV BL Lac?

In this section, MAGIC J2001+435 is introduced qualitatively. Then X-rays analysis, which lead to compute X-rays properties of this source, is presented. VHE γ-rays analysis of this source is presented based on an unpublished paper from *MAGIC* collaboration. At the end summary of results and conclusions are presented.

4.1 Introduction

MAGIC J2001+435 was little studied before its detection in γ-rays band. Its location, which is near to the galactic plane, is one the reasons which causes lack of study. This source had been considered a radio source with unknown redshift near the galactic plane. *"Fermi Large Area Telescope Bright Gamma-ray Source List"* [77] contains 37 unassociated sources from total number of 205 sources. This source was classified as unassociated in this catalogue. After this classification a new era of this source study started. Next two paragraph contains most significant data of this source before its new era.

The first available data for MAGIC J2001+435 released in 1991 as a radio source in *"The 87GB catalog of radio sources covering delta between 0 and + 75 deg at 4.85 GHz"*. This catalogue contains sources data from NRAO 91m telescope located in Green Bank survey which are observed during October 1987 [42].

"The first XMM-Newton slew survey catalogue: XMMSL1" contains the first X-ray band data of this source [78].

It is notable that before the new era of this source there is no attempt for classification of this source. Locating in populated region in the sky, near to galactic plane, causes having uncertainty of counterparts in other wavelengths to confirm its the classification of this source. This leads this source to be left as an orphan for

long time.

Bassani, L. et al. resolved this source type in their paper, *"On the identification of the Fermi/LAT source 0FGL J2001.0+4352 with a BL Lac"* [10]. They used XMM-Newton and Swift/XRT data to localise the X-ray counterpart. Then, they characterised its X-ray spectrum. Afterwards they identified its radio counterpart from NVSS (NRAO VLA Sky Survey [79]) data at 1.4 GHz.

Finally, an optical follow-up observation with the telescope at Bologna Astronomical Observatory was done. A nearly featureless spectra in optical band retrieved from these observation. Only the Galactic diffuse interstellar and the atmospheric telluric lines are apparent in spectrum. No other emission or absorption lines were detected. There seems to be a slope change in the optical spectrum near the 6.24×10^{14}Hz. This may be due to a non-thermal component which merges with the light from the host galaxy. The spectrum is intrinsically blue and is similar to those of BL Lacs. AGN classification approach of Laurent-Muehleisen et al. (1998) also confirmed this classification [10].

It is not clear that this source is a typical TeV BL Lac. Answering to this question is covered by this thesis as a subsidiary aim in this section.

There is an estimation of redshift ~ 0.2 in Bassani et al. paper [10]. The host galaxy is resolved in June 13, 2013. Deep optical R-band images obtained with Nordic Optical Telescope (Kari Nilsson private communication). The preliminary results show that the host galaxy redshift of this source is $z = 0.19 \pm 0.04$ which is in good agreement with the Bassani redshift estimation in 2009.

4.2 X-ray Analysis

Available X-ray data for MAGIC J2001+435 were not too many at beginning time of the thesis. The available data can not be synchronized to the other objects collected data. Therefore we analysed the X-rays data of the source.

In this section data reduction procedure which is used to reduce needed X-ray data of MAGIC J2001+435 is discussed qualitatively. Then validation of data reduction procedure will be checked using observed data of two other BL Lacs in our sample. They are BL Lacertae and Markarian 180. The last part contains X-ray data of MAGIC J2001+435, reduced by validated reduction procedure.

4.2.1 X-ray data reduction procedure

NASA developed all of the data reduction tools for their different telescopes under a unified scheme data reduction tool called HEAsoft. As the first step of data reduction for these objects, I attempt to use the online data reduction tool of HEAsoft (WebHera). After a long try to use the related pipeline to reduce data for *SWIFT-XRT* data, it is found that there is no way of reaching to the goal of data reduction using online tool. Internet security matter from NASA server forced them to restrict data analysis for one of the sub-applications (XIMAGE) in the XRTPIPLINE.

I used HEAsoft on a local machine to run the XRTPIPELINE to reduce my data in the second step. But this approach also failed. XRTPIPELINE do not show the details of spectrum analysis. It just show you a visual view of final spectrum. The final approach which leads to the result was using applications one by one to reduce data. They are introduced in appendix II together with data reduction procedure steps.

4.2.2 Data reduction procedure validity check

HEAsoft version 6-13 which contains XSELECT version 2.4b, XRTEXPOMAP version 0.2.7, XRTMKARF version 0.6.0, GRPPHA version 3.0.1 and XSPEC version 12.8.0 is used to reduce the following data.

To approach a correct data reduction procedure two sources from the sample with known X-rays properties are selected. Sample restricted to the sources which

their data retrieved from Giommi, P., et.al., 2011 [61]. This paper contains X-ray properties of 14 TeV BL Lacs.

BL Lacertae is chosen as one of our candidate to check the data reduction procedure. This object, like MAGIC J2001+435, located near the galactic plane. BL Lacertae is brighter than the other objects, which their spectra are fitted by power law model.

Markarian 180 was another source for checking the data reduction procedure. Its spectra is fitted by log parabola model. It is not located near to galactic plane. In comparison to other objects which fulfils these criteria this object is not too bright.

Giommi, P., et al., 2011 [61] used the *SWIFT* observation data on December 23, 2009 to reduced the data for BL Lacertae X-rays properties. For Markarian 180 *SWIFT* observation data on October 28, 2009 are used. First two row in table 12 shows X-ray properties analysed by them.

For BL Lacertae data from the SWIFT-XRT database with the observation ID "00035028039", which is related to the one in Giommi, P. paper, are downloaded. The procedure is applied to it considering source region as a circle with 47" radius. According to the count rate obtained after extracting spectrum of the source (Step 7), there is no need of pile up thread for this source. Using the latest response matrix file (swxpc0to12s6_ 20010101v014.rmf) from SWIFT-XRT calibration files[20] data were fitted by a photoelectric absorbed power law model leaving the hydrogen-equivalent column density (N_H) as a free parameter. The model kept similar to the ones used in Giommi, P. et al. paper.

All of the obtained data are in good agreement with the data from Giommi, P., et al., 2011 [61]. Comparing two sets of data shows that my reduced data are more accurate than those presented in Giommi, P., et al. paper. This can be concluded from the smaller error bars and reduced χ^2 with the same degree of freedom in my

[20] `http://heasarc.gsfc.nasa.gov/docs/heasarc/caldb/data/swift/xrt/index.html`

data reduction.

Table 12: X-ray properties of BL Lacertae and Markarian 180

Source Name	$\Gamma_{X,t}$	Γ_X	$\Gamma_{X,c}$	$N_H/10^{21}$ $[cm^{-2}]$	S_X $[erg/cm^2/s]$	$[\chi^2_{Re}/dof]$
(1)	**(2)**	**(3)**	**(4)**	**(5)**	**(6)**	**(7)**
Data from Giommi, P., et al., 2011 [61]						
Markarian 180	LP	$1.86^{+0.05}_{-0.05}$	$0.66^{+0.13}_{-0.13}$	0.12	$50.7 * 10^{-12}$	1.17/164
BL Lacertae	PL	$1.88^{+0.25}_{-0.23}$		$2.93^{+0.90}_{-0.25}$	$11.2 * 10^{-12}$	0.47/21
Results of current work data reduction						
Markarian 180	LP	$1.86^{+0.05}_{-0.05}$	$0.46^{+0.13}_{-0.13}$	0.12	$65.0 * 10^{-12}$	0.96/61
BL Lacertae	PL	$1.76^{+0.13}_{-0.13}$		$2.51^{+0.45}_{-0.45}$	$10.9 * 10^{-12}$	0.35/21

For Markarian 180 data from the *SWIFT-XRT* database with the observation ID "00035015025", which is related to the one in Giommi, P. paper, are downloaded. Due to the high count rate of this source image has been piled up considering a ring centred at source position instead of a circle. The ring has inner radius of 30.68" and 70.8" is the value for outer radius of it. The above mentioned procedure is applied to reduce the data of the this object. For the response matrix file the latest one was used like the BL Lacertae. Similar to the Giommi, P. et al. paper, data were fitted by a photoelectric absorbed log parabola model by fixing the value of hydrogen-equivalent column density (N_H) to 0.12×10^{21} [cm^{-2}]. Following are results of my data reduction.

The fitted model is valid. The fitted parameters (i.e slope and curvature of spectra) are within the error bars of two model fittings. The difference in Reduced χ^2 and d.o.f. values comes from the pileup threads which are used. As this source is bright number of saturated pixel on CCD is high. This will cause model fitting to be very sensitive to the pile up threads.

The above mentioned results from data reduction of these two sources confirms that the used procedure is correct and leads to correct spectrum fitting results. All of the calculated parameters are presented in bottom part of table 12.

4.2.3 MAGIC J2001+435 X-rays data

For MAGIC J2001+435 data from the SWIFT-XRT database with the observation ID "00039229006" are downloaded. Downloaded data are related to the night of detection of this source in VHE γ-rays band, July 16, 2010. Leaving Hydrogen-equivalent column density as free parameter, observation data were fitted by both models to find which model fitted better to the object spectra. The best fit model is power law with the following characteristic:

- Best fit photon index calculated to be 2.77 ± 0.31
- Hydrogen-equivalent column density (N_H) is equal to $(3.75 \pm 0.75) \times 10^{21}$ [cm^{-2}]
- X-ray integral flux in $(2 - 10$ [KeV]) range is $(1.328^{+0.348}_{-0.244}) \times 10^{-12}$ [erg/cm^2/s]
- The parameters which shows the correctness of the above data are Reduced $\chi^2 = 1.051$ for 11 Degrees of Freedom (d.o.f.).

The reduced data are compatible with an unpublished paper from *MAGIC* collaboration.

Following the *"FERMI Large Area Telescope First Source Catalog"* [74] *SWIFT* carried out some observation on this source during January 21, 2009 and September 18, 2010 [21]. MAGIC J2001+435 light-curve is illustrated in figure 12. Data of this light-curve are extracted from *"Swift-XRT Monitoring of Fermi-LAT Sources of Interest"* [58]. The average count rate (0.03-10 KeV) is 0.067 (count/s). X-ray count rate during the night of detection in VHE γ-rays (July 16, 2010) is higher than the average count rate with a factor of 1.34. On July 29, 2010 the X-ray flux is much higher by a factor of 4.26 of average count rate.

[21] `http://heasarc.gsfc.nasa.gov/W3Browse/swift/swiftxrlog.html`

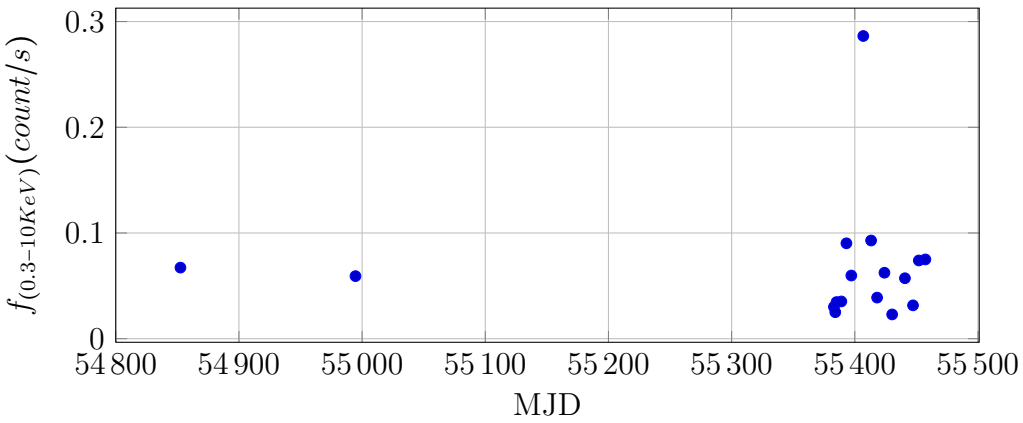

Figure 12. MAGIC J2001+435 X-ray light-curve [Linear scale]

4.3 Very High Energy Gamma-Ray properties

As a part of thesis project, I analysed the VHE γ-rays data of July 16, 2010 observed by *MAGIC*, but due to technical problems the analysis was not complete. This section contains some information from *MAGIC* collaboration's unpublished paper indicated with "[80]".

The geographical position of *MAGIC* is 28.8° north and 17.8° west at altitude of 2200 meters above sea level. Its lowest operative energy threshold is ~ 50 [GeV]. For a source, which exhibits an integral flux of 0.8% of Crab Nebula flux above 290 [GeV], *MAGIC* has a sensitivity to detect 5 standard deviation (σ) signal by 50 hours observation in stereoscopic mode [81].

Using wobble mode, MAGIC J2001+435 was observed for 9.0 hours during November 7 to 26, 2009 at zenith angle between 20° and 40°. Another observation was carried out by MAGIC on this source for 14.4 hours during July 6 and September 8, 2010 at zenith angle between 15° and 30°. To minimize systematic errors originating from possible exposure inhomogeneities, Direction of wobble offset between two symmetric sky locations was alternated every 20 minutes. Using standard analysis chain with MAGIC Analysis and Reconstruction Software (MARS) observation data are analysed. The followings are results of this data analysis [80].

Calculated significance level of excess is only 1.8σ above energy threshold of 100 [GeV] for the first period of observation (November 2009). For the second period of observation (July-September 2010) calculated significance level of excess is only 1.1σ above energy threshold of 70 [GeV] if one night (July 16, 2010) excluded from whole observations. But during July 16, 2010 night the excess of events N_{ex} = 125.0 ± 20.2 and correspondent calculated significance level of excess is 6.3σ above energy threshold of 70 [GeV]. The effective observation time for July 16, 2010 was 1.36 hours. The source spectrum is fitted with power law model with N_0 = $(1.9 \pm 0.4) \times 10^{-10}$ [$\mathrm{TeV^{-1}cm^{-2}s^{-1}}$], E_t = 200 [GeV] and Γ_V = (2.8 ± 0.4) [22]. Source integral flux over 200 GeV is equal to ($f_{V,>200GeV} = (1.8 \pm 0.5) \times 10^{-11}$ [$\mathrm{Ph/cm^2/s}$]) for July 16, 2010. No statically significant intra-night variability is detected for the source.[80].

4.4 Summary and conclusions

The source redshift (z = 0.19) is in the range of most populated part of sample ($z < 0.2$). There are 32 objects in this range.

This source is categorized as an IBL in *FERMI second AGN catalogue* [23]. However, no value presented for its synchrotron peak frequency. There are only 4 IBLs in our sample other than MAGIC J2001+435.

Radio flux energy density is ~ 51% of whole sample average ($S_{R,ave} = 1.99 \times 10^{-14}$ [$\mathrm{erg/cm^2/s}$]). Radio flux energy density value $S_R = 10.0881 \times 10^{-15}$ [$\mathrm{erg/cm^2/s}$] located on the edge of second part of sample distribution ($1.00 \times 10^{-14} \leq S_R < 6.65 \times 10^{-14}$ [$\mathrm{erg/cm^2/s}$]). 22 Objects have radio flux less than this source. Meanwhile, 19 objects have radio flux higher than this object.

Optical flux energy density is ~ 31% of whole sample average ($S_{O,ave} = 1.99 \times 10^{-11}$ [$\mathrm{erg/cm^2/s}$]). Optical flux energy density value $S_O = 6.26 \times 10^{-12}$ [$\mathrm{erg/cm^2/s}$] located in near to the upper border of second part of distributions ($1 \times 10^{-12} \leq S_O < 1 \times 10^{-11}$

[22] Please see section 3-5 for equation of power law model.

[erg/cm^2/s]). 16 Objects have optical flux energy density less than this source. Optical flux variability lays in the most populated group of sample $0.5 \leq (f_{O,var} = 0.95) < 1$. It is notable that the data for optical flux energy density of this source is from Tuorla blazar monitoring program, Which start monitoring this source 29 days after its discovery in VHE γ-rays band. Considering optical and VHE γ-rays light curves connection, the $f_{O,var}$ value can be more than the value presented here.

Figure 13 shows R-band optical light-curve of this source during the August 14, 2010 and June 12, 2012 from Tuorla blazar monitoring program. The optical light-curve show that the source has a yearly decreasing optical flux after its detection in VHE γ-rays band.

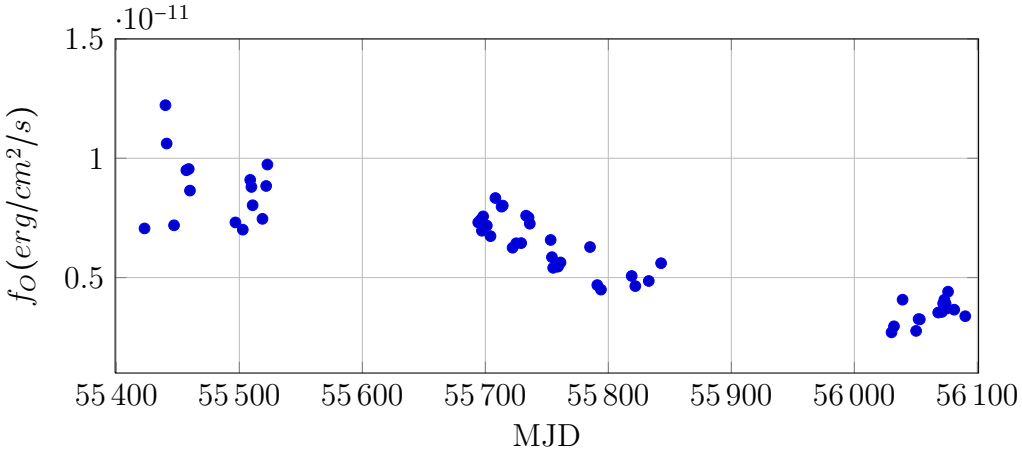

Figure 13. MAGIC J2001+435 R-band optical light-curvel [Linear scale]

X-rays flux is ~ 3% of whole sample average ($S_{X,ave} = 3.52 \times 10^{-11}$ [erg/cm^2/s]). X-rays flux energy density value $S_X = 1.30 \times 10^{-12}$ [erg/cm^2/s] located on the edge of whole sample. This source is the second faintest source of sample. Its X-rays flux variability amplitude is in the second most populated group of sample $5 \leq (f_{X,var} = 12.81) < 20$. Also it has the softest spectra in X-rays within the sample.

γ-rays flux energy density is ~ 53% higher than whole sample average ($S_{\gamma,ave} = 4.98 \times 10^{-10}$ [erg/cm^2/s]). γ-rays flux energy density value $S_\gamma = 9.42 \times 10^{-10}$ [erg/cm^2/s] located on the upper side of most populated part of distributions. This source is 1

of the 17 variable sources of the sample with the $f_{\gamma,var}$ = 117.98. Only 5 objects have γ-rays flux energy density and flux variability more than this source. All objects, which have γ-rays flux energy density more than this source, are not the same as the objects which are more variable in γ-rays. γ-rays spectra is softer than the average. However, 11 sources in the sample have softer spectra than this source.

There are two approach to compare VHE γ-rays flux energy density with the ones of sample. In the former, it is assumed that single detected sources in VHE γ-rays (group B) are faint sources which are observed in their high state. Therefore, VHE γ-rays flux energy density average of whole sample, considering high state flux of group A and group B fluxes is ($S_{V,ave} = 5.26 \times 10^{-11}$ [erg/cm^2/s]) and this source has a flux energy density of $\sim 11\%$ sample average. 23 objects have VHE γ-rays flux energy density less than it. VHE γ-rays spectral index is harder than the average spectral index in this band. But 9 sources in the sample have harder spectra than this source.

In the later approach, it is assumed that single detection of group B is due to lack of observation. Therefore, behaviour of the sources in group B are like the low state of group A. This matter will be discussed in section 5. Considering this assumption VHE γ-rays flux energy density average of whole sample is ($S_{V,ave} = 4.35 \times 10^{-12}$ [erg/cm^2/s]) and this source has flux energy density higher than the average by factor of $\sim 75\%$. 9 objects have VHE γ-rays flux energy density higher than it. Due to lack of information about low state spectral index of the sample, comparing the source spectral index is ignored.

Both approach shows typical behaviour of this source in comparison to whole sample.

MAGIC telescope did not observe this source during its X-ray outburst, on July 29, due to bad weather condition. Also observation in VHE γ-rays band carried out during the rise in optical light curve near September 1, 2010 did not show significant

signal in VHE γ-rays.

From these comparisons, it can be concluded that MAGIC J2001+435 is a typical TeV BL Lac even if it had not been in BL Lacs catalogues. However for some of the properties this source located on the edge of whole sample (e.g. X-rays flux).

5 Step III: TeV BL Lacs population study

To pave the way for prediction method building, different properties of BL Lacs should be studied carefully. Finding correlations between different wavelengths is the first step in this approach.

5.1 Introduction

Flux energy density data for 5 different bands are presented in chapter 3. Radio (S_R), Optical (S_O), X-rays (S_X) fluxes are homogeneous but the error bars for these data are not available. γ-rays flux (S_γ) data are homogeneous and includes error bars.

Flux energy density data in VHE γ-rays are inhomogeneous but the error bars are available for them. To overcome this issue we consider three homogeneous dataset from VHE γ-rays Flux energy density. Dividing group A into High state ($S_{V,H}$) and Low state ($S_{V,L}$) two homogeneous data set become available. The third homogeneous dataset is group B ($S_{V,SD}$). Two more datasets are built by considering combination of group B with each state of group A. These combinations are named as $S_{V,(SD+H)}$ and $S_{V,(SD+L)}$.

Spectral indices slopes are available in three bands (Γ_X, Γ_γ and $\Gamma_{V,(H+SD)}$). Difference of VHE γ-rays spectral index values between group A High and Low states are within their error bars except for one data point. Combination of VHE γ-rays spectral index group A (High State) and group B is considered as VHE γ-rays spectral index dataset.

There are totally 12 datasets available (nine flux energy densities and three spectral index slope datasets). Number of datasets and possible correlations for cross band luminosity is same as the ones for flux energy densities. Therefore, number of possible cross band correlations is 55 (26 for flux energy densities, 26 for luminosities and 3 for spectral indices).

A Fortran 90 code is used to fit trend lines to each pair of dataset. The code is written based on linear least square regression. The best fitted line can be expressed by the following equation:

$$Y = aX + b \tag{9}$$

where a is the slope of fitted line and b is the Y-interception of line when $X=0$.

Power law model can be expressed as:

$$Y = bX^a, \tag{10}$$

where a is the power law index and b is the normalization factor of fitted model when $X=0$. Applying logarithm on both side of this equation we will have:

$$\ln(Y) = \ln(b) + a\ln(X), \tag{11}$$

If we consider new parameters $Y' = \ln Y$, $b' = \ln b$ and $X' = \ln X$ the power law formula become linear.

$$Y' = aX' + b', \tag{12}$$

By applying linear least square regression to this equation we can calculate the parameters which describe the power law model as well. In this method error bars value divided by value of data point considered as the error bars in power law model. This method of error conversion is accurate when the converted error bars has a value less than 0.01.

Calculating Pearson Correlation Coefficient (PCC) gives leads to the answer of how much one datasets is correlated to another. This coefficient varies between -1 to 1. If the coefficient is equal to 1 it means that datasets has positive correlation. Zero value shows that there is no correlation between datasets. Finally, -1 value shows the correlation is negative[23]. I set boundary values for no (< 0.32), weak

[23] http://en.wikipedia.org/wiki/Pearson_product-moment_correlation_coefficient

(0.32-0.67) and strong (> 0.67) correlations considering this distributions and the general concept of PCC. With this approach the significance of fitted models can be compared with each other. PCCs for each pair of datasets are calculated using LibreOffice CALC (Version: 3.4.4) software[24].

Table 13 shows correlation study results for all the selected pair of datasets. Columns 1 and 2 present parameters which considered to find correlation between them. Column 3 and 4 show PCC values for linear and power law model accordingly. Column 5 present which model has more correlation based on the values of two previous columns. Finally, parameters which describe the selected model are presented in column 6 and 7.

Table 13: Cross band correlations study results

Parameters		**PCC**		**Best fitted model paramters**		
X	**Y**	**L**	**PL**	**M.**	**a**	**b**
S_R	S_O	0.223	0.536	PL	$5.39 * 10^{-1}$	$3.46 * 10^{-4}$
L_R	L_O	0.953	0.755	L	$2.08 * 10^{3}$	$-6.01 * 10^{44}$
S_R	S_X	0.055	0.018	L	$1.45 * 10^{2}$	$3.19 * 10^{-11}$
L_R	L_X	0.113	0.377	PL	$3.81 * 10^{-1}$	$7.48 * 10^{28}$
S_R	S_γ	0.329	0.701	PL	$4.55 * 10^{-1}$	$1.54 * 10^{-3}$
L_R	L_γ	0.972	0.894	L	$5.07 * 10^{4}$	$-1.07 * 10^{46}$
S_R	$S_{V,H}$	0.059	0.120	PL	$-4.18 * 10^{-1}$	$2.42 * 10^{-16}$
L_R	$L_{V,H}$	0.024	0.322	PL	$2.12 * 10^{-1}$	$1.94 * 10^{36}$
S_R	$S_{V,L}$	0.041	0.205	PL	$-1.46 * 10^{-1}$	$6.36 * 10^{-14}$
L_R	$L_{V,L}$	0.817	0.727	L	$4.17 * 10^{1}$	$1.52 * 10^{44}$
S_R	$S_{V,SD}$	0.052	0.185	PL	$2.79 * 10^{-1}$	$1.58 * 10^{-8}$
L_R	$L_{V,SD}$	0.289	0.568	PL	$7.51 * 10^{-1}$	$6.81 * 10^{12}$
S_R	$S_{V,(SD+H)}$	0.189	0.465	PL	$6.04 * 10^{-1}$	$1.68 * 10^{-3}$
L_R	$L_{V,(SD+H)}$	0.186	0.556	PL	$6.67 * 10^{-1}$	$4.67 * 10^{16}$
S_R	$S_{V,(SD+L)}$	0.154	0.337	PL	$2.48 * 10^{-1}$	$6.89 * 10^{-9}$
L_R	$L_{V,(SD+L)}$	0.235	0.646	PL	$5.77 * 10^{-1}$	$1.08 * 10^{20}$
S_O	S_X	0.413	-0.094	L	1.27	$8.24 * 10^{-12}$
L_O	L_X	0.110	0.398	PL	$3.45 * 10^{-1}$	$2.18 * 10^{29}$
S_O	S_γ	0.786	0.686	L	9.86	$6.21 * 10^{-11}$

Continued on next page

[24] http://en.wikipedia.org/wiki/LibreOffice_Calc

Table 13: continued from previous page

Parameters		PCC		Best fitted model paramters		
X	**Y**	**L**	**PL**	**M.**	**a**	**b**
L_O	L_γ	0.944	0.880	L	$2.25 * 10^{1}$	$1.45 * 10^{46}$
S_O	$S_{V,H}$	0.577	0.137	L	$1.05 * 10^{-1}$	$1.25 * 10^{-12}$
L_O	$L_{V,H}$	0.074	0.468	PL	$2.78 * 10^{-1}$	$4.47 * 10^{32}$
S_O	$S_{V,L}$	0.485	0.230	L	$1.26 * 10^{-1}$	$-7.26 * 10^{-13}$
L_O	$L_{V,L}$	0.836	0.818	L	$1.92 * 10^{-2}$	$1.78 * 10^{44}$
S_O	$S_{V,SD}$	-0.077	0.105	PL	$-1.11 * 10^{-1}$	$9.53 * 10^{-14}$
L_O	$L_{V,SD}$	0.722	0.571	L	1.23	$2.61 * 10^{44}$
S_O	$S_{V,(SD+H)}$	0.615	0.476	L	3.36	$1.91 * 10^{-11}$
L_O	$L_{V,(SD+H)}$	0.214	0.597	PL	$6.40 * 10^{-1}$	$7.23 * 10^{15}$
S_O	$S_{V,(SD+L)}$	0.500	0.322	L	$1.08 * 10^{-1}$	$1.84 * 10^{-12}$
L_O	$L_{V,(SD+L)}$	0.254	0.685	PL	$5.52 * 10^{-1}$	$2.48 * 10^{19}$
S_X	S_γ	0.518	0.043	L	3.49	$4.42 * 10^{-10}$
L_X	L_γ	0.118	0.577	PL	$6.93 * 10^{-1}$	$1.46 * 10^{15}$
S_X	$S_{V,H}$	0.827	0.732	L	$6.23 * 10^{-1}$	$2.21 * 10^{-12}$
L_X	$L_{V,H}$	0.472	0.655	PL	$5.07 * 10^{-1}$	$3.25 * 10^{22}$
S_X	$S_{V,L}$	0.869	0.714	L	$1.97 * 10^{-1}$	$8.75 * 10^{-13}$
L_X	$L_{V,L}$	0.795	0.730	L	$2.70 * 10^{-1}$	$3.49 * 10^{43}$
S_X	$S_{V,SD}$	0.099	0.033	L	$1.52 * 10^{-2}$	$7.46 * 10^{-13}$
L_X	$L_{V,SD}$	0.533	0.699	PL	$6.54 * 10^{-1}$	$4.69 * 10^{14}$
S_X	$S_{V,(SD+H)}$	0.802	0.340	L	1.42	$2.39 * 10^{-12}$
L_X	$L_{V,(SD+H)}$	0.135	0.447	PL	$5.22 * 10^{-1}$	$1.51 * 10^{21}$
S_X	$S_{V,(SD+L)}$	0.827	0.438	L	$0.59 * 10^{-1}$	$6.93 * 10^{-12}$
L_X	$L_{V,(SD+L)}$	0.548	0.685	PL	$6.13 * 10^{-1}$	$4.54 * 10^{16}$
S_γ	$S_{V,H}$	0.564	0.079	L	$4.28 * 10^{-3}$	$1.32 * 10^{-12}$
L_γ	$L_{V,H}$	0.037	0.471	PL	$2.74 * 10^{-1}$	$2.81 * 10^{32}$
S_γ	$S_{V,L}$	0.552	0.341	L	$6.72 * 10^{-3}$	$-9.22 * 10^{-13}$
L_γ	$L_{V,L}$	0.816	0.883	PL	$5.59 * 10^{-1}$	$1.78 * 10^{8}$
S_γ	$S_{V,SD}$	0.502	0.622	PL	$6.62 * 10^{-1}$	$6.98 * 10^{-6}$
L_γ	$L_{V,SD}$	0.701	0.885	PL	$8.32 * 10^{-1}$	$7.57 * 10^{5}$
S_γ	$S_{V,(SD+H)}$	0.625	0.591	L	$1.59 * 10^{-1}$	$2.67 * 10^{-11}$
L_γ	$L_{V,(SD+H)}$	0.177	0.698	PL	$6.73 * 10^{-1}$	$3.03 * 10^{13}$
S_γ	$S_{V,(SD+L)}$	0.606	0.545	L	$6.24 * 10^{-3}$	$1.72 * 10^{-12}$
L_γ	$L_{V,(SD+L)}$	0.282	0.861	PL	$6.28 * 10^{-1}$	$1.29 * 10^{15}$
Γ_X	Γ_γ	0.175	0.196	PL	0.135	1.61
Γ_X	$\Gamma_{V,(SD+H)}$	0.368	0.376	PL	0.395	2.37
Γ_γ	$\Gamma_{V,(SD+H)}$	-0.067	-0.063	L	-0.21	3.66

5.2 Cross bands flux energy density and luminosity study

Cross band flux energy density and luminosity study divided into three sections considering strength of the flux energy density correlation.

Figure 14 shows distributions of PCC values for all the flux energy density and luminosity correlations. Six pairs of cross band flux energy density datasets do not have correlations. Flux energy densities of the BL Lacs are depending on their distance. I subtract distance bias by using the luminosities instead of the flux energy densities. Subtracting distance bias gives a better PCC value in most of the cases.

Only for seven cross band correlations PCC decrease after taking out this bias. PCCs for three cross bands pairs decrease more than 0.1. Finally, this decreasing PCC cause to correlation change from strong to intermediate only on two pairs (i.e. X-(V,H) and X-(V,H+SD)).

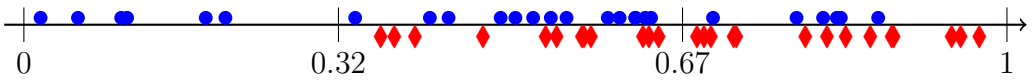

Figure 14. Distribution of PCC values for flux energy density (circles) and luminosity (diamonds) correlations

All pairs of luminosity datasets are correlated to each other with different factors. Seventy four percent of cross bands luminosity give better power law correlation than linear correlation. Seventy five percent of valid flux energy density correlations are linear correlations.

When considering luminosity correlations, the errors on redshift and parameters which affect luminosity distant should be taking into account in future analysis.

I categorize correlations according to the flux energy density correlations strength and discuss both flux energy density and luminosity results within these categories in next pages.

Presented correlation trend lines in table 13 are not statistically studied. Lack of data points' error bars is the main reason of this issue. The goodness of fitted

lines are not clear yet, but they still can be used as luminosity or flux energy density calculators between different bands.

Flux energy density strong correlations

Six pairs of data sets have strong correlations in flux energy densities.

Radio and optical band have strong correlations with γ-rays band. These findings are consistent with the works done by Fan et. al.[13] and Hovatta et.al. [82]. Luminosity correlations between these bands are better than their flux energy densities correlations. Improvement of correlation from flux energy density to luminosity are illustrated in panels (c and h) in figure 15 and panels (b and f) in figure 16.

X-rays has correlations with four datasets of VHE γ-rays band. Single detected VHE γ-rays dataset does not show any correlation with X-rays. Unlike R-γ and O-γ correlations, X-rays and VHE γ-rays correlations weaken when considering their luminosity correlations. Also, combining single detected data to high or low state in VHE γ-rays band causes the correlations weakening. This mean that increasing the number of data points do not help us for finding better correlations between these pair of datasets. Difference in physics behind different state could be assumed as reason for this issue. For X-(V,L) and X-(V,L+SD) luminosity correlations are still strong while for X-(V,H) and X-(V,H+SD) luminosity correlations become intermediate. It can be concluded that X-rays has better correlation with the low state of VHE γ-ray than the high state.

The connection between luminosities in these bands have been studied in Wagner [3] and he finds visible trend between X-rays and VHE γ-rays luminosities. For flux energy densities single sources are known to show connection in variability and in their light curves during the flare times (1ES 2344+514 and Markarian 180 [83]). But there are some cases which disagree with this connection (e.g. VHE γ-rays orphan flare of Markarian 501 in 2009 [84]). Panels (b, c, e and f) in figure 17 show

the schematic of these correlations.

Flux energy density intermediate correlations

Fourteen pairs of datasets have intermediate flux energy density correlations.

Optical band flux energy density show intermediate power law correlation to radio band, while their luminosity show strong linear correlation (See panels (a and f) in figure 15). If we assume linear model optical band flux energy density has no correlation to radio band. Meanwhile assuming power law model correlation increases PCC value between two bands by a factor of ~ 2.4 (see the first row of table 13). These two band have intermediate power law correlation. This was expected as the radiation mechanism in these two bands are the same[25].

Two VHE γ-rays datasets, which show intermediate correlations to radio band, are V,(H+SD) and V,(L+SD). As the first outcome, it can be concluded that number of data points for finding correlations with homogeneous datasets are low. The value of PCC increases more when high state dataset combined to single detected dataset. $S_{V,(H+SD)}$ show more correlation than $S_{V,(L+SD)}$. These datasets show more correlation in luminosity. Meanwhile, $L_{V,(L+SD)}$ is more correlated to radio band than $L_{V,(H+SD)}$. It shows VHE γ-rays high state dataset is more statistically independent from distance. The effect of received flux on luminosity is huge and somehow nearly equal to luminosity distance effect. This cause the $L_{V,(H+SD)}$ plot be become more scattered. The main reason for flux effect could be jet power in high state which agrees with Wagner [3] conclusions.

Optical and X-rays flux energy densities have intermediate linear correlation. In comparison to the other intermediate correlation on this property this correlation is within the weak ones (PCC=0.413). Their luminosity has even weaker correlation than flux energy density. The luminosity correlation can be described by power law

[25]Spectrum of synchrotron mechanism can be described by power law model.

model. As shown in figure 16 (Panel (a)), boundaries of our pair of dataset are similar to the boundaries which are introduced by Costamante and Ghisellini [11] for selecting TeV BL Lacs candidates.

Four out of five datasets of VHE γ-rays band show flux energy density intermediate correlation to optical band. The dataset which does not show such correlation is $S_{(V,SD)}$. Datasets which contains the high state of multiple detected sources are less correlated in luminosity than flux energy density (panels c and g in figure 16). But the ones which contains low state have good improvement when I try to find luminosity correlation for them. Flux energy density correlation of high and low states to optical improve when I add single detected data points to these datasets. But this behaviour does not exist in luminosity correlation. For high state the luminosity correlation coefficient improves, while for the low state it drops 18%. It shows that single detected sources have similar behaviour to the high state of multiple detected sources in $L_O - L_V$ plane.

X-rays and γ-rays show intermediate correlation both in flux energy density and luminosity planes. Correlation coefficient is a little better in luminosity plane than in flux energy density plane. Flux energy densities have linear correlation, but luminosities have power law correlation.

Finally, γ-rays band flux energy density have intermediate correlation with all five datasets of VHE γ-rays band. The correlations turn to strong correlation when considering luminosity datasets except for one dataset (i.e. (V,H)). Figure 18 show distribution of sample for these correlations. Combination of single detected source to high and low state of multiple detected source improve flux energy density correlation, but weakens luminosity correlations to γ-rays band. Connection between these to bands is expected as their radiation mechanism are the same and they are close to each other in energy range. Taking into the account that VHE γ-rays data points are not corrected for the EBL absorption, weaker correlation in flux energy

density planes are also expected.

Flux energy density no correlations

As the best done work up to now, Costamante and Ghisellini [11] had no chance to attempt for finding correlation between S_R and S_X, because number of TeV BL Lacs was too low (five) in that time. We find that there is no correlation between S_R and S_X datasets. As it is shown in figure 15, our finding about the place of TeV BL Lacs in $S_R - S_X$ plane confirms their finding in 2002. The chosen rectangular by them is still valid for TeV BL Lacs. This can be a good criteria for predicting TeV BL Lacs. No correlation between S_R and S_X could be described by different emission regions of these two band. Luminosity correlation between these two band are intermediate but it is not so strong and the PCC is near to the introduced boundary.

Three out of five datasets of VHE γ-rays do not show flux energy density correlations to radio band. These datasets are not-combined ones (i.e. $S_{(V,H)}$, $S_{(V,L)}$ and $S_{(V,SD)}$). Lack of enough data points is the main cause of not finding correlation between these datasets and radio band. The correlations improve when the luminosity are considered for finding correlations. VHE γ-rays low state has strong correlation to radio band.

VHE γ-rays high state and single detected datasets have intermediate luminosity correlation. Meanwhile, single detected dataset is more correlated to radio. Wagner, R. M., 2008 [3] claimed that there is no clear trend between radio and VHE γ-rays. Our finding somehow disagree with his findings. Number of data points in the time of their publication can be a reason for this disagreement. Another reason is that they used data from Costamante and Ghisellini [11], which were old, incomplete and not well averaged, as their radio data points.

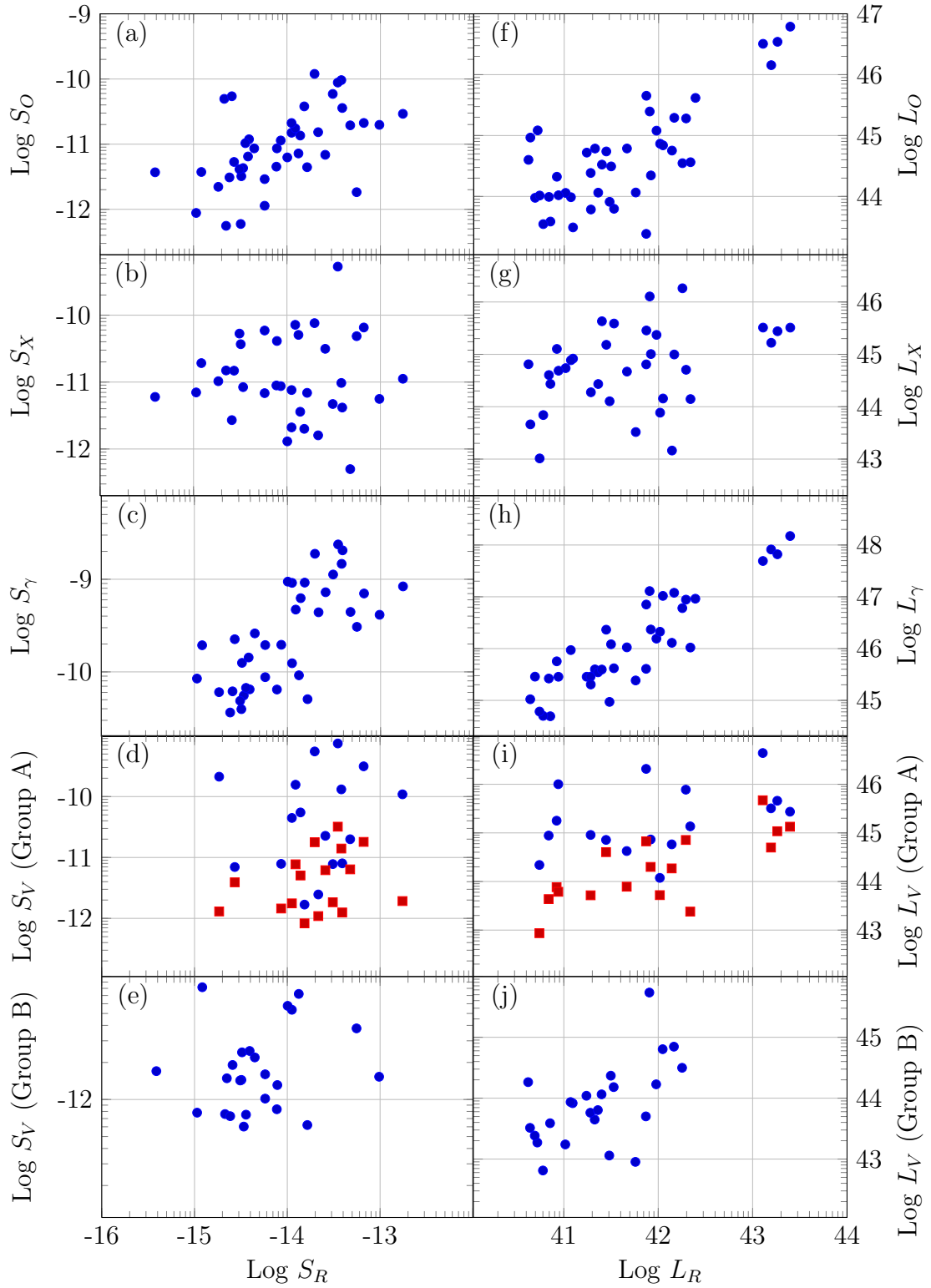

Figure 15. Left: Sample distribution in $S-S$ planes. X axis is S_R and Y axes from top to bottom are S_O, S_X, S_γ, S_V (*Group A*) and S_V (*Group B*) all in $[erg/cm^2/s]$ unit. Right: Sample distribution in $L-L$ planes. X axis is L_R and Y axes from top to bottom are L_O, L_X, L_γ, L_V (*Group A*) and L_V (*Group B*) all in $[erg/s]$ unit. Panels (d and i): High state (circles) and low state (rectangles).

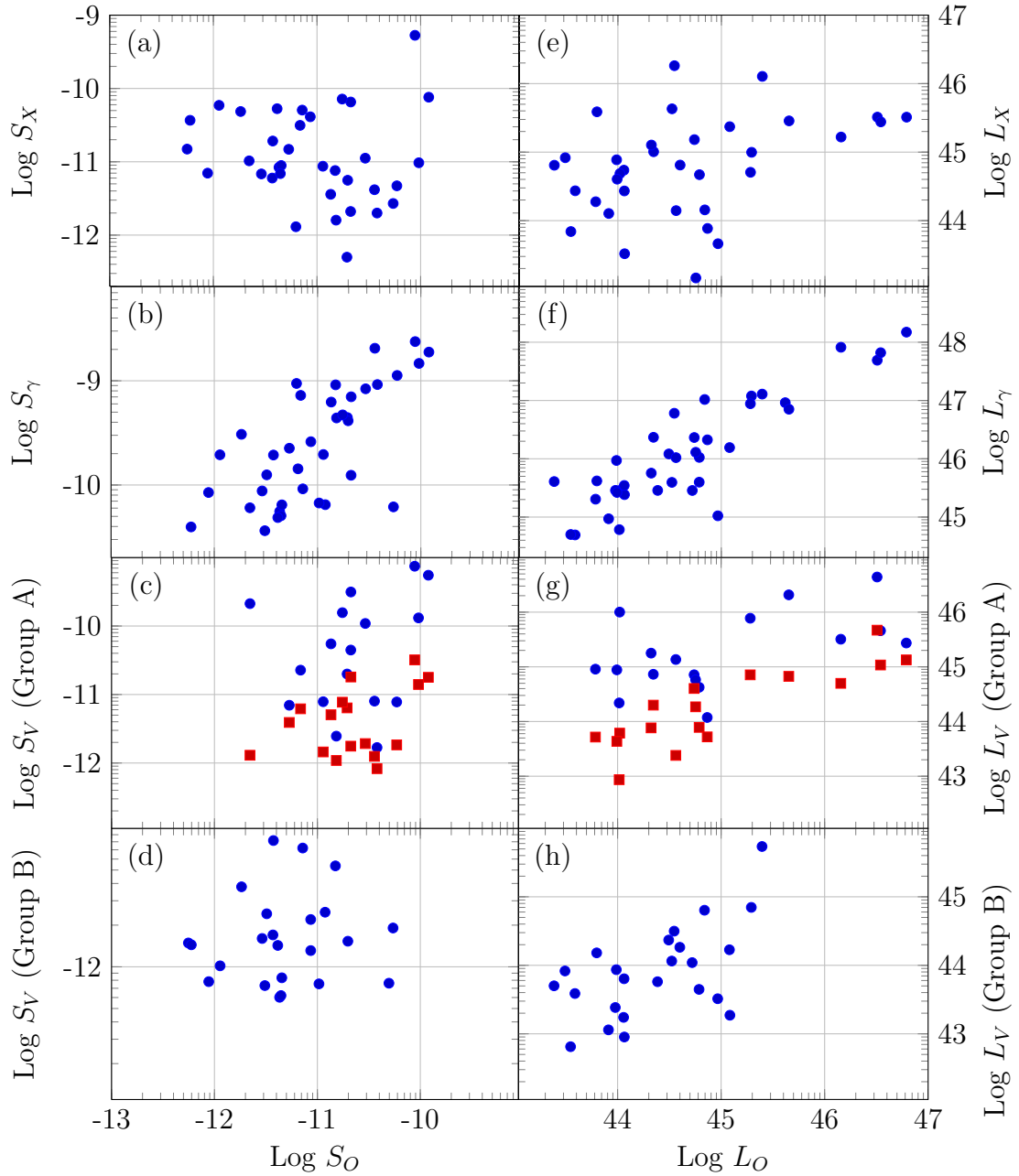

Figure 16. Left: Sample distribution in $S-S$ planes. X axis is S_O and Y axes from top to bottom are S_X, S_γ, S_V (*Group A*) and S_V (*Group B*) all in $[erg/cm^2/s]$ unit. Right: Sample distribution in $L-L$ planes. X axis is L_O and Y axes from top to bottom are L_X, L_γ, L_V (*Group A*) and L_V (*Group B*) all in $[erg/s]$ unit. Panels (c and g): High state (circles) and low state (rectangles).

VHE γ-rays single detected dataset does not show flux energy density correlation to optical and X-rays band. However, it shows strong luminosity correlation to these bands. These connections are the good ones which can be used to find new VHE

γ-rays emitting BL Lacs.

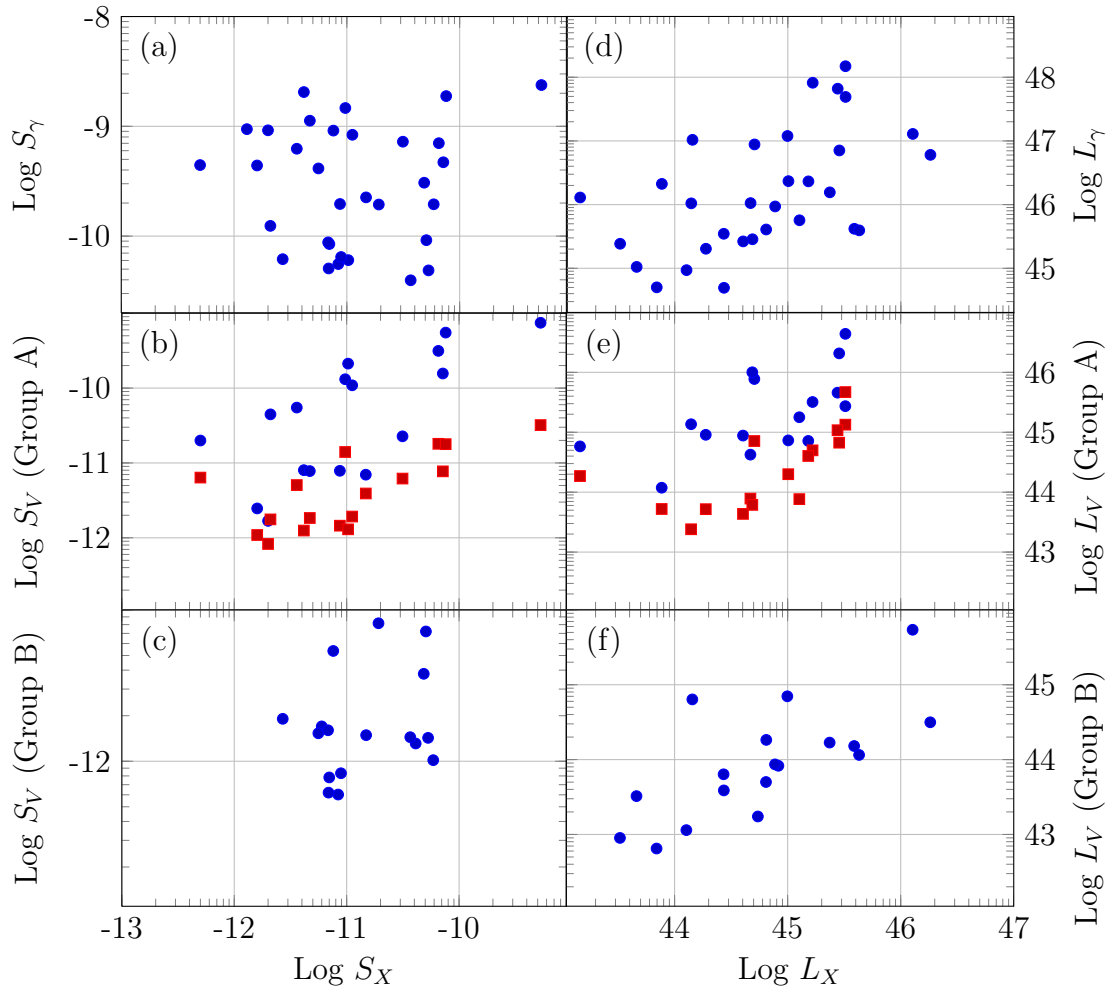

Figure 17. Left: Sample distribution in $S-S$ planes. X axis is S_X and Y axes from top to bottom are S_γ, S_V $(Group\ A)$ and S_V $(Group\ B)$ all in $[erg/cm^2/s]$ unit. Right: Sample distribution in $L-L$ planes. X axis is L_X and Y axes from top to bottom are L_γ, L_V $(Group\ A)$ and L_V $(Group\ B)$ all in $[erg/s]$ unit. Panels (b and e): High state (circles) and low state (rectangles).

When subtracting distance effect by comparing BL Lacs luminosities in different planes, the trends become more clear. This issue is completely obvious in panels h of figure 15, panel f of figures 15, 16, 17 and 18.

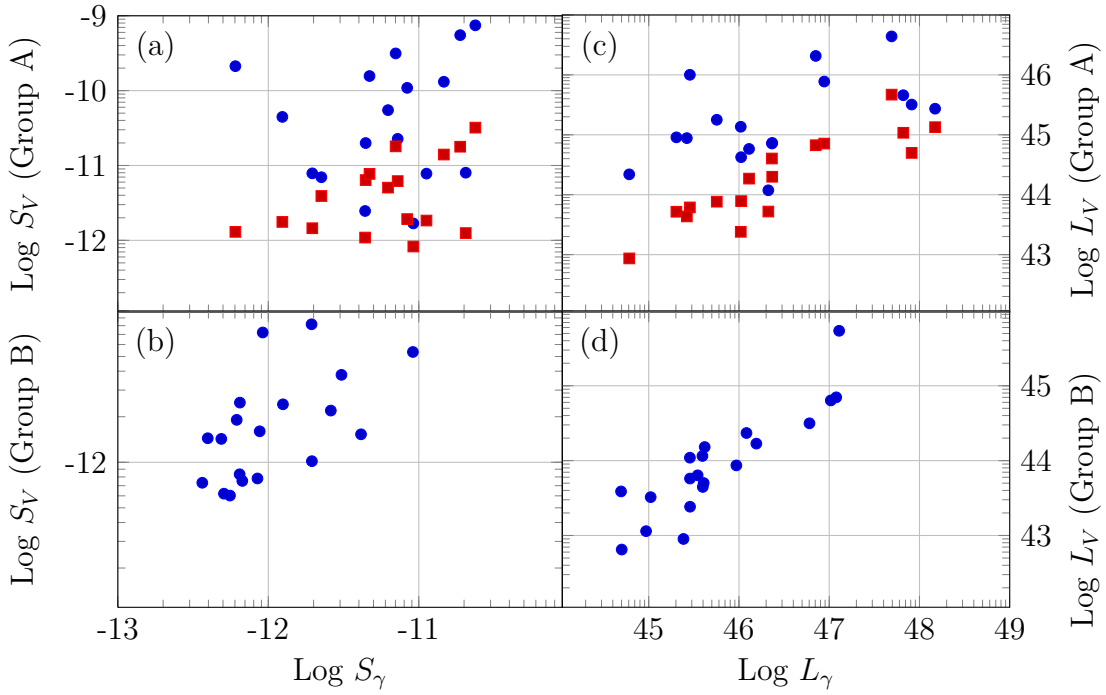

Figure 18. Left: Sample distribution in $S-S$ planes. X axis is S_γ and Y axes from top to bottom are S_V $(Group\ A)$ and S_V $(Group\ B)$ all in $[erg/cm^2/s]$ unit. Right: Sample distribution in $L-L$ planes. X axis is L_γ and Y axes from top to bottom are L_V $(Group\ A)$ and L_V $(Group\ B)$ all in $[erg/s]$ unit. Panels (a and c): High state (circles) and low state (rectangles).

5.3 Cross bands Spectral study

Distribution of sample in spectral indices planes are illustrated in figure 19. In this figure X-rays and γ-rays band spectral indices considered as independent parameter separately. While γ-rays and VHE γ-rays.

VHE γ-rays spectral indices used in this section as data points are combination of VHE γ-rays group A high state and group B. Low state spectral indices of group A are ignored due to being within the error bars of high state spectral index data points.

X-rays spectral index shows intermediate power law correlation to the VHE γ-rays spectral index. X-rays spectral index could be used as a probe to predicting VHE γ-rays. Massaro, F., et al. 2011 [67] used this property to predict some of the VHE γ-rays sources. After their prediction some of the introduced sources are

detected in this band. But it can not be proved that this prediction method is correct. According to my proposal for *MAGIC*-cycle 8, two of the sources which was predicted by him do not show any significant signal in VHE γ-rays band.

Unlike the work done by Abdo et. al. [12], γ-rays and X-rays do not have any correlation to each others. It means that their finding can not be used for TeV BL Lacs. Less number of TeV BL Lacs in their sample and the statistical effect of other non-TeV BL Lacs and AGNs could be the reasons for this discrepancy.

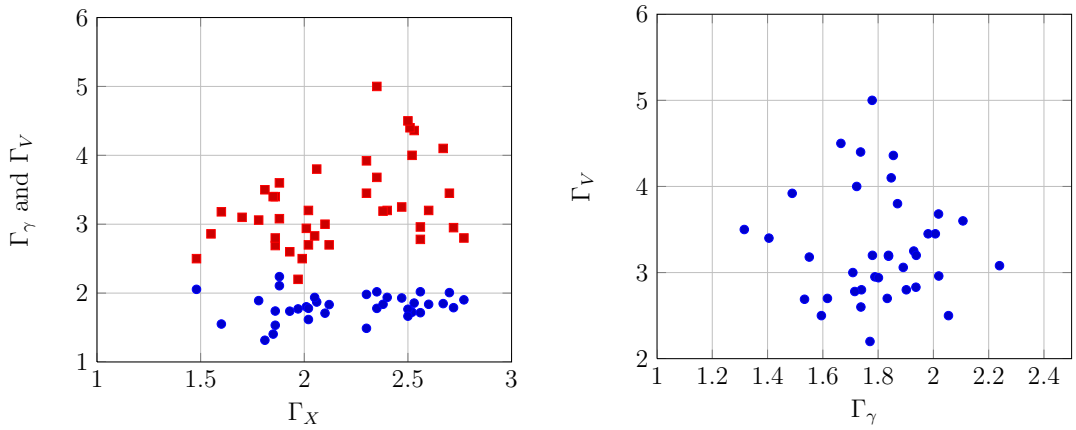

Figure 19. Left: BL Lacs' γ-rays (circles) and VHE γ-rays (squares) spectral index distribution considering X-rays spectral index as independent parameter. Right: BL Lacs' VHE γ-rays spectral index distribution considering γ-rays spectral index as independent parameter.

VHE γ-rays and γ-rays spectral indexes do not show correlation. Using measured Γ_V instead of the intrinsic can be a reason for not having correlation to Γ_γ. The soft spectra of VHE γ-rays happens when the γ-rays spectra is near 1.8. There is also a peak in γ-rays flux near this spectral index value[26]. It can be concluded that near this spectral index most of the energy of the jet is used to emit γ-rays and can not be extended to VHE γ-rays part of spectrum.

Spectral indices do not show linear or power law correlations to each other.

[26]Please see section 3.4.3

5.4 Summary and conclusions

Correlations of flux energy density and luminosity between different wavelengths ranges are studied using the synchronized collected data in chapters 3 and 4. Luminosity correlations describe connection between object's intrinsic properties. They can be used to develop current physical knowledge behind emission mechanism. Therefore, luminosity correlations are generally more interesting.

Fourteen pairs of datasets have strong luminosity correlation. The three most strongest correlations between pairs of luminosity datasets are $(L_R - L_\gamma)$, $(L_O - L_\gamma)$ and $(L_R - L_O)$. They have PCC value above 0.94. VHE γ-rays datasets are not within these three pairs. These correlations also have been found in Fan et. al. [13] and Hovatta et.al [82]. Hovatta et.al [82] concluded that BL Lacs' γ-rays emission is more related to the jet's particle flow than the shocks generated inside the jet.

Radio band luminosity is the proxy of jet power. Therefore, having strong correlation to optical shows that the emission of BL Lacs in the optical band is mostly dominated by the emission from their jets. Furthermore, for BL Lacs' γ-rays emission depend on the jet power. Taking into account $(L_O - L_\gamma)$ strong correlation, our results confirm conclusion made by Hovatta et.al [82].

Rest of the strong luminosity correlations are between one of VHE γ-rays datasets and other bands. γ-rays has strong luminosity correlation to four VHE γ-rays datasets. γ-rays and VHE γ-rays bands emission mechanism is thought to be the same and luminosity correlations are predictable.

Number of strong correlations to VHE γ-rays datasets for X-rays and optical is three. These two bands thought to be the origin of seed electron for IC mechanism, which describe VHE γ-rays emissions.

Finally, radio band has only one strong luminosity correlation to VHE γ-rays datasets. VHE γ-rays low state dataset is the one which has correlation to radio band.

Comparing datasets of VHE γ-rays, VHE γ-rays low state ($L_{V,L}$) is correlated to all other bands. It confirms that an emission mechanism exist which can describe the entire SED of BL Lacs. It is believed that SSC is such a mechanism.

VHE γ-rays single detected ($L_{V,SD}$) has strong correlations to optical, X-rays and γ-rays bands. $L_{V,SD}$ is a good probe to predict the amount VHE γ-rays radiation of non-TeV BL Lacs, if have well averaged optical, X-rays and γ-rays properties.

VHE γ-rays high state luminosity dataset ($L_{V,H}$) is the only dataset that does not show strong luminosity correlation to other bands. This dataset has better correlation in flux energy density than luminosity. Therefore, effect of distance is more dominant than the effect of variability amplitude within the distribution of this dataset.

VHE γ-rays single detected sources have similar behaviour to the low state of multiple detected ones. It can be concluded that VHE γ-rays high state has different emission or particle acceleration mechanism. This also confirmed by soft spectral indices in VHE γ-rays (Figure 19) near the peak of flux energy density in γ-rays band (Figure 9).

Finally, to complete the work of population study, followings steps should be done:

1. Statistical studies on the fitted models.

2. Collect the missing polarization data.

3. Finding correlations between polarization properties and other BL Lacs' properties, such as γ-rays and VHE γ-rays flux.

4. Producing a well averaged X-rays properties in $(2-10$ [keV]) band. This will implement by analysing *SWIFT-XRT* raw data provided in its observation database.

5. Completing the sample host galaxy flux to be insured about fully subtracting this bias from optical flux properties and performing a proper variability amplitude study.

6. Calculating VHE γ-rays intrinsic properties to subtract EBL absorption bias from them. *MAGIC* collaboration has a database of spectral points for all observed sources, which will be used to complete this task.

7. Taking into account the errors of radio and optical band properties in model fitting procedure. The error bars in optical will be calculated using Tuorla blazar monitoring database while for the radio literature will be searched deeply.

8. Collecting synchronized and quasi-simultaneous data for γ-rays, X-rays, optical and radio properties of non-TeV BL Lacs.

9. Comparing TeV BL Lacs properties to those of the non-TeV BL Lacs samples.

6 Future prospective and acknowledgements

6.1 Future prospective

In this work we have aimed at collecting synchronized data of TeV BL Lacs. As described in previous chapter, this database needs to be completed. Then it should be compared to non-TeV BL Lacs to investigate what makes BL Lac object a TeV BL Lac and to anticipate good candidates for future TeV detections.

Additionally, multi wavelengths analysis of BL Lacs aims at studying their intrinsic properties. As they are bright extragalactic objects, they can be used to study the universe between us and BL Lacs (e.g. Extragalactic Background Light (EBL) and Inter Galactic Magnetic Field (IGMF)). EBL is all the accumulated radiation of all stars and starlight reprocessed by the dust and contains star formation history of the universe. VHE γ-ray observations of BL Lacs can be used to constrain the level of EBL and strength of the magnetic field, but for this intrinsic VHE γ-ray spectrum has to be known. The more VHE γ-rays detected (TeV) BL Lacs, which are different in redshifts and positions, means the more accurate indirect EBL measurement.

In unified scheme of radio-loud AGNs, the observed nuclear phenomenology of BL Lacs is interpreted as being due to presence of relativistic jet. Multi wavelengths analysis of BL Lacs can be used to probe the relativistic jets. By studying the observed emission we can constrain particle acceleration mechanism, emission mechanism, gamma-rays production mechanism, magnetic field in jet, Doppler factors. These constraints can be compared to those resulting from magnetohydrodynamical simulations of the jets. However, currently the simulations typically scope mainly the jet launching region, while the main part of the BL Lacs emission originates further out in a jet. Still, within this work, It is good to compare the constraints from the simulations to constraints from observations.

BL Lacs multi wavelengths data can be modelled in first order with the simple

SSC model, to evaluate the parameters of the emission region.

Observing time with the best IACTs for source hunting in VHE γ-rays band is at least 10-15 hours because of relatively low photon flux of objects in this band. This forces astronomers to predict whether an object emits VHE γ-rays. According to current knowledge there is no concrete prediction method in this regard. The correlations which are studied in this thesis are the main building block introduce prediction methods. In addition, comparing multi wavelengths properties of TeV BL Lacs to the non-TeV BL Lacs (e.g. full sample of BL Lacs), which is not done in this work, also plays an important role in introducing a prediction method.

6.2 Acknowledgements

I would like to express my gratitude to my supervisor, Dr. Elina Lindfors, for her help, advice, understanding, patience and teaching me word by word from basics of astronomy through the advance part of my field of interest, and for motivating me in the time of changing my proficiency. I would also like to appreciate professor Harry Lehto for opening window of astronomy in my life.

I should express here my appreciation to all "Tuorlans", who taught me what astronomy is about. Special thanks to Riho Reinthal who shared his time, knowledge and many other things with me to start this thesis. Also I should thank to my best friend Mehrnoosh Nickpasand who encouraged me, accompanied me, and gave me words of comfort in the difficult times. Undoubtedly many names are missing here.

Last but not least, I would appreciate my brother to support me both financially and mentally in last two years. I could not achieve to this level without the supports of my wife and my parents. I dedicated this thesis to my love (Mahboobeh).

This thesis has made use of NASA's Astrophysics Data System and NASA/IPAC Extragalactic Database (NED) which is operated by the Jet Propulsion Laboratory, California Institute of Technology, under contract with the National Aeronautics

and Space Administration. This thesis has made use of data obtained from the High Energy Astrophysics Science Archive Research Center (HEASARC), provided by NASA's Goddard Space Flight Center.

References

[1] http://en.wikipedia.org/wiki/Active_galactic_nucleus

[2] Urry, C. M. and Padovani, P., 1995, Publications of the Astronomical Society of the Pacific, v.107, p.803

[3] Wagner, R.M., 2008, Monthly Notices of the Royal Astronomical Society, Volume 385, Issue 1, pp. 119-135.

[4] Aharonian, F., et al., 2008, Astronomy and Astrophysics manuscript no. hessj1825II

[5] Ginzburg, V. L. and Syrovatskii, S. I., 1964, The Origin of Cosmic Rays (New York: Macmillan)

[6] Aharonian, F., et al., 2008, Astronomy and Astrophysics, Volume 481, pp. 401-410

[7] Massaro, F., et al., 2013, The Astrophysical Journal Supplement Series, 207:4 (15pp)

[8] Abdo, A. A., et al., 2010, The Astrophysical Journal, 716:30-70

[9] Mariotti, M., 2010, The Astronomer's Telegram, #2753

[10] Bassani, L., et al., 2009, Monthly Notices of the Royal Astronomical Society: Letters, Volume 397, Issue 1, pp. L55-L59

[11] Costamante, L. and Ghisellini, G., 2002, Astronomy and Astrophysics, v.384, p.56-71 (2002)

[12] Abdo, A. A., et al., 2010, The Astrophysical Journal, Volume 716, Issue 1, pp. 30-70 (2010)

[13] Xu-Liang Fan, et al., 2012, Research in Astron. Astrophys., Vol. 12, No. 11, 1475-1485

[14] Massaro, E., et al., 2008, Astronomy and Astrophysics manuscript no. AA-2008-10161 Lc

[15] Pearson, K., 1895, Proceedings of the Royal Society of London, 58, pp. 240-242.

[16] Jones, D. H., et al., 2009, Monthly Notices of the Royal Astronomical Society, Volume 399, Issue 2, pp. 683-698

[17] Nieppola, E., et al., 2006, Astronomy and Astrophysics, Volume 445, Issue 2, January II 2006, pp.441-450

[18] Rector ,T.A., et al., 2003, The Astronomical Journal, Volume 125, Issue 3, pp. 1060-1072

[19] Mao, L. S., et al., 2011, New Astronomy, Volume 16, Issue 8, p. 503-529

[20] Laurent-Muehleisen, S.A, et al., 1998, The Astrophysical Journal Supplement Series, Volume 118, pp. 127-175

[21] Furniss, A., et. al. 2013, The Astrophysical Journal, Volume 761, 6pp

[22] Falomo, R. and Kotilainen, J.K. 1999, Astronomy and Astrophysics, v.352, p.85-102 (1999)

[23] Ackermann, M., et al., 2011, The Astrophysical Journal, Volume 743, Issue 2, article id. 171, 37 pp. (2011)

[24] Aharonian, F., et al., 2007, Astronomy and Astrophysics, Volume 473, Issue 3, October III 2007, pp.L25-L28

[25] Shaw, M.S., et al., 2013, The Astrophysical Journal, Volume 764, Issue 135, pp. 1-13

[26] Benbow, W., et al., 2011, eprint arXiv: 1110.0038

[27] Kotilainen, J. K., et al., 2011, Astronomy and Astrophysics, Volume 534, id.L2, 5 pp

[28] Furniss, A., et. al. 2013, The Astrophysical Journal Letters, Volume 768, Issue 2, article id. L31, 6 pp. (2013).

[29] Danforth, C. W., et al., 2010, The Astrophysical Journal, Volume 720, Issue 1, pp. 976-986

[30] Fossati, G., et al., 1998, Monthly Notices of the Royal Astronomical Society, Volume 299, Issue 2, pp. 433-448

[31] Giommi, P., et al., 2004, eprint arXiv: astro-ph/0411093

[32] Laurent-Muehleisen, S. A., et al., 1999, The Astrophysical Journal, Volume 525, Issue 1, pp. 127-143

[33] Perlman, E. S., et al., 1996, Astrophysical Journal Supplement v.104, p.251

[34] Wright, E.L. 2006, The Publications of the Astronomical Society of the Pacific, Volume 118, Issue 850, pp. 1711-1715

[35] Planck Collaboration: Ade, P.A.R., et al., 2013, Astronomy and Astrophysics manuscript no. draft p1011

[36] Kovalev, Y. Y., et al., 2009, ApJ, 696, L17

[37] Ghirlanda, G., et al., 2010, MNRAS, 407, 791

[38] Ghirlanda, G., et al., 2011, MNRAS, 413, 852

[39] Mahony, E., et al., 2010, ApJ, 718, 587

[40] Ackermann, M., et al., 2011, arXiv:1108.0501 (Radio-gamma connection)

[41] Griffith, M. R., et al., 1995, Astrophysical Journal Supplement Series (ISSN 0067-0049), vol. 97, no. 2, p. 347-453

[42] Gregory, P. C., et al., 1991, Astrophysical Journal Supplement Series (ISSN 0067-0049), vol. 75, April 1991, p. 1011-1291. NSERC-supported research

[43] Gregory, P. C., et al., 1994, Astrophysical Journal Supplement Series, vol. 90, no. 1, p. 173-177

[44] Reinthal, R., et al., 2012, Journal of Physics: Conference Series, Volume 355, Issue 1, id. 012013

[45] Reinthal, R., 2012,
`http://www.astro.utu.fi/EWASS2013/S12/EWASS_120713_Reinthal.pdf`

[46] Wylezalek, D., et al., 2010, Bachelor Thesis in Physics

[47] Jannuzi, B. T., et al., 1994, Astrophysical Journal, Part 1 (ISSN 0004-637X), vol. 428, no. 1, p. 130-142

[48] Data from Liverpool telescope, Private communication with Nilsson, K.

[49] Mead, A. R. G., et al., 1990, Astronomy and Astrophysics Supplement Series (ISSN 0365-0138), vol. 83, no. 1, April 1990, p. 183-204

[50] Angel, J. R. P., et al., 1980, Annual review of astronomy and astrophysics. Volume 18. (A81-20334 07-90) Palo Alto, Calif., Annual Reviews, Inc., 1980, p. 321-361

[51] Ikejiri, Y., et al., 2011, Publications of the Astronomical Society of Japan, Vol.63, No.3, pp.639–675

[52] Flesch, E., et al., 2004, Astronomy and Astrophysics, v.427, p.387-392

[53] Tuorla Blazar monitoring Program, `http://users.utu.fi/kani/1m/index.html`

[54] Aleksic, J., et al., 2012, Astroparticle Physics, Volume 35, Issue 7, p. 435-448

[55] Aharonian, F., et al., 2008, Astronomy and Astrophysics, Volume 481, Issue 3, 2008, pp.L103-L107

[56] Jennifer K., et al., 2007, The Astrophysical Journal Supplement Series, 172:634-644

[57] Abramowski, A., et al., Astronomy and Astrophysics, Volume 516, id.A56

[58] Stroh, M.C. and Falcone, A.D. 2013, The Astrophysical Journal Supplement, Volume 207, Issue 2, article id. 28, 12 pp.

[59] Donato, D., et al., 2005, Astronomy and Astrophysics, Volume 433, Issue 3, April III 2005, pp.1163-1169

[60] Archambault, S., et al., 2013, The Astrophysical Journal, Volume 776, Issue 2, article id. 69, 10 pp.

[61] Giommi,P., et al., 2012, Astronomy and Astrophysics, Volume 541, 59 pp

[62] Stamerra, A., et al., 2011, The Astronomer's Telegram, #3208

[63] Aleksic, J., et al., 2013, Astronomy and Astrophysics, Volume 563, id.A90, 6 pp.

[64] Verrecchia, F., et al., 2007, Astronomy and Astrophysics, Volume 472, Issue 2, 2007, pp.705-713

[65] Aleksic, J., et al., 2012, Astronomy and Astrophysics, Volume 539, id.A118, 6 pp

[66] Massaro, F., et al., 2011, The Astrophysical Journal Letters, Volume 742, Issue 2, article id. L32, 5 pp. (2011)

[67] Massaro, F., et al., 2011, The Astrophysical Journal, Volume 793, Issue 73, pp. 1-12

[68] Aliu, E., et al., 2011, The Astrophysical Journal, Volume 742, Issue 2, article id. 127, 7 pp.

[69] Acciari, V. A., et al., 2010, The Astrophysical Journal Letters, Volume 715, Issue 1, pp. L49-L55 (2010)

[70] Hofmann, W., 2012, The Astronomer's Telegram, #4098

[71] Massaro, F., et al., 2008, Astronomy and Astrophysics, Volume 478, Issue 2, February I 2008, pp.395-401

[72] Ackermann, M., et al., 2013, arXiv:1306.6772v3

[73] Nolan, P. L., et al., 2012, The Astrophysical Journal Supplement, Volume 199, Issue 2, article id. 31, 46 pp. (2012)

[74] Abdo, A. A., et al., 2010, ApJS, 188, 405

[75] Senturk, G.D., et al., 2013, The Astrophysical Journal, Volume 764, Issue 2, article id. 119, 18 pp.

[76] Delotto, B. 2012, Journal of Physics: Conference Series 375

[77] Abdo, A. A., et al., 2009, The Astrophysical Journal Supplement, Volume 183, Issue 1, pp. 46-66

[78] Saxton, R.D., et al., 2008, Astronomy and Astrophysics, Volume 480, pp. 611-622

[79] Condon, J.J., et al., 1998, The Astronomical Journal, Volume 115, Issue 5, pp. 1693-1716.

[80] MAGIC Collaboration, 2014, Private communication with Lindfors, E.

[81] Aleksic, J., et al., 2012, Astroparticle Physics, Volume 35, Issue 7, p. 435-448

[82] Hovatta, T., et al, 2014, Monthly Notices of the Royal Astronomical Society, Volume 439, Issue 1, p.690-702

[83] Rugamer, S., et al., 2011, eprint arXiv:1109.6808

[84] Barres de Almeida, U., et al., 2011, Proceedings of the 32nd International Cosmic Ray Conference (ICRC2011), held 11-18 August, 2011 in Beijing, China. Vol. 8 OG2.3-2.4: Cosmic Ray Origin and GalacticP

[85] Abdo, A. A., et al., 2011, The Astrophysical Journal, Volume 726, Issue 1, article id. 43, 14 pp

[86] Swordy, S., et al., 2008, The Astronomer's Telegram, #1753

[87] Anderhub, H., et al., 2009, The Astrophysical Journal, Volume 704, Issue 2, pp. L129-L133

[88] Berger, K., et al., 2013, eprint arXiv:1308.3486

[89] Mirzoyan, R., 2014, The Astronomer's Telegram, #5887 and Lindfors ,E., 2014, Private communication

[90] Albert, J., et al., 2007, The Astrophysical Journal, Volume 667, Issue 1, pp. L21-L24

[91] Cortina, J. and Holder, J., 2014, The Astronomer's Telegram, #4976

[92] Lindfors ,E., 2014, Private communication

[93] Albert, J., et al., 2007, The Astrophysical Journal, Volume 663, pp. 125-138

[94] Aleksic, J., et al., 2012, Astronomy and Astrophysics, Volume 544, id.A142, 10 pp

[95] Albert, J., et al., 2006, The Astrophysical Journal, Volume 642, Issue 2, pp. L119-L122

[96] Acciari, V. A., et al., 2010, The Astrophysical Journal Letters, Volume 709, Issue 2, pp. L163-L167 (2010)

[97] Acciari, V. A., et al., 2009, The Astrophysical Journal, Volume 707, Issue 1, pp. 612-620 (2009)

[98] Acciari, V. A., et al., 2008, The Astrophysical Journal, Volume 684, Issue 2, pp. L73-L77

[99] Aleksic, J., et al., 2014, Astronomy and Astrophysics, Volume 567, id.A135, 15 pp.

[100] Petry, D., et al., 2002, The Astrophysical Journal, Volume 580, Issue 1, pp. 104-109

[101] Horan, D., et al., 2002, The Astrophysical Journal, Volume 571, Issue 2, pp. 753-762

[102] Orr, M. 2011, Proceedings of the 32nd International Cosmic Ray Conference (ICRC2011), held 11-18 August, 2011 in Beijing, China. Vol. 8 OG2.3-2.4: Cosmic Ray Origin and GalacticPhenomena, p.119

[103] Aleksic, J., et al., 2012, The Astrophysical Journal, Volume 748, Issue 1, article id. 46, 10 pp. (2012)

[104] Aharonian, F., et al., 1999, Astronomy and Astrophysics, v.342, p.69-86 (1999)

[105] Acciari, V. A., et al., 2011, The Astrophysical Journal, Volume 729, Issue 2, pp. 1-9

[106] Krawczynski, H., et al., 2004, The Astrophysical Journal, Volume 601, Issue 1, pp. 151-164

[107] Tagliaferri, G., et al., 2008, The Astrophysical Journal, Volume 679, pp. 1029-1039

[108] Aharonian, F., et al., 2007, The Astrophysical Journal, Volume 664, Issue 2, pp. L71-L74

[109] Aharonian, F., et al., 2009, The Astrophysical Journal Letters, Volume 696, Issue 2, pp. L150-L155 (2009)

[110] Arlen, T., et al., 2013, The Astrophysical Journal, Volume 762, 13pp

[111] Albert, J., et al., 2007, The Astrophysical Journal, Volume 666, Issue 1, pp. L17-L20

[112] Acciari, V. A., et al., 2011, The Astrophysical Journal, Volume 738, article id. 169, 8 pp. (2011)

[113] Aleksic, J., et al., 2014, arXiv:1211.2608v2

[114] Abramowski, A., et al., 2013, Astronomy and Astrophycisc, Volume 554, pp. A72

[115] Aleksic, J., et al., 2013, Astronomy and Astrophysics manuscript no. AA 0033 v5

[116] Aharonian, F., et al., 2007, Astronomy and Astrophysics, Volume 475, Issue 2, November IV 2007, pp.L9-L13

[117] Aliu, E., et al., 2012, The Astrophysical Journal, Volume 750, Issue 2, article id. 94, 6 pp

[118] Abramowski, A., et al., 2012, Astronomy and Astrophysics, Volume 538, id.A103, 9 pp

[119] Zech, A., et al., 2011, eprint arXiv:1105.0840

[120] Benbow, W., et al., 2011, eprint arXiv:1110.0040

[121] Aharonian, F., et al., 2010, Astronomy and Astrophysics, Volume 521, id.A69, 6 pp

[122] Abramowski, A., et al., 2012, Astronomy and Astrophysics, Volume 542, id.A94, 10 pp

[123] Aharonian, F., et al., 2007, Astronomy and Astrophysics, Volume 470, Issue 2, August I 2007, pp.475-489

[124] Albert, J., et al., 2006, The Astrophysical Journal, Volume 648, Issue 2, pp. L105-L108

[125] Hofmann, W., 2012, The Astronomer's Telegram, #4072

[126] Fortin, P., et al., 2010, 25th Texas Symposium on Relativistic Astrophysics

[127] Berger, K., et al., 2011, Proceedings of the 32nd International Cosmic Ray Conference (ICRC2011), held 11-18 August, 2011 in Beijing, China. Vol. 8 OG2.3-2.4: Cosmic Ray Origin and GalacticPhenomena, p.167

[128] Acero, F., et al., 2010, Astronomy and Astrophysics, Volume 511, id.A52, 13 pp

Appendix I: VHE γ-rays properties raw data

We present raw data of BL Lacs' VHE γ-rays properties in this appendix. The raw data are presented in two tables according to the groups which are defined in section 3.5.

We try to collect integral flux of sources in [Photon/cm^2/s] unit as much as possible. But for some of the observations integral flux in this unit are not available. In this case, I used integral flux of objects which are presented relative to the Crab nebula (VHE γ-rays standard candle) integral flux. These data are mostly the new ones which are according to preliminary data reduction results. VER J0521+211, 1ES 0806+524, Markarian 421 and 1ES 1959+650 in high state of group A are such sources. Meanwhile, 1ES 0502+675, RGB 0648+152, 1ES 1440+122, PKS 1440-389, AP Lib and 1ES 1741+196 are in group B.

Crab flux measured by different telescopes sometimes do not show good agreement to each other. This uncertainties are the result of different resolution, observing Zenith Angle, spectrum model fitting, extrapolation to a certain energy band.

I avoid these uncertainties by using Crab nebula flux from *MAGIC collaboration* [54] to change relative Crab unit to [Photon/cm^2/s] unit. The uncertainty about the real value which are reported by other telescopes are still present in my data. In comparison to other errors this error is negligible (Only for 7 data points).

Table A-1 shows the VHE γ-rays properties collected from different references for group A. Table A-2 shows the VHE γ-rays properties collected from different references for group B. In both tables integral flux is over E_t and the data are not comparable to each others. The synchronized comparable integral flux over 200 [GeV] are presented in Tables 9 and 10 in section 3.5

Table A-1: collected VHE γ-rays properties (group A)

Source Name	**High State**				**Low state**			
	E_t [**GeV**]	$f_{V,H(>E_t)}/10^{-12}$ $[Ph/cm^2/s]$	$\Gamma_{V,H}$	**Ref.**	E_t [**GeV**]	$f_{V,L(>E_t)}/10^{-12}$ $[Ph/cm^2/s]$	$\Gamma_{V,L}$	**Ref.**
(1)	**(2)**	**(3)**	**(4)**	**(5)**	**(6)**	**(7)**	**(8)**	**(9)**
3C 66A	200	25.00±4.00	4.10±0.60	[85]	200	3.90±1.60	4.10±0.40	[86]
VER J0521+211	200	70.77±14.70	3.25±0.72	[60]	200	19.30±1.30	2.92±0.34	[60]
S5 0716+714	400	7.50±2.20	3.45±0.54	[87]	400	0.80±0.70	3.45±0.54	[87]
1ES 0806+524	250	15.00±3.00	3.20±0.30	[88]	250	3.10±1.00	2.70±0.40	[88]
1ES 1011+496	200	77.00±2.00	3.01	[89]	200	15.80±3.20	4.00±0.50	[90]
Markarian 421	300	1430.22	2.20	[91, 92]	200	100.00	2.20±0.80	[93]
1ES 1215+303	200	7.70±0.90	2.96±0.14	[94]	200	3.40±0.10		[94]
1ES 1218+304	100	87.00±14.00	3.00±0.40	[95]	200	12.20±2.60	3.07±0.09	[96]
W Comae	200	62.20±12.00	3.68±0.22	[97]	200	19.90±0.70	3.81±0.35	[98]
PKS 1424+240	150	16.60±5.00	5.00±1.70	[99]	150	5.30±2.50	3.50±1.20	[99]
H 1426+428	500	67.00±11.39	3.50±0.35	[100, 101]	350	1.00	3.50±0.35	[100, 101]
PG 1553+113	200	24.30±1.40	4.50±0.21	[102]	150	14.00±3.80	4.10±0.30	[103]
Markarian 501	1000	178.07±10.12	2.06±0.13	[104]	300	28.00±5.00	2.72±0.15	[105]
1ES 1959+650	2000	7.23	2.83±0.14	[106]	300	12.70±1.60	2.58±0.18	[107]
PKS 2155-304	200	1720.00±50.00	3.19±0.02	[108]	200	55.60±1.30	3.34±0.05	[109]
BL Lacertae	200	340.00±60.00	3.60±0.40	[110]	200	6.00±2.00	3.60±0.50	[111]
1ES 2344+514	300	67.60±6.20	2.78±0.09	[112]	200	5.50±1.70	2.40±0.40	[113]

Table A-2: Collected VHE γ-rays properties (group B)

Source Name (1)	E_t [**GeV**] (2)	$f_{V(>E_t)}/10^{-12}$ $[Ph/cm^2/s]$ (3)	$\Gamma_{V,SD}$ (4)	**Ref.** (5)
BZB J0013-1854	310	0.83±0.17	3.40±0.50	[114]
1ES 0033+595	150	7.10±1.30	3.80±0.70	[115]
RGB J0152+017	300	2.70±0.51	2.95±0.36	[55]
1ES 0229+200	580	0.94±0.15	2.50±0.19	[116]
RBS 0413	250	1.50±0.60	3.18±0.68	[117]
1ES 0347-121	250	3.32±0.44	3.10±0.23	[24]
1ES 0414+009	200	1.88±0.20	3.45±0.25	[118]
PKS 0447-439	250	7.90±1.90	4.36±0.49	[119]
1ES 0502+675	300	7.80	3.92±0.35	[120]
PKS 0548-322	250	2.70±0.60	2.86±0.34	[121]
RGB 0648+152	200	7.54	4.40±0.80	[68]
RGB J0710+591	300	3.90±0.80	2.69±0.26	[69]
BZB J1010-3119	200	2.35±0.64	3.08±0.42	[122]
1ES 1101-232	200	4.50±1.20	1.51±0.17	[123]
Markarian 180	200	22.5±6.90	2.80±0.70	[124]
1ES 1440+122	200	2.28	3.40±0.70	[120]
PKS 1440-389	200	6.85		[125]
AP Lib	300	2.60	2.50±0.20	[126]
1ES 1727+502	200	2.60±0.80	2.70±0.50	[63]
1ES 1741+196	250	1.32	2.70±0.47	[127]
PKS 2005-489	400	2.57±0.18	3.20±0.16	[128]
B3 2247+381	200	5.00±0.60	3.20±0.50	[65]
H 2356-309	240	3.06±0.26	3.06±0.15	[57]

Appendix II: X-rays data reduction procedure

X-rays data reduction procedure used different files which are listed in table A-3 with their extension and description. The applications which are used in the procedure are introduced briefly in table A-4.

Table A-3: Description of files used in data reduction procedure

No.	File Type	File extension	Description
1	Level 2 Events File	-xpcw3po_cl.evt	Calibrated & screened event. Available in database.
2	Attitude File	-sat.fits	Used to to transform detector coordinates in sky position.
3	Housekeeping File	-xhd.hk	Includes columns for each of the parameters found in the header of the science packet.
4	Response Matrix File	-.rmf	This file prepared for a standard events grade setting.
5	Exposure Map Image	-xpcw3po_ex.img	This file is used to correct the loss of flux caused by some of the CCD pixels not being used to collect data.
6	Region file	-.reg	Shows which region of image is the region of interest to extract data from it.
7	Spectra file	-.pi	The file used to store events according to the energy channels.
8	Ancillary Response file	-.arf	Contains the effective area of the telescope as a function of energy needed to perform spectral analysis.

It is assumed that the user already install and initialize HEAsoft. HEAsoft has been linked to the *SWIFT-XRT* calibration database (CALDB)[27]. In the next step

[27]Please see `http://heasarc.gsfc.nasa.gov/docs/heasarc/caldb/swift/`

the observation data including auxiliary and housekeeping files should be downloaded from *SWIFTXRLOG* database[28]. After being prepared for data reduction the following procedure could be used to extract spectrum and calculating needed parameters. Level 2 Events File used as the event file in this procedure.

Table A-4: Description of applications used in data reduction procedure

No.	Application Name	Description
1	XSELECT	A command line interface to the Ftools. Used to extract images, light curves and spectra from the event data, using the entered filters, as well as the GTI created by the applied selection
2	XRTEXPOMAP	Generates an exposure map that accounts for CCD bad pixels and columns, attitude variations and telescope vignetting
3	XRTMKARF	Generates OGIP-style Ancillary Response Function (ARF) file which is suitable for input into the spectral fitting program XSPEC
4	GRPPHA	An interactive command driven task to define and display the grouping and quality flags, and the fractional systematic errors associated with channels in a FITS PI file.
5	XSPEC	A command-driven, interactive, X-ray spectral-fitting program.
6	DS9	An astronomical imaging and data visualization application.

The procedure schematic is illustrated as a flowchart diagram in figure A-1. Each application of HEAsoft has specific color in this diagram . Small circles, containing numbers, are the connection points accordingly. Downloading steps are illustrated as orange boxes.

[28] `http://heasarc.gsfc.nasa.gov/W3Browse/swift/swiftxrlog.html`

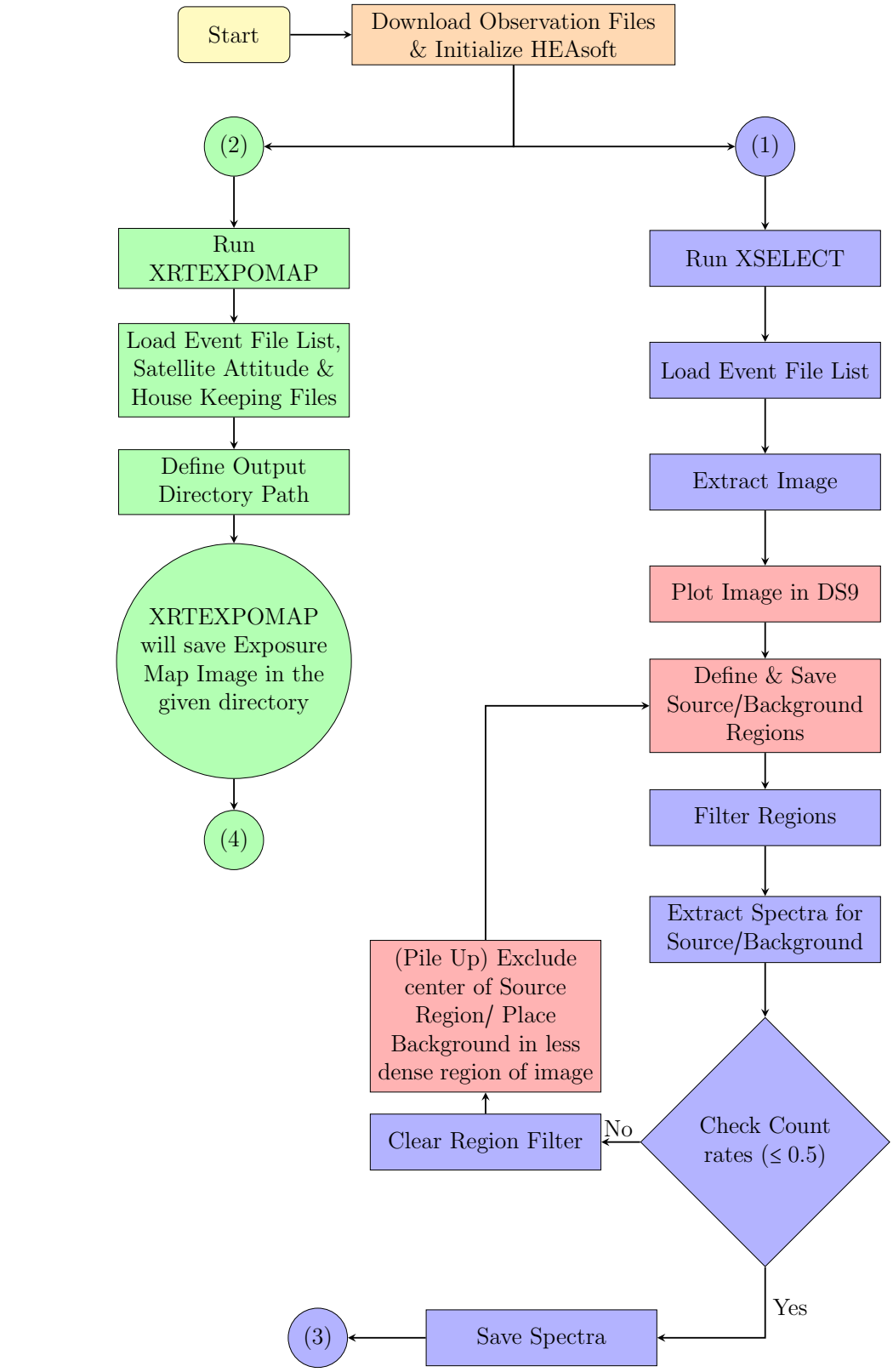

Figure A-1. Spectrum data reduction flowchart for SWIFT-XRT photon counting observations (Continued on next page)

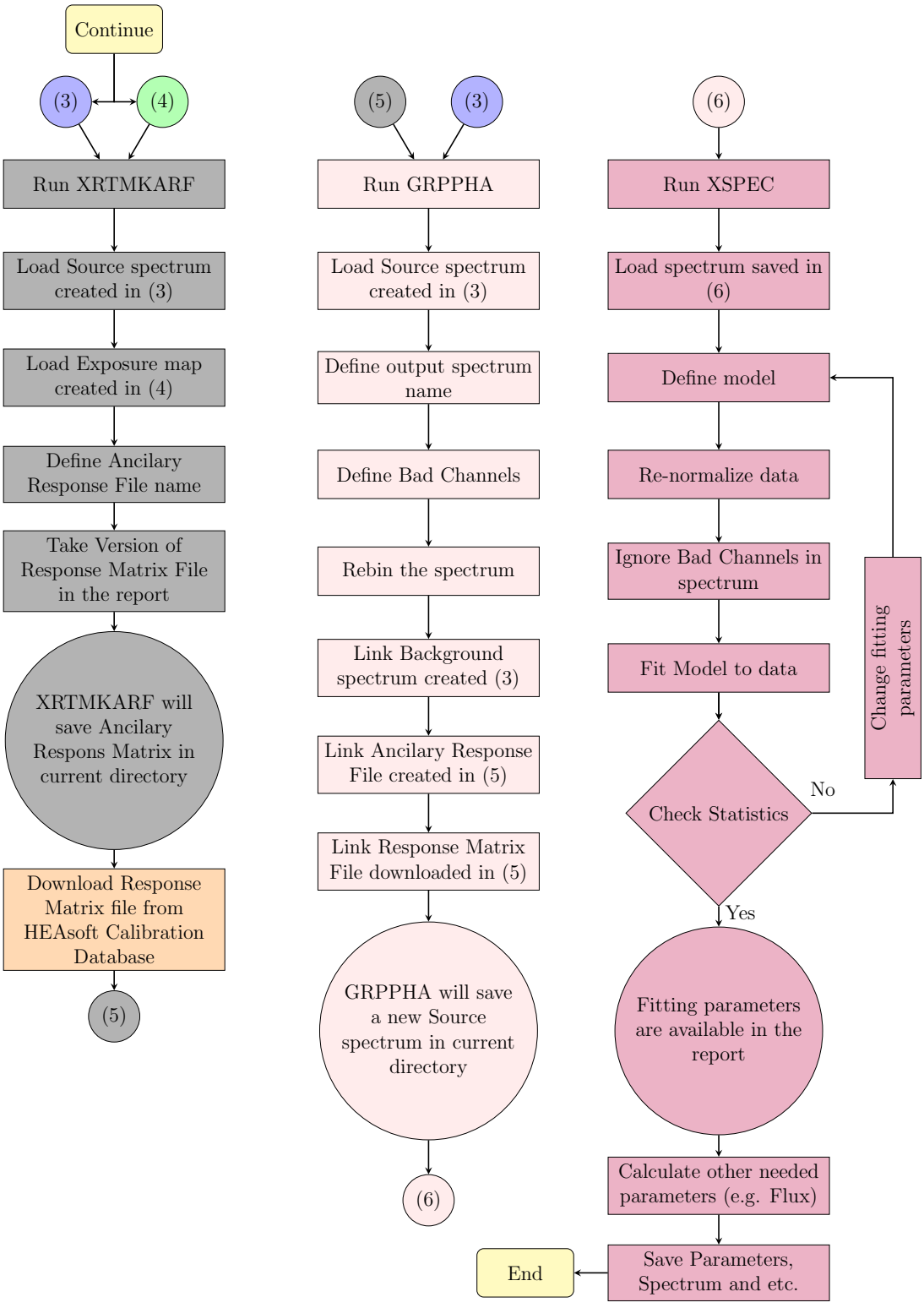

Figure A-1. (Continued from previous page) Spectrum data reduction flowchart for SWIFT-XRT photon counting observations

Data reduction procedure:

1. Run XSELECT by executing "xselect" command in terminal.
2. Load event file list, downloaded from database, by executing "read event" command and answering to the coming questions one by one (i.e. Directory path, Event file name and resetting mission)
3. Execute "extract image" command.
4. execute "plot image" command to see the visual image in DS9.
5. In DS9 define and save source and background regions.
6. Execute "filter region" command, using one of the generated region files in previous step.
7. Execute "extract spectrum" command.
8. Check spectrum count rate to be ≤ 0.5 count/s in report of "extract spectrum" command. Proceed to step 10.
9. (Pile Up) If the spectrum count rate is above 0.5 count/s, execute "clear region", redefine the region by excluding the center of source (For background region change the place of defined region) in DS9. Go to step 6 and use the new defined region.
10. Executing "save spectrum" command for source and background individually. Note: the procedure in step 6 to step 10 should be done individually for source and background.
11. Execute "exit" command to close XSELECT
12. Run XRTEXPOMAP by executing "xrtexpomap" command in terminal.

13. Load event file, Attitude file and House keeping file of the observation one by one. Note: The attitude and house keeping files located in "auxil" and "/xrt/hk" folders of downloaded data accordingly.

14. XRTEXPOMAP will make an exposure map image using the SWIFT calibration data.

15. Execute "exit" command to close XRTEXPOMAP.

16. Run XRTMKARF by executing "xrtmkarf" command in terminal.

17. Load source spectrum which is created in step 10.

18. Load exposure map created which is created in step 14

19. Give a name to the output ARF file.

20. Look at report and write version of Response Matrix File which is used automatically from CALDB data base.

21. Execute "exit" command to close XRTMKARF

22. Download Response Matrix File which is noted in step 20 from *SWIFT-XRT* calibration database (CALDB)[29]

23. Run GRPPHA by executing "grppha" command in terminal.

24. Load source spectrum which is created in step 10.

25. Give a name to the output spectrum file.

26. Define channels which contains bad data by execute command "bad 0-29".

27. To have enough counts (in this case 20) in each bin of your spectrum execute "group min 20" command.

[29] `http://heasarc.gsfc.nasa.gov/docs/heasarc/caldb/data/swift/xrt/index.html`

28. Execute command "chkey backfile" followed by the name of background spectrum created in step 10.

29. Execute command "chkey ancrfile" followed by the name of ARF file created in step 20

30. Execute command "chkey respfile" followed by the name of RMF file downloaded in step 22

31. Execute "exit" command to save the spectrum and exit GRPPHA.

32. Run XSPEC by executing "xspec" command.

33. Load the spectrum created step 31.

34. Define the model which you want to fit spectra with it (In my case the command was "model phabs(powerlaw)" to fit the spectrum with photoelectric absorbed model and power law model).

35. Re-normalize your data by simply type "renorm" command.

36. Ignore bad data by executing "ignore bad" command.

37. Fit the model to data by simply type "fit" command.

38. Check the statistical parameters of your modelled spectrum fitting.

39. If the statistic of fit is good proceed to next step. If not you should start a try and error on the model and ignored channels to get a good statistical fit.

40. The spectrum parameters (In my case spectral index and Hydrogen-equivalent column density (N_H)) and statistics parameter (In my case reduced χ^2) are available in the report.

41. Calculate the flux in the proper range by executing "flux" command following by the range you want and if needed its error.

42. execute "save all" to save all of parameters and fitted spectra in a file with "xcm" extension.

43. Execute "exit" command to exit XSPEC.

The following pages show an example of complete cycle of X-ray data reduction using the presented procedure.

```
======================================================================
$ heainit
$ xselect
                          **  XSELECT V2.4b  **
> Enter session name >[SWIFT] magic
magic:SUZAKU > read event
> Enter the Event file dir >[] /home/vafara/prsource/xray/Last/
> Enter Event file list >[] sw00039229006xpcw3po_cl.evt
Got new mission: SWIFT
> Reset the mission ? >[yes]
  Notes: XSELECT set up for      SWIFT
 Time keyword is TIME       in units of s
 Default timing binsize =   5.0000
Setting...
 Image  keywords   = X          Y           with binning =    1
 WMAP   keywords   = X          Y           with binning =    1
 Energy keyword    = PI                     with binning =    1
Getting Min and Max for Energy Column...
Got min and max for PI:     0   1023
Got the minimum time resolution of the read data:   2.5073
MJDREF =  5.1910000742870E+04 with TIMESYS = TT
 Number of files read in:           1
 ******************** Observation Catalogue ********************
Data Directory is: /home/vafara/prsource/xray/Last/
HK Directory is: /home/vafara/prsource/xray/Last/
         OBJECT      OBS_ID      DATE-OBS    DATAMODE
      1 J2001+4352  00039229006 2010-07-16T   PHOTON
magic:SWIFT-XRT-PHOTON > extract image
extractor v5.23    23 Mar 2012
 Getting FITS WCS Keywords
Doing file:/home/vafara/~/Last/sw00039229006xpcw3po_cl.evt
 10% completed
100% completed
          Total      Good    Bad: Time     Phase     Grade       Cut
           1149      1149             0         0         0         0
======================================================================
    Grand Total      Good    Bad: Time     Phase     Grade       Cut
           1149      1149             0         0         0         0
   in  3858.7     seconds
 Image            has     1149 counts for 0.2978     counts/sec
magic:SWIFT-XRT-PHOTON > plot image
magic:SWIFT-XRT-PHOTON > filter region source.reg
magic:SWIFT-XRT-PHOTON > extract spectrum
extractor v5.23    23 Mar 2012
 Getting FITS WCS Keywords
Number of regions = 1
sign = 1, shape = 2, comp = 1
492.308631 536.471850 19.937965 0.000000 0.000000 0.000000 0.000000
0.000000 0.000000 0.000000 -nan 0.000000 0.000000 397.522442 0.000000
472.370666 512.246596 516.533885 556.409814
```

```
 Doing file: /home/vafara/~/Last/sw00039229006xpcw3po_cl.evt
[regfilter("magic_region.xsl",X,Y)]
 10% completed
100% completed
          Total      Good    Bad: Time     Phase     Grade       Cut
            303       303             0         0         0         0
============================================================================
    Grand Total      Good    Bad: Time     Phase     Grade       Cut
            303       303             0         0         0         0
   in  3858.7     seconds
 Spectrum         has      303 counts for 7.8523E-02 counts/sec
 ... written the PHA data Extension
magic:SWIFT-XRT-PHOTON > save spectrum source.pi
Wrote spectrum to source.pi
magic:SWIFT-XRT-PHOTON > clear region
magic:SWIFT-XRT-PHOTON > filter region back.reg
magic:SWIFT-XRT-PHOTON > extract spectrum
extractor v5.23    23 Mar 2012
 Getting FITS WCS Keywords
Number of regions = 1
sign = 1, shape = 2, comp = 1
336.750986 595.499689 19.938017 0.000000 0.000000 0.000000 0.000000
0.000000 0.000000 0.000000 -nan 0.000000 0.000000 397.524509 0.000000
316.812970 356.689003 575.561672 615.437706
 Doing file: /home/vafara/~/Last/sw00039229006xpcw3po_cl.evt
[regfilter("magic_region.xsl",X,Y)]
 50% completed
100% completed
         Total      Good    Bad: Time     Phase     Grade       Cut
           4          4             0         0         0         0
============================================================================
  Grand Total      Good    Bad: Time     Phase     Grade       Cut
            4         4             0         0         0         0
   in  3859.2     seconds
 Spectrum         has        4 counts for 1.0365E-03 counts/sec
 ... written the PHA data Extension
magic:SWIFT-XRT-PHOTON > save spectrum back.pi
Wrote spectrum to back.pi
magic:SWIFT-XRT-PHOTON > exit
> Save this session? >[yes]
exit
$ xrtexpomap infile=sw00039229006xpcw3po_cl.evt
attfile=sw00039229006sat.fits hdfile=sw00039229006xhd.hk outdir=./
------------------------------------------------------------
             Running ' xrtexpomap version 0.2.7 '
------------------------------------------------------------
------------------------------------------------------------------------
  Running 'xrtinstrmap_0.3.3'
------------------------------------------------------------------------
 Input Parameters List:
Name of the input Event file           :'sw00039229006xpcw3po_cl.evt'
Name of the input region file          :'CALDB'
Name of the input HK Header file       :'sw00039229006xhd.hk'
Name of the output instrument map file :
                               './sw00039229006xpcw3po_rawinstr.img'
Check pointing stability?(yes/no)      :'no'
------------------------------------------------------------------------
xrtinstrmap_0.3.3: Info: Processing 'sw00039229006xpcw3po_cl.evt'file
xrtinstrmap_0.3.3: Info: Processing sw00039229006xhd.hk file.
xrtinstrmap_0.3.3: Info: Processing 'http://heasarc.gsfc.nasa.gov/FTP
/caldb/data/swift/xrt/bcf/instrument/swxregion20010101v004.fits' file
xrtinstrmap_0.3.3: Info: Appended 1 image in
```

```
                              ./sw00039229006xpcw3po_rawinstr.img file
xrtinstrmap_0.3.3: Info: Appended 2 image in
                              ./sw00039229006xpcw3po_rawinstr.img file
xrtinstrmap_0.3.3: Info: Appended 3 image in
                              ./sw00039229006xpcw3po_rawinstr.img file
xrtinstrmap_0.3.3: Info: Appended 4 image in
                              ./sw00039229006xpcw3po_rawinstr.img file
xrtinstrmap_0.3.3: Info: Appended 5 image in
                              ./sw00039229006xpcw3po_rawinstr.img file
xrtinstrmap_0.3.3: Info: Appended 6 image in
                              ./sw00039229006xpcw3po_rawinstr.img file
xrtinstrmap_0.3.3: Info:
      File './sw00039229006xpcw3po_rawinstr.img' successfully written
-------------------------------------------------------------------------
xrtinstrmap_0.3.3: Exit with success.
-------------------------------------------------------------------------
swiftxform: running ftcopy
swiftxform: verbose: HDU[1] skytime DEFAULT[TMIDDLE]=>300934317.56331
swiftxform: running getxform
swiftxform: running imagetrans
swiftxform: running getwcs
swiftxform: running fthedit
swiftxform: verbose: HDU[2] skytime DEFAULT[TMIDDLE]=>300940282.70938
swiftxform: running getxform
swiftxform: running imagetrans
swiftxform: running getwcs
swiftxform: running fthedit
swiftxform: verbose: HDU[3] skytime DEFAULT[TMIDDLE]=>300946242.94520
swiftxform: running getxform
swiftxform: running imagetrans
swiftxform: running getwcs
swiftxform: running fthedit
swiftxform: verbose: HDU[4] skytime DEFAULT[TMIDDLE]=>300950259.35278
swiftxform: running getxform
swiftxform: running imagetrans
swiftxform: running getwcs
swiftxform: running fthedit
swiftxform: verbose: HDU[5] skytime DEFAULT[TMIDDLE]=>300956261.21069
swiftxform: running getxform
swiftxform: running imagetrans
swiftxform: running getwcs
swiftxform: running fthedit
swiftxform: verbose: HDU[6] skytime DEFAULT[TMIDDLE]=>300961927.43731
swiftxform: running getxform
swiftxform: running imagetrans
swiftxform: running getwcs
swiftxform: running fthedit
swiftxform: running ftchecksum
 No of detectors read in:   30
![XIMAGE> chat 0
![XIMAGE> read "./sw00039229006xpcw3po_skyinstr.img+1"
![XIMAGE>   read_image ./sw00039229006xpcw3po_skyinstr.img+1
![XIMAGE> save_ima
![XIMAGE> read "./sw00039229006xpcw3po_skyinstr.img+2"
![XIMAGE>   read_image ./sw00039229006xpcw3po_skyinstr.img+2
![XIMAGE> sum_ima
![XIMAGE> save_ima
![XIMAGE> read "./sw00039229006xpcw3po_skyinstr.img+3"
![XIMAGE>   read_image ./sw00039229006xpcw3po_skyinstr.img+3
![XIMAGE> sum_ima
![XIMAGE> save_ima
```

```
![XIMAGE> read "./sw00039229006xpcw3po_skyinstr.img+4"
![XIMAGE>   read_image ./sw00039229006xpcw3po_skyinstr.img+4
![XIMAGE> sum_ima
![XIMAGE> save_ima
![XIMAGE> read "./sw00039229006xpcw3po_skyinstr.img+5"
![XIMAGE>   read_image ./sw00039229006xpcw3po_skyinstr.img+5
![XIMAGE> sum_ima
![XIMAGE> save_ima
![XIMAGE> read "./sw00039229006xpcw3po_skyinstr.img+6"
![XIMAGE>   read_image ./sw00039229006xpcw3po_skyinstr.img+6
![XIMAGE> sum_ima
![XIMAGE> save_ima
![XIMAGE> write_ima/file="./sw00039229006xpcw3po_sumskyinstr.img"
![XIMAGE> quit
![XIMAGE> exit
------------------------------------------------------------------------
  Running 'xrtexpocalc_0.1.4'
------------------------------------------------------------------------
 Input Parameters List:
Name of the input Event file:
  './sw00039229006xpcw3po_sumskyinstr.img.gz'
Name of the output Event file:'./sw00039229006xpcw3po_ex.img'
------------------------------------------------------------------------
xrtexpocalc_0.1.4: Info:
 Processing './sw00039229006xpcw3po_sumskyinstr.img.gz' file.
xrtexpocalc_0.1.4: Info:
    File  ./sw00039229006xpcw3po_ex.img successfully written.
------------------------------------------------------------------------
xrtexpocalc_0.1.4: Exit with success.
------------------------------------------------------------------------
------------------------------------------------------------
xrtexpomap_0.2.7: Exit with success
------------------------------------------------------------
$ exit
$ xrtmkarf expofile=sw00039229006xpcw3po_ex.img
Name of the input PHA FITS file[source.pi] source.pi
Apply PSF correction (used if extended=no)?(yes/no)[yes]
Name of the output ARF FITS file[1.arf] magic.arf
Source X coordinate (SKY for PC and WT modes, DET for PD mode)
                                        (used if extended=no):[] -1
Source Y coordinate (SKY for PC and WT modes, DET for PD mode)
                                        (used if extended=no):[] -1
------------------------------------------------------------
Running 'xrtmkarf_0.6.0'
------------------------------------------------------------
 Input Parameters List:
Name of the input RMF file                    :'CALDB'
Name of the input mirror effective area file  :'CALDB'
Name of the input filter transmission file    :'CALDB'
Name of the input arf file                    :'CALDB'
Name of the input exposure map file    :'sw00039229006xpcw3po_ex.img'
Name of the input vignetting file             :'CALDB'
Name of the input spectrum file               :'source.pi'
Name of the input PSF file                    :'CALDB'
Name of the output ARF file                   :'magic.arf'
Source SKYX                                   :'-1.000000'
Source SKYY                                   :'-1.000000'
Source off-axis angle (arcmin)                :'-99.000000'
Extended source?                              : no
------------------------------------------------------------
vig_flag (in)  : 0
```

```
  min exposure : 0.000000 in 0 0
  max exposure : 3858.734375 in 443 221
 MAXIMUM EXPOSURE : 1.000000
 CENTER of the ROI (SKY)  492.308631 536.471850
 CENTER of the SRC (SKY)  492.308624 536.471863
xrtmkarf_0.6.0: Info: WMAP region boundaries
      (X1:X2,Y1:Y2):[ 473 : 513 , 517 : 557 ]
xrtmkarf_0.6.0: Info: Source position (X,Y): [492.308624 ,536.471863]
  min ROI exposure : 1546.387939 in 479 525
  max ROI exposure : 3858.734375 in 474 530
xrtmkarf_0.6.0: Info: Processing 'http://heasarc.gsfc.nasa.gov/FTP/ca
ldb/data/swift/xrt/cpf/rmf/swxpc0to12s6_20010101v014.rmf' CALDB file.
xrtmkarf_0.6.0: Info: Processing 'http://heasarc.gsfc.nasa.gov/FTP/ca
       ldb/data/swift/xrt/cpf/arf/swxs6_20010101v001.arf' CALDB file.
300.296211 43.857792 300.296200 43.857790
 Optical Axis SKY coordinate X: 500.487992
 Optical Axis SKY coordinate Y: 500.502970
CX: 492.308624 CY: 536.471863 Off-axis Angle (arcmin): 1.450895
vig_flag   : 0
>>> using a not vignetted exposure map
 xrtmkarf_0.6.0: Info: Processing 'http://heasarc.gsfc.nasa.gov/FTP/
 caldb/data/swift/xrt/cpf/vign/swxvign20010101v001.fits' CALDB file.
xrtmkarf_0.6.0: Info: Processing 'http://heasarc.gsfc.nasa.gov/FTP/
caldb/data/swift/xrt/cpf/psf/swxpsf20010101v005.fits' CALDB file.
 PERC. OF FLUENCE WITHIN THE ROI:  84.531361 % (AT 1.002500 keV )
 PERC. OF FLUENCE WITHIN THE ROI:  84.550029 % (ON AVERAGE)
xrtmkarf_0.6.0: Info: 'magic.arf' file successfully written.
------------------------------------------------------------------------
xrtmkarf_0.6.0: Exit with success.
------------------------------------------------------------------------
$ exit
$ grppha
Please enter PHA filename[source.pi]
Please enter output filename[final.pi] magic.pi
  -------------------------
  MANDATORY KEYWORDS/VALUES
  ------------------------------------------------------------------------
  EXTNAME   - SPECTRUM        Name of this BINTABLE
  TELESCOP  - SWIFT           Mission/Satellite name
  INSTRUME  - XRT             Instrument/Detector
  FILTER    - NONE            Instrument filter in use
  EXPOSURE  - 3843.3          Integration time (in secs) of PHA data
  AREASCAL  - 1.0000          Area scaling factor
  BACKSCAL  - 1.25000E-03     Background scaling factor
  BACKFILE  - none            Associated background file
  CORRSCAL  - 1.0000          Correlation scaling factor
  CORRFILE  - none            Associated correlation file
  RESPFILE  - none            Associated redistribution matrix file
  ANCRFILE  - none            Associated ancillary response file
  POISSERR  - TRUE            Whether Poissonian errors apply
  CHANTYPE  - PI              Whether channels have been corrected
  TLMIN1    - 0               First legal Detector channel
  DETCHANS  - 1024            No. of legal detector channels
  NCHAN     - 1024            No. of detector channels in dataset
  PHAVERSN  - 1.2.0           OGIP FITS version number
  STAT_ERR  - FALSE           Statistical Error
  SYS_ERR   - FALSE           Fractional Systematic Error
  QUALITY   - TRUE            Quality Flag
  GROUPING  - FALSE           Grouping Flag
  ------------------------------------------------------------------------
GRPPHA[group min 20] bad 0-29
GRPPHA[exit] group min 20
```

```
GRPPHA[group min 20] chkey backfile back.pi
GRPPHA[chkey backfile back.pi] chkey ancrfile magic.arf
GRPPHA[chkey ancrfile magic.arf]
                        chkey respfile swxpc0to12s6_20010101v014.rmf
GRPPHA[chkey respfile swxpc0to12s6_20010101v014.rmf] exit
 ... written the PHA data Extension
 ...... exiting, changes written to file : magic.pi
 ** grppha 3.0.1 completed successfully
$ exit
$ xspec
XSPEC version: 12.8.0
Build Date/Time: Fri Jan 11 16:23:36 2013
XSPEC12>data magic.pi
***Warning: Detected response matrix energy bin value = 0 (or neg).
     XSPEC will instead use small finite value
      (response file will not be altered).
1 spectrum  in use
Spectral Data File: magic.pi  Spectrum 1
Net count rate (cts/s) for Spectrum:1
                  7.780e-02 +/- 4.559e-03 (98.7 % total)
 Assigned to Data Group 1 and Plot Group 1
  Noticed Channels:  1-693
  Telescope: SWIFT Instrument: XRT  Channel Type: PI
  Exposure Time: 3843 sec
 Using fit statistic: chi
 Using test statistic: chi
 Using Background File                back.pi
  Background Exposure Time: 3844 sec
 Using Response (RMF) File swxpc0to12s6_20010101v014.rmf for Source 1
 Using Auxiliary Response (ARF) File  magic.arf
XSPEC12>model phabs(powerlaw)
Input parameter value, delta, min, bot, top, and max values for ...
      1       0.001(0.01)          0          0     100000      1e+06
1:phabs:nH>
      1       0.01(0.01)         -3         -2          9         10
2:powerlaw:PhoIndex>
      1       0.01(0.01)          0          0      1e+24      1e+24
3:powerlaw:norm>
========================================================================
Model phabs<1>*powerlaw<2> Source No.: 1   Active/On
Model Model Component  Parameter  Unit     Value
 par  comp
   1    1   phabs      nH         10^22    1.00000      +/-  0.0
   2    2   powerlaw   PhoIndex            1.00000      +/-  0.0
   3    2   powerlaw   norm                1.00000      +/-  0.0
------------------------------------------------------------------------
Fit statistic : Chi-Squared =   7.266136e+08 using 693 PHA bins.
***Warning:Chi-square may not be valid due to bins with zero variance
           in spectrum number(s): 1
Test statistic : Chi-Squared =   7.266136e+08 using 693 PHA bins.
 Reduced chi-squared =   1.053063e+06 for    690 degrees of freedom
 Null hypothesis probability =   0.000000e+00
***Warning:Chi-square may not be valid due to bins with zero variance
           in spectrum number(s): 1
 Current data and model not fit yet.
XSPEC12>renorm
Fit statistic : Chi-Squared =         195.27 using 693 PHA bins.
***Warning:Chi-square may not be valid due to bins with zero variance
           in spectrum number(s): 1
Test statistic : Chi-Squared =         195.27 using 693 PHA bins.
 Reduced chi-squared =        0.28300 for    690 degrees of freedom
```

```
 Null hypothesis probability =   1.000000e+00
***Warning:Chi-square may not be valid due to bins with zero variance
           in spectrum number(s): 1
 Current data and model not fit yet.
XSPEC12>ignore bad
ignore:   679 channels ignored from  source number 1
Fit statistic : Chi-Squared =         173.92 using 14 PHA bins.
Test statistic : Chi-Squared =         173.92 using 14 PHA bins.
 Reduced chi-squared =         15.810 for     11 degrees of freedom
 Null hypothesis probability =   1.843335e-31
 Current data and model not fit yet.
XSPEC12>fit
                                      Parameters
Chi-Squared  |beta|/N    Lvl          1:nH    2:PhoIndex       3:norm
172.963      8.00355e-10  -3        1.00000       1.00000  0.000409943
121.44       11.719       -1       0.189407       1.44223  0.000269747
75.5776      71145.8      -2       0.345793       3.50393   0.00101223
48.364       17433.1      -1       0.318357       2.10493   0.00144839
12.9325      24038.8      -2       0.329632       2.49965   0.00141353
11.5683      2612.63      -3       0.371229       2.74866   0.00158687
11.5561      269.52       -4       0.374777       2.77076   0.00161587
11.5561      7.8365       -5       0.374666       2.77040   0.00161559
========================================
 Variances and Principal Axes
                 1        2        3
 9.7088E-09| -0.0030  -0.0005   1.0000
 1.1157E-03|  0.9777  -0.2099   0.0028
 1.0398E-01| -0.2099  -0.9777  -0.0011
----------------------------------------
====================================
  Covariance Matrix
        1           2           3
   5.649e-03   2.111e-02   2.741e-05
   2.111e-02   9.945e-02   1.128e-04
   2.741e-05   1.128e-04   1.479e-07
------------------------------------
======================================================================
Model phabs<1>*powerlaw<2> Source No.: 1   Active/On
Model Model Component  Parameter Unit     Value
 par  comp
   1    1   phabs      nH        10^22  0.374666     +/-  7.51632E-02
   2    2   powerlaw   PhoIndex         2.77040      +/-  0.315350
   3    2   powerlaw   norm             1.61559E-03  +/-  3.84579E-04
----------------------------------------------------------------------
Fit statistic : Chi-Squared =          11.56 using 14 PHA bins.
Test statistic : Chi-Squared =          11.56 using 14 PHA bins.
 Reduced chi-squared =          1.051 for     11 degrees of freedom
 Null hypothesis probability =   3.979140e-01
XSPEC12>flux 2. 10. err
Parameter distribution is derived from fit covariance matrix.
 Model Flux 0.00023479 photons (1.3281e-12 ergs/cm^2/s) range
(2.0000 - 10.000 keV) Error range 0.0001972 - 0.0002768
(1.084e-12 - 1.676e-12)  (68.00% confidence)
XSPEC12>exit
XSPEC: quit
```